POLITECNICO DI TORINO

Master Thesis
in Nanotechnologies for ICTs

Master Thesis

Single-Electron Phenomena in Electrochemistry of Biosensors

Supervisors:

Prof. Alberto Tagliaferro
Prof. Sandro Carrara

Candidate:

Tommaso Serra

December 2020

Abstract

In this work, we modelled Coulomb blockade and Coulomb staircase phenomena starting from first-principles and taking advantage of Schrödinger-like problems knowledge.

Coulomb blockade and staircase phenomena are physical effects related to the quantization of levels in a nanoparticle. In the past, experimental results concerning these phenomena have been modelled with either semiclassical or circuit-like models, which derive electrical parameters such as capacitances and resistances in order to reproduce the measured currents trends.

Our approach, as quoted above, originates in the framework of quantum mechanics. As a first step, we studied a simplified model, which is often used to describe a similar quantum structure, in which discretized energy levels exist in the region enclosed between two one-dimensional potential energy barriers. In this model, when electrons are forced to drift across the system under the effect of a bias voltage, they are able to tunnel across the first energy barrier to move to one of the available energy levels, eventually leaving the system by tunneling across the other barrier.

When dealing with coherent electron transport collisions are not phase-breaking and quantization of the available conducting channels emerges either as a staircase-like or an oscillating resonant current-voltage characteristics, depending on the nanoparticle size.

Literature provides analytic expressions for quantum tunneling across one, two or multiple barriers when no external bias is applied to the system. However, as our goal was to model the effect of bias voltage we were forced to revert to a numerical approach. To this purpose, we implemented the solution of the out-of-equilibrium Schrödinger equation using *Finite Element Method* (FEM) and *Non-Equilibrium Green's Functions* (NEGF) approaches.

The FEM solution, although computationally less expensive than the NEGF algorithm, proves to be viable only at equilibrium and small-bias conditions, while the NEGF solution provides reliable results over a wider bias voltage range. Hence, we focused on a NEGF approach. The obtained results have been analyzed in order to identify the role that each geometrical parameter plays in determining the current-voltage curve shape.

Once the first step completed, as our target was to apply the model to the simulation and design of nanoparticle-enhanced electrochemical biosensors, we modified the geometrical structure in order to emulate a nanoparticle with an attached molecule. Now, quantum tunneling can only occur when an energy level within the nanoparticle sits at an energy close enough to that of an unoccupied energy level of the molecule, or vice versa. Current-voltage characteristics obtained for these kind of systems have been found to be very similar both in shape and order of magnitude to those available in literature.

As the problem to tackle is rather challenging, the present work, although leading to satisfactory results, represents a first critical step in the direction of a comprehensive tool for the simulation and design of nanoparticle-enhanced electrochemical biosensors. Improvements can be made in optimizing the solving algorithm, making it more efficient and less time-consuming, as well as including other relevant physical phenomena in order to obtain a more complete description of the electron transfer. An example could be the inclusion of the *hopping* phenomenon, which plays a role most probably as relevant as tunneling, but for incoherent electron transport.

Acknowledgements

Ringrazio i relatori, prof. Alberto Tagliaferro e prof. Sandro Carrara, per avermi guidato con pazienza e disponibilità in questo progetto nonostante le difficoltà legate al lavoro a distanza. Ringrazio il dott. Massimo Rovere per i consigli sull'utilizzo di MATLAB.

Inoltre, ringrazio la mia famiglia e i miei amici per avermi supportato e sopportato in questi cinque anni di università.

Contents

Abstract i

Acknowledgements ii

List of Figures iii

List of Tables v

Introduction 2

1 Tunneling models 3
1.1 Equilibrium analytic models . . . 3
1.1.1 Single-barrier tunneling . . . 4
1.1.2 Double-barrier tunneling . . . 5
1.2 Landauer-Büttiker formula . . . 6

2 Numerical implementation 9
2.1 FEM solution of the Schrödinger equation . . . 9
2.1.1 Lagrange polynomials as basis functions . . . 9
2.1.2 Weak formulation of Schrödinger's equation . . . 10
2.1.3 Boundary conditions . . . 11
2.1.4 Pseudocode of the FEM solving algorithm . . . 13
2.1.5 Model testing . . . 13
2.1.6 Simulations with bias voltage . . . 15
2.2 NEGF formalism . . . 18
2.2.1 Retarded and advanced Green's functions . . . 18
2.2.2 The infinitesimal η . . . 19
2.2.3 Matrix formulation for the numerical solution . . . 19
2.2.4 Matrix truncation and *self-energy* term . . . 20
2.2.5 Transmission function and current . . . 21
2.2.6 Density matrix, spectral function and local density of states . . . 22
2.2.7 A more rigorous definition of the one-particle Green's functions . . . 23
2.2.8 Single-particle Green's function of many-body systems . . . 24
2.2.9 Current density operator . . . 26
2.2.10 Current operator and relation to the Landauer-Büttiker formula . . . 27
2.2.11 Summary of the solution procedure . . . 28
2.2.12 Pseudocode of the NEGF solving algorithm . . . 30
2.2.13 Model testing and validation . . . 31

3 The influence of geometrical parameters on the Coulomb blockade **39**
3.1 Effect of the barriers thickness . . . 40
3.2 Effect of the "barriers height": the U_0 value . . . 41
3.3 Effect of the distance between barriers . . . 43
3.4 Relation between transmission and current peaks . . . 44

4 Three-barrier systems: a molecule bound to the nanoparticle **49**
4.1 The metal contact . . . 49
4.2 Simulations with a metal contact . . . 50
4.3 Nanoparticle-molecule bound system . . . 52
4.3.1 Individual systems . . . 52
4.3.2 The bound system . . . 53
4.3.3 Voltage drop across the molecule . . . 56
4.3.4 The importance of levels alignment . . . 57
4.3.5 Crossing over of energy levels . . . 59
4.3.6 Conduction of an individual molecule . . . 61
4.4 Simulation of a real system . . . 63

Conclusions and outlook **66**

Bibliography **67**

A Analytic derivation for single- and double-barrier transmission probabilities **69**
A.1 Single barrier . . . 69
A.2 Double barrier . . . 72

B Explicit expression of the FEM matrix elements **73**
B.1 Stiffness matrix elements . . . 73
B.2 Mass matrix elements . . . 74
B.3 Matrix assembling . . . 74

List of Figures

1.1 Single potential barrier 4
1.2 Double potential barrier 5
1.3 Graphical representation for the Landauer-Büttiker formula derivation 7

2.1 First-order Lagrange polynomials 10
2.2 Single-barrier tunneling probability comparison, analytic and FEM 14
2.3 Double-barrier tunneling probability comparison, analytic and FEM 15
2.4 1V, linear voltage drop between the contacts 15
2.5 FEM transmission probability, evolution with increasing bias 17
2.6 Ballistic device, equilibrium LDOS 31
2.7 Ballistic device, equilibrium transmission probability and total current 32
2.8 Ballistic device, total current 32
2.9 Single-barrier tunneling device, equilibrium transmission probability comparison 33
2.10 Single-barrier tunneling device total current, linear and logarithmic axes 34
2.11 Double-barrier resonant tunneling device, equilibrium LDOS 34
2.12 Double-barrier resonant tunneling device, equilibrium transmission probability comparison . . 35
2.13 NEGF transmission probability, evolution with increasing bias 37
2.14 Double-barrier resonant tunneling device, total current 38
2.15 Higher bias total current, logarithmic axis 38

3.1 Bias voltage such that only one energy level is conducting at a time 39
3.2 Reference simulated system for barriers thickness comparison and transmission functions . . . 40
3.3 Total current comparison for different barriers thicknesses 41
3.4 Transmission analysis for different U_0 values 42
3.5 Total current for different U_0 values 42
3.6 Transmission function for different nanoparticle sizes 43
3.7 Total current for different nanoparticle sizes. 44
3.8 Five-levels system used for the peaks analysis 45
3.9 Simulation results of the system used for the peaks analysis 45
3.10 Peaks positions analysis 46
3.11 Analysis of the gap between peaks 47
3.12 Potential of each contact 48

4.1 Bias voltage profile used in chapter 3 50
4.2 Modified bias voltage profile for a metal contact 50
4.3 Test system, metal contact. 51
4.4 Current comparison at different temperatures 51
4.5 Restoring Coulomb blockade at room temperature 52
4.6 Nanoparticle system. 53
4.7 Molecule system. 53

4.8 Nanoparticle-molecule bound system. 54
4.9 Bound system under a 0.05 V-bias 55
4.10 Bound system under a 0.15 V-bias 55
4.11 Bound system, total current 56
4.12 Bias voltage comparison with and without extending the voltage drop to the third barrier . . 56
4.13 Current comparison with and without extending the voltage drop to the third barrier 57
4.14 System with conducting channel outside the bias window 58
4.15 Current comparison of aligned and misaligned energy levels inside the bias window 59
4.16 Energy levels crossing over in the bound system 59
4.17 Larger system with no crossing over of energy levels 60
4.18 Systems with and without the nanoparticle 61
4.19 Transmission function without nanoparticle 62
4.20 I-V characteristics without nanoparticle 62
4.21 Current of an individual molecule with decreasing distance from the contact 63
4.22 Current comparison with and without nanoparticle 63
4.23 Experimental voltammogram 64
4.24 System used for the simulation of the experimental setup. 65

List of Tables

3.1 Analysis of position and gap between consecutive transmission and current peaks 46

4.1 Individual nanoparticle and molecule energy levels 52

Introduction

Molecular-scale electronic components, such as nanoparticles or quantum dots, are of growing interest due to their potential to become part of future nanoscale devices.

Advancements in experimental techniques made it possible to fabricate molecular-scale devices, as well as junctions between such components and two, or more, electrodes. From an applied point of view, it is desirable to control the way electrodes and nanoparticle are coupled, and eventually connect individual devices into a working circuit; on the other hand, it is also important to understand and model electron transport at the nanoscale.

Molecules and nanoparticles alike can be described as a set of discrete energy levels, and coupling with the contacts is usually assumed to be weak so that the discrete energy levels can be considered isolated from the contacts by potential energy barriers.

Under the effect of an applied bias voltage a current flows through the system; however, the number of electrons that are able to tunnel across the barriers depends on the energetically available confined energy levels. This phenomenon is known as *Coulomb blockade* of electrons, in which the discretization of conducting channels reflects onto the current-voltage characteristics that shows a unique staircase-like or oscillatory trend.

The Coulomb blockade is mostly visible at low temperatures conditions, that cause the thermal energy of electrons $k_B T$ to be lower than the energy required to add a new electron to the quantum dot; however, with sufficient spacing between energy levels, this phenomenon is observable even at room temperature.

Among the many approaches that have been applied to the Coulomb blockade, many rely on the definition of circuit-like electrical parameters, such as resistances and capacitances, to generate an equivalent circuit that is able to reproduce the current of the analysed system.

In this work, the Coulomb blockade phenomenon has been modelled by numerical solution of first-principle, Schrödinger-like problems.

Organization of this work

Analytic tunneling formulas that can be derived from Schrödinger's equation are presented in chapter 1. These formulas are commonly available in literature, and the starting point is the tunneling across a single barrier: incoming electrons, represented as plane waves, are partially reflected and partially transmitted through the barrier.

It is possible to generalize this concept to as many barriers as needed by combining single-barrier scattering matrices.

The Landauer-Büttiker formula is also introduced in this chapter with a simple approach based on balance equations of inflows and outflows of current. This formula allows to derive a current from the tunneling, or transmission, probability of the system under analysis; however, it applies to a system subject to a bias voltage.

Since the analytic tunneling expression presented in chapter 1 are strictly valid for a system in equilibrium condition, the Schrödinger equation outside of equilibrium is solved numerically in chapter 2. Two solution

methods are presented in this chapter: the first and simpler one is a direct solution of Schrödinger's equation by *Finite Element Method* (FEM) which proves to be effective only at near-equilibrium conditions, while the second one is based on the more sophisticated *Non-Equilibrium Green's Functions* (NEGF) approach. In general, the concept of Green's functions is applicable whenever the response of a system is related to the excitation through a differential operator; hence, it can be used to solve Schrödinger's equation.

The NEGF approach proves to be viable over a wider range of bias voltages than the FEM; therefore, it is the method of choice in the remaining chapters.

The effect of geometrical parameters on the confined energy levels is analysed in chapter 3. For this analysis, parameters have been varied independently from one another to determine which one affects the most the distribution of energy levels.

In addition, by allowing only one energy level to conduct at each time, it is possible to highlight the gap between two consecutive conducting channels through the current, and observe the contribution of each conducting channel individually.

Finally, chapter 4 turns towards more realistic system, by simulating a three-barrier system that aims to represent a molecule bound to a nanoparticle.

The aim of this work is to represent a first step in the direction of comprehensive modelling and designing of nanoparticle-enhanced electrochemical biosensors. To this purpose, the voltage drop has been modified so that the junction of the nanoparticle with the contacts is more closely reminding to a metal junction, similarly to many experimental setups.

Moreover, the importance of aligning molecular energy levels with the nanoparticle ones is verified, and allows the formation of conducting channels through the whole system; thus yielding a better current signal via sequential tunneling of electrons.

The advantage of using a nanoparticle to enhance the current signal produced by a single molecule is proven with respect to an individual molecule bound directly to the metal contact.

Finally, this work concludes with an attempt at reproducing a current-voltage curve from experimental measurements on a real system.

Chapter 1

Tunneling models

The theoretical model is based on the solution of the time-independent Schrödinger equation for an arbitrary potential [1], [2].

The stationary Schrödinger equation can be expressed as

$$H(\boldsymbol{r})\psi_n(\boldsymbol{r}) = E_n\psi_n(\boldsymbol{r}), \qquad H(\boldsymbol{r}) = -\frac{\hbar^2}{2m}\frac{d^2}{d\boldsymbol{r}^2} + U(\boldsymbol{r}) \tag{1.1}$$

in which the quantum number n is used to label the different energy levels E_n and their corresponding eigenfunctions $\psi_n(x)$.
As a consequence, stationary states are characterized by a time-dependent wavefunction

$$\Psi_n(\boldsymbol{r}, t) = \psi_n(\boldsymbol{r}) \cdot \exp\left\{-\frac{iE_n t}{\hbar}\right\} \tag{1.2}$$

and, since equation (1.1) is linear, the most general solution is given by a linear combination of $\Psi_n(\boldsymbol{r}, t)$:

$$\Psi(\boldsymbol{r}, t) = \sum_n C_n \Psi_n(\boldsymbol{r}, t) \tag{1.3}$$

where C_n are complex coefficients.

In the analysis performed in this work, systems are one-dimensional and the potential $U(\boldsymbol{r}) = U(x)$ is a function that generates abrupt discontinuities along the x direction.

1.1 Equilibrium analytic models

According to [3], a nanoparticle can be modelled as a double potential barrier, with energy levels confined in-between, and a current signal can be measured as a consequence of transmission, or tunneling, of incoming electrons through the system.

An analytic expression describing this phenomenon can be derived from equation (1.1), starting with a single potential barrier [1], and then combining the effect of two barriers via the *scattering matrix* formalism presented in [4].

1.1.1 Single-barrier tunneling

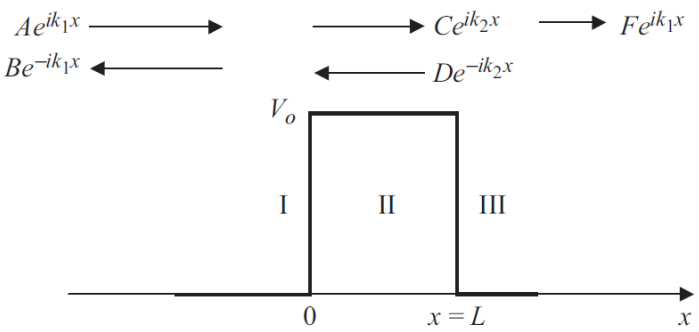

Figure 1.1: Single potential barrier; image taken from [1].

The system is shown in figure 1.1. In order to avoid misinterpretations, despite the notation used in the image, U will be used to refer to the potential energy; while V will be reserved when referring to the bias voltage in the next sections.

The derivation performed in [1] at first assumes the particle energy E to be such as $E > U_0$; and, by assuming the particle is arriving from $x = -\infty$, it avoids reflections in region III. As a consequence, there is only one wavevector associated to the particle in that specific region.

Assuming quantum effects to be present only along the x-direction, the stationary solution of Schrödinger's equation (1.1) can be factorized in a transverse envelope $\chi(y, z)$ and a longitudinal wavefunction $\psi(x)$, such as in [5]:

$$\psi_n(\boldsymbol{r}) = \psi_n(x, y, z) = \frac{1}{\sqrt{L_x}}\chi(y, z)\psi(x) \tag{1.4}$$

in which L_x is a normalization length of the system regarding the x direction.

Then, assuming normal incidence of electrons, the transverse components of the electron wavevector are equal to zero and the longitudinal wavefunction $\psi(x)$ in regions I to III can be expressed as:

$$\begin{aligned} \psi_I(x) &= Ae^{ik_1x} + Be^{-ik_1x} \\ \psi_{II}(x) &= Ce^{ik_2x} + De^{-ik_2x} \\ \psi_{III}(x) &= Fe^{ik_1x} \end{aligned} \tag{1.5}$$

Relations among complex coefficients A to F are determined by imposing the continuity boundary conditions on $\psi(x)$ and its first derivative at $x = 0$ and $x = L$.

The aim of this procedure is to obtain an analytic expression for the tunneling probability, or transmission coefficient, which describes the probability of the incident wave to pass through the barrier as a function of its energy. By definition, the tunneling probability is the squared modulus of the transmission Fresnel coefficient, or transmission amplitude $t = F/A$:

$$T = |t|^2 = t \cdot t^* = \frac{F}{A} \cdot \frac{F^*}{A^*}$$

An extended derivation of the final expression is performed in appendix A, section A.1; here, only the final

result is reported:

$$T(E) = \begin{cases} \dfrac{4E(U_0 - E)}{4E(U_0 - E) + U_0^2 \sinh^2\left(\sqrt{\dfrac{2m(U_0 - E)}{\hbar^2}} L\right)} , & E < U_0 \\ \dfrac{4E(E - U_0)}{4E(E - U_0) + U_0^2 \sin^2\left(\sqrt{\dfrac{2m(E - U_0)}{\hbar^2}} L\right)} , & E \geq U_0 \end{cases} \tag{1.6}$$

Equation (1.6) is case-defined in order to maintain a real argument in the square root at denominator.

In addition, when $E \ll U_0$ the expression reduces to a decaying exponential function of the barrier thickness L:

$$T \propto \exp\left\{ -2\sqrt{\frac{2m(U_0 - E)}{\hbar^2}} L \right\} , \qquad E \ll V_0 \tag{1.7}$$

which is the simplified expression used in [3] for each barrier.

Finally, since there are no losses, the reflection probability is complementary to the transmission probability: $R + T = 1$.

These probabilities constitute the *scattering matrix* of the system, relating outgoing wave amplitudes to incoming wave amplitudes. Using an equivalent notation to [4], it is possible to write

$$\begin{pmatrix} B \\ F \end{pmatrix} = \begin{bmatrix} S_{11} & S_{12} \\ S_{21} & S_{22} \end{bmatrix} \cdot \begin{pmatrix} A \\ 0 \end{pmatrix} ; \qquad \boldsymbol{S} = \begin{bmatrix} S_{11} & S_{12} \\ S_{21} & S_{22} \end{bmatrix} \tag{1.8}$$

for the system under analysis. Expanding the product, it is easily proven that $S_{11} = B/A = r$, reflection amplitude, and $S_{21} = F/A = t$, transmission amplitude. The scattering matrix is shown in [4] to be *unitary* to ensure current conservation; while the *reciprocity relation* is satisfied for *coherent* transport, in which no phase-breaking collisions occur.

This means that the final form of the scattering matrix is:

$$\boldsymbol{S} = \begin{bmatrix} S_{11} & S_{12} \\ S_{21} & S_{22} \end{bmatrix} = \begin{bmatrix} r & t \\ t & r \end{bmatrix} \tag{1.9}$$

in which $|r|^2 = R$.

1.1.2 Double-barrier tunneling

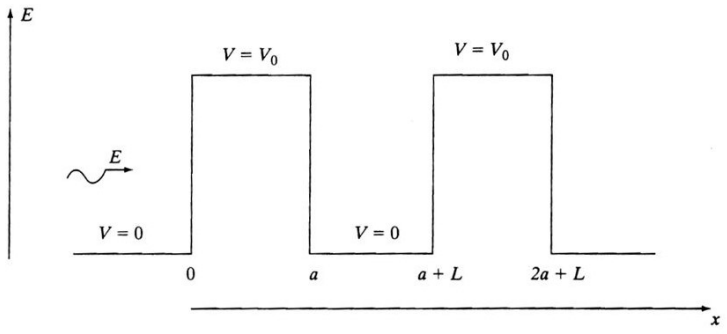

Figure 1.2: Double potential barrier, image taken from [6].

Also in case of a double potential barrier the tunneling probability could in principle be determined from the Schrödinger equation; however, the scattering matrix formalism is a more common approach to the problem which allows to divide the system in sections, and combine their individual scattering matrices to obtain a composite scattering matrix for the whole system, such as in [4] and [7].

Since the scattering matrix for a single potential barrier is known, the transmission probability of a double-barrier system is more easily determined from the single-barrier one.

For a general system of two barriers different from each other, and characterized by scattering matrices respectively

$$\boldsymbol{S}_1 = \begin{bmatrix} r_1 & t_1 \\ t_1 & r_1 \end{bmatrix} , \qquad \boldsymbol{S}_2 = \begin{bmatrix} r_2 & t_2 \\ t_2 & r_2 \end{bmatrix} \tag{1.10}$$

applying the rules for coherent combination of scattering matrices listed in [4], the resulting transmission amplitude is:

$$t = \frac{t_1 t_2}{1 - r_1 r_2} \tag{1.11}$$

which translates into a tunneling probability equal to:

$$T(E) = |t|^2 = t \cdot t^* = \frac{T_1 T_2}{1 - 2\sqrt{R_1 R_2}\cos(\theta) + R_1 R_2} \tag{1.12}$$

where the argument $\theta = 2k(L+a)$ is the sum of the reflection amplitudes' arguments: it represents the phase shift acquired during a round-trip between the barriers.

Here again, only the final result is reported; but a more detailed derivation is found in appendix A, section A.2.

1.2 Landauer-Büttiker formula

The current evaluation relies on the assumption that the contacts through which the current is injected into the system are "reflectionless", i.e. electrons are able to leave the system and enter them without any reflection. This is a reasonable assumption when transmitting from a narrow conductor, such as a nanoparticle, to a wide contact [8], [9].

Starting with a single contact, the current can be evaluated for each transverse conducting mode separately and then all contributions can be added up together, as in [4].

A uniform electron gas constituted of n electrons per unit length moving at velocity v carries a current density equal to:

$$I = env(k) = en\frac{1}{\hbar}\frac{\partial E(k)}{\partial k} , \qquad v(k) = \frac{1}{\hbar}\frac{\partial E(k)}{\partial k} \tag{1.13}$$

Conducting transverse modes in the contacts are determined by the applied voltage difference at the system's ends, which translates into a difference in the contacts' chemical potentials μ_1 and μ_2. At a temperature higher than zero Kelvin degrees, a reasonable assumption is that transverse modes inside the contacts are occupied according to a Fermi-Dirac distribution:

$$f(E-\mu) = \frac{1}{1 + \exp\left\{\dfrac{E-\mu}{k_B T}\right\}} \tag{1.14}$$

With an electron density equal to $(1/L)$, associated with a single transverse k-mode in a conductor of length L, the current becomes:

$$I = \frac{e}{L}\sum_k \frac{1}{\hbar}\frac{\partial E(k)}{\partial k} f(E-\mu) \tag{1.15}$$

summing over all k values. Assuming periodic boundary conditions, and a sufficiently high number of k values, the summation can be converted into an integral:

$$\sum_k \quad \rightarrow \quad 2 \times \frac{L}{2\pi} \int dk \tag{1.16}$$

in which the factor 2 accounts for the spin multiplicity. Then,

$$I = \frac{2e}{L} \frac{L}{2\pi\hbar} \int f(E-\mu) dE = \frac{2e}{h} \int f(E-\mu) dE \tag{1.17}$$

This result can be extended to include several conducting modes:

$$I = \frac{2e}{h} \int f(E-\mu) M(E) dE \tag{1.18}$$

where $M(E)$ is the number of transverse modes above the cut-off energy.

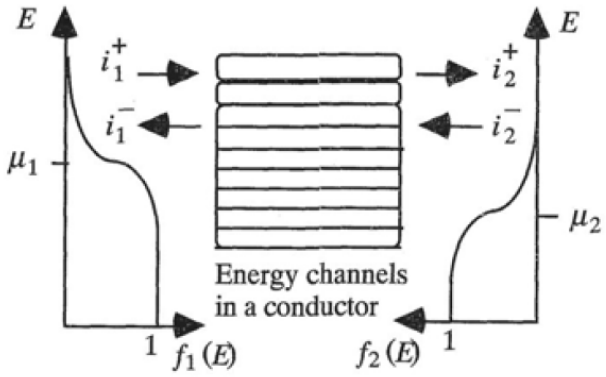

Figure 1.3: Graphical representation for the Landauer-Büttiker formula derivation; image taken from [4].

In equation (1.18), it is assumed that transport only occurs from one contact to the other; however, in general, current can flow also in the opposite direction and the energy of injected electrons is dictated by the applied bias voltage $\mu_1 - \mu_2 = e \cdot V$ via the number of conducting modes each contact has available in that range.

Therefore, contacts are characterized by a certain transmission efficiency $T_{(1,2)}$ of electrons inside the system, and by a certain number $M_{(1,2)}$ of conducting transverse modes, respectively.

Figure 1.3 can be used as a reference, imagining two contacts at the left- and right-hand sides of the system, whose Fermi-Dirac distribution functions of electrons are represented. Current flows entering and leaving the left contact can be expressed as:

$$\begin{cases} i_1^+ = \dfrac{2e}{\hbar} f(E-\mu_1) \dfrac{\partial E(k)}{\partial k} M_1 \\ \\ i_1^- = (1-T_1)\, i_1^+ + T_2 i_2^- \end{cases} \tag{1.19}$$

Similarly, for the right contact:

$$\begin{cases} i_2^- = \dfrac{2e}{\hbar} f(E-\mu_2) \dfrac{\partial E(k)}{\partial k} M_2 \\ \\ i_2^+ = T_1 i_1^+ + (1-T_2)\, i_2^- \end{cases} \tag{1.20}$$

in which the plus and minus signs at apex indicate an electron flow towards the right and left, respectively. The total current density flowing from one contact to the other is given by the balance:

$$i = i_1^+ - i_1^- = i_2^+ - i_2^- = T_1 i_1^+ - T_2 i_2^- = \frac{2e}{\hbar}\frac{\partial E(k)}{\partial k}\left[T_1 M_1 f(E-\mu_1) - T_2 M_2 f(E-\mu_2)\right] \tag{1.21}$$

In the absence of inelastic scattering events inside the system, as stated in [4], it can be proven that $T_1 M_1 = T_2 M_2 = T(E)$ at all temperatures, $T(E)$ being the transmission probability of the system.

Finally, the total current can be evaluated accounting for the contribution of all existing k values within the contacts through an integral, such as in equations (1.16) and (1.17):

$$I = \int i \, \frac{dk}{2\pi} = \frac{2e}{h}\int T(E)\left[f(E-\mu_1) - f(E-\mu_2)\right]\frac{\partial E(k)}{\partial k}\, dk \tag{1.22}$$

Changing the integration variable from the wavevector k to the energy E, the Landauer-Büttiker formula is obtained:

$$I = \frac{2e}{h}\int T(E)\left[f(E-\mu_1) - f(E-\mu_2)\right] dE \tag{1.23}$$

The integral can be allowed to span over all energies since only the energy range in which the difference between Fermi distributions is different from zero is responsible for conduction.

A more rigorous derivation, based on quantum mechanics, of equation (1.23) is given in chapter 2, section 2.2, with the introduction of the current and current density operators.

Chapter 2

Numerical implementation

In order to calculate the current across the double-barrier system according to equation (1.23) the tunneling probability has to be evaluated at each intermediate bias voltage value between $V = 0$ and $V = V_{max}$. In order to do so, equation (1.12) is no longer valid because it has been obtained in an equilibrium condition, in which the left- and right-hand side chemical potentials coincide.

Two methods have been compared to evaluate $T(E)$ outside of equilibrium, the *Finite Element Method* (*FEM*) and the *Non-Equilibrium Green's Functions* (*NEGF*) approaches.

2.1 FEM solution of the Schrödinger equation

This approach aims to numerically solve the Schrödinger equation by deriving an approximate wavefunction in terms of a linear combination of some appropriate basis functions. The bias voltage enters Schrödinger's equation directly, by "tilting" the equilibrium potential energy profile.

Injecting electrons from one contact, the tunneling probability is then evaluated as the squared absolute value of the approximate solving wavefunction at the opposite contact.

2.1.1 Lagrange polynomials as basis functions

As explained in [10], the *FEM* approach needs the domain, in this case a segment $[0, L]$ of the x-axis, to be discretized into a finite number of elements. The problem is defined into N mesh nodes and $N - 1$ sub-intervals. Then, a set of N basis functions is defined to approximate the solution; in particular, first-order Lagrange polynomials have been used:

$$
\begin{aligned}
N_1(x) &= \frac{x_2 - x}{x_2 - x_1}, \quad x_2 \leq x < x_1 \\
N_j(x) &= \begin{cases} \dfrac{x - x_{j-1}}{x_j - x_{j-1}}, & x_{j-1} \leq x < x_j \\ \dfrac{x_{j+1} - x}{x_{j+1} - x_j}, & x_j \leq x < x_{j+1} \end{cases} \qquad j = 2, \ldots, N-1 \\
N_N(x) &= \frac{x - x_{N-1}}{x_N - x_{N-1}}, \quad x_{N-1} \leq x \leq x_N
\end{aligned}
\tag{2.1}
$$

These functions are triangle-shaped and their support is limited only up to their left- and right-hand side adjacent nodes; figure 2.1 shows a simple case with 5 nodes and 4 sub-intervals for a domain $x \in [0, 1]$.

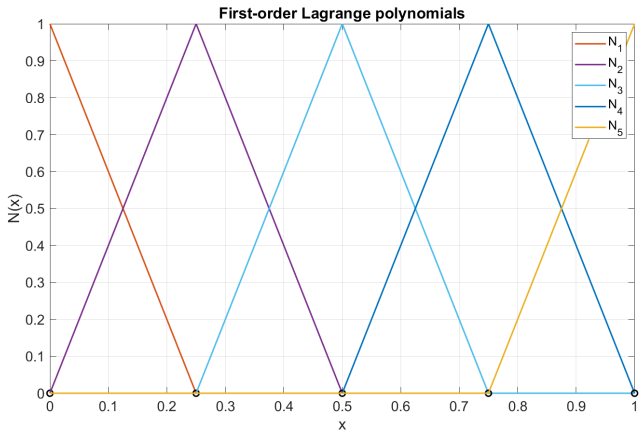

Figure 2.1: First-order Lagrange polynomials with $N = 5$; nodes are shown as black circles on the x-axis.

The electron wavefunction which is the unknown of the problem, is expressed as a linear combination of basis functions, according to Galërkin's procedure:

$$\psi(x) = \sum_{j=1}^{N} c_j N_j(x) = \sum_{j=1}^{N} \psi_j N_j(x) \ , \qquad \psi_j = \psi(x = x_j) \tag{2.2}$$

A property of Lagrange polynomials (2.1) is that they are interpolating functions; therefore, the coefficients c_j are exactly equal to the value of the wavefunction at node x_j.

The limited support of each basis function is an advantage since the inner product between two basis functions N_i, N_j and that of their first derivatives N_i' and N_j' will be zero for almost all i, j pairs. Hence, the integrands in the weak formulation of a problem will be identically equal to zero whenever $|i - j| > 1$.

2.1.2 Weak formulation of Schrödinger's equation

The Schrödinger equation for the one-dimensional system writes:

$$\left[-\frac{\hbar^2}{2m} \frac{d^2}{dx^2} + U(x) \right] \psi(x) = E\psi(x) \tag{2.3}$$

Each term of the equation is multiplied by a weighting function, which is chosen to be equal to the Lagrange polynomial (2.1) used as basis function, and integrated over the whole domain to obtain

$$-\frac{\hbar^2}{2m} \int_0^L N_i(x) \frac{d^2}{dx^2} \psi(x) dx + \int_0^L N_i(x) U(x) \psi(x) dx = E \int_0^L N_i(x) \psi(x) dx \tag{2.4}$$

then, Green's theorem (integration by parts in 1D) is used on the first integral on the left-hand side to reduce by one order the derivative of the wavefunction in the integrand; thus obtaining the weak formulation of Schrödinger's equation:

$$\frac{\hbar^2}{2m} \int_0^L \frac{dN_i}{dx} \frac{d\psi}{dx} dx + \int_0^L N_i(x) U(x) \psi(x) dx = E \int_0^L N_i(x) \psi(x) dx + \frac{\hbar^2}{2m} N_i(x) \frac{d\psi}{dx} \bigg|_0^L \tag{2.5}$$

substituting (2.2) into equation (2.5), applying proper boundary conditions, and taking advantage of the integral's linearity, it is possible to write

$$\frac{\hbar^2}{2m}\sum_{j=1}^{N}\psi_j\underbrace{\int_0^L\frac{dN_i}{dx}\frac{dN_j}{dx}dx}_{K_{ij}}+\sum_{j=1}^{N}\psi_j U_j\underbrace{\int_0^L N_i(x)N_j(x)dx}_{M_{ij}}=E\sum_{j=1}^{N}\psi_j\underbrace{\int_0^L N_i(x)N_j(x)dx}_{M_{ij}}, \tag{2.6}$$

$$i=2,\ldots,N-1$$

for a single mesh point; $U_j=U(x=x_j)$ is equal to a constant at each mesh point and thus it can be moved out of the integral. Due to how Lagrange polynomials are defined, these integrals will be identically equal to zero whenever $|i-j|>1$. In matrix form:

$$\left(\frac{\hbar^2}{2m}[K]_j+U_j[M]_j\right)\{\psi\}_j=E[M]_j\{\psi\}_j \tag{2.7}$$

Then, summing over all mesh points, a generalized eigenvalue equation is obtained:

$$\sum_j\left(\frac{\hbar^2}{2m}[K]_j+U_j[M]_j\right)\{\psi\}=E\sum_j[M]_j\{\psi\} \tag{2.8}$$

Equation (2.8) is the discrete weak formulation of Schrödinger's equation with respect to first-order Lagrange polynomials; the unknown is the set of coefficients $\{\psi\}$ of the expansion (2.2).

Matrices $[K]$ and $[M]$ are commonly referred to as *stiffness* matrix and *mass* matrix, respectively. Since first-order Lagrange polynomials are linear functions, the matrix elements can be computed analytically; their calculation is performed in appendix B.

2.1.3 Boundary conditions

In this model, contacts or electron reservoirs are not an actual part of the domain; but they occupy the regions $x<x_1$ and $x>x_N$ and are defined as fully absorbing elements. Considering electrons to be injected from the left- and right-hand contacts with known wavevectors k_L and k_R, respectively; and allowing them the possibility to be partially reflected inside the contacts, it is possible to write:

$$\begin{aligned} k_L&=\sqrt{\frac{2m\,(E-U_1)}{\hbar^2}} &&,\psi_L(x)=\psi_L^+e^{ik_Lx}+re^{-ik_Lx}\\ k_R&=\sqrt{\frac{2m\,(E-U_N)}{\hbar^2}} &&,\psi_R(x)=te^{ik_Rx}+\psi_R^-e^{-ik_Rx}\end{aligned} \tag{2.9}$$

assuming $+x$ to be the positive propagation direction.

Evaluating (2.9) and their first derivative at the domain's boundaries $x=x_1$ and $x=x_N$, respectively, it is possible to eliminate the reflection and transmission amplitudes r and t, obtaining the mixed boundary conditions:

$$\begin{aligned}\left.\frac{d\psi_L(x)}{dx}\right|_{x_1}&=-ik_L\psi_L(x_1)+2ik_L\psi_L^+e^{ik_Lx_1}\\ \left.\frac{d\psi_R(x)}{dx}\right|_{x_N}&=ik_R\psi_R(x_N)-2ik_R\psi_R^-e^{-ik_Rx_N}\end{aligned} \tag{2.10}$$

Now, continuity of the wavefunctions and of their first derivatives across the device-contact interface can be enforced by using equations (2.10) as the finite-element equations corresponding to the first and last node,

respectively.

Thus, the value of the electron energy is determined by the boundary conditions and the eigenvalue problem (2.8) can be rewritten including them as equations. Starting from a more compact notation for equation (2.8):

$$[H]\{\psi\} = E\,[M]\{\psi\} \tag{2.11}$$

with

$$\begin{aligned} [H] &= \sum_j \left(\frac{\hbar^2}{2m}\,[K]_j + U_j\,[M]_j \right) \\ [M] &= \sum_j [M]_j \end{aligned} \tag{2.12}$$

the system which includes the boundary conditions becomes inhomogeneous and linear:

$$[A]\{\psi\} = \{b\} \tag{2.13}$$

where

$$[A] = E\,[M] - [H] \tag{2.14}$$

is the matrix incorporating the boundary conditions (2.10). $\{b\}$ is the known vector whose elements are all equal to zero, except for the first one which acts as a stimulus for the system according to the boundary conditions. The aim is obtaining the system's transmission probability; for this purpose, incoming electrons are assumed to be coming from the left contact, hence $\psi_L^+ = 1$ and $\psi_L^- = 0$.

Finally, the system of equations (2.13) can be solved by direct approaches for linear systems. A schematic pseudocode of the solving algorithm is shown in the following section.

2.1.4 Pseudocode of the FEM solving algorithm

Algorithm 1: Solution procedure by FEM

Data: x, *Energy*, *Bias*, U_{eq}
Result: Current I
Initialization;
for *Bias* **do**
  $U = U_{eq} + q \cdot Bias$;
  $\mu_1 = E_F + q \cdot Bias/2$;
  $\mu_2 = E_F - q \cdot Bias/2$;
  for x **do**
    Define FEM matrices;
    H = stiffness matrix;
    M = mass matrix;
  end
  for *Energy* **do**
    $A = Energy \cdot M - H$;
    $A(1,1) = A(1,1)$ + boundary conditions of the left-hand contact;
    $A(end, end) = A(end, end)$ + boundary conditions of the right-hand contact;
    b = known vector whose elements are equal to zero;
    $b(1)$ = stilumus to the system according to the boundary conditions;
    $\psi = A \setminus b$;
    $T(Energy) = \mathrm{abs}\left(\psi(end)\right)^2$;
  end
  $I(Bias) = \dfrac{2e}{h} \int T(Energy) \left[f(Energy - \mu_1) - f(Energy - \mu_2) \right] dE$;
end

2.1.5 Model testing

Analytic equations (1.6) for tunneling across a single barrier and (1.12) for a double barrier are valid for a system in equilibrium conditions, in which no bias voltage is applied that would tilt the potential energy profile in one direction; therefore, in order to validate the numerical solution of Schrödinger's equation, and compare it to the analytic formulas presented in chapter 1, the finite element model has been used to solve Schrödinger's equation for a fixed potential energy profile. The incident electron kinetic energy has been modified like an independent variable in order to evaluate the tunneling probability as a function of the particle energy. At each iteration, the whole procedure is repeated after updating the potential energy profile according to the applied bias voltage.

As a reminder, the FEM model approximates the wavefunction solution of the Schrödinger equation using a set of basis functions, equations (2.1) in this particular case. Then, the FEM tunneling probability can be derived from the squared absolute value of the approximate wavefunction evaluated at the opposite end of the domain with respect to the electron injection point. The process is repeated to build a tunneling probability as a function of the incident electron energy:

$$T(E) = |\psi(x = x_N, E)|^2 = |\psi_N(E)|^2 \tag{2.15}$$

The software used for all the simulations and numerical computations is MATLAB 2020a build.

Figures 2.2 and 2.3 show the comparison between FEM solution and the analytic equations (1.6) and (1.12), respectively; together with the potential energy profile provided to the Schrödinger equation.

In the single-barrier case the agreement between the results is nearly perfect, so that no difference is noticeable to the naked eye and the difference between curves is found to be of the same order of magnitude as MATLAB's machine precision, which is 10^{-16}. At first, the tunneling probability increases exponentially with the electron energy, then it stabilizes to values close to unity for $E > U_0$.

The double-barrier case shows also a good agreement with the analytic expression, especially in the lower energy range where the curves nearly coincide, until E slightly exceeds U_0. This range is the most relevant in terms of Coulomb blockade because it is the range in which confinement effects can be observed.

In particular, two peaks of transmission are present for electron energies such as $E < U_0$. This suggests the presence of two confined energy levels between the barriers which allow electrons whose energy is compatible to transit across them with probability nearly equal to one. As E becomes larger than U_0, the tunneling probability quickly stabilizes to values close to unity, with a few oscillations.

For $E \gtrapprox 0.75\ eV$ the analytic and FEM curves start to slightly differentiate from each other; however, this should not be a cause of concern for this work because Coulomb blockade phenomenon is mainly observed for energies such that confined levels are present in between the barriers.

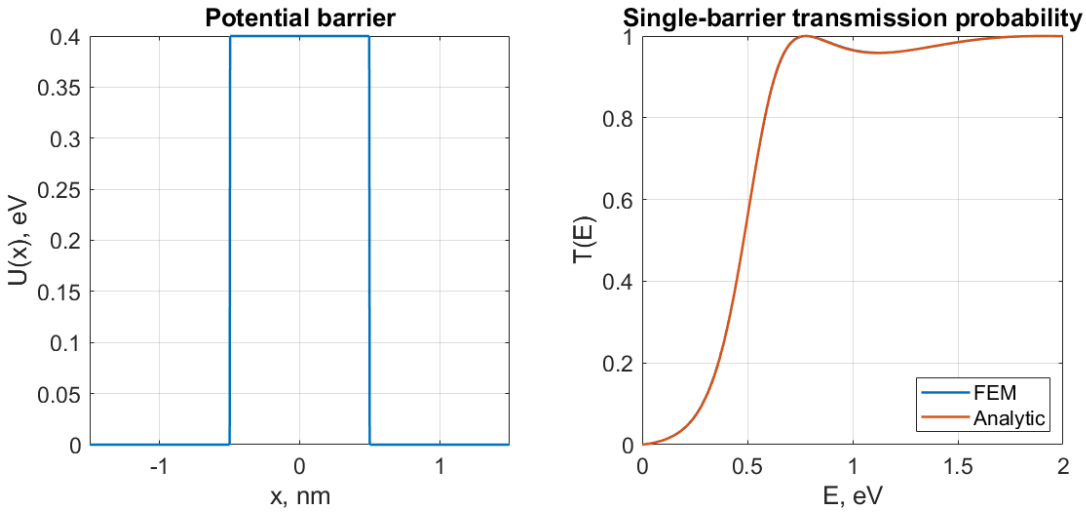

Figure 2.2: Single-barrier tunneling probability comparison, analytic and FEM.

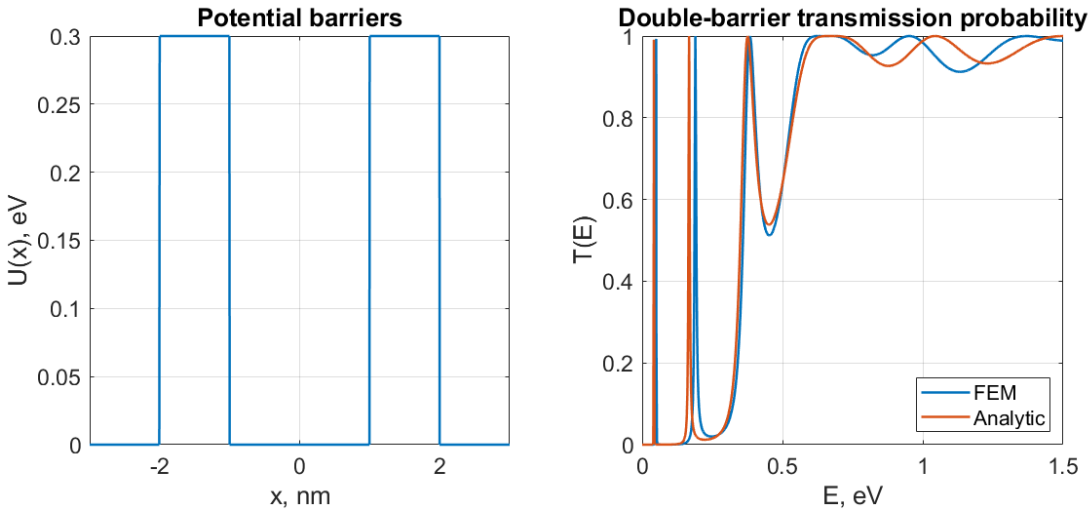

Figure 2.3: Double-barrier tunneling probability comparison, analytic and FEM.

2.1.6 Simulations with bias voltage

Since preliminary tests and comparisons with the analytic equilibrium formulas produced satisfactory results, the FEM model has been generalized to include the presence of a progressively increasing bias voltage between the two contacts.

The voltage drop between the them is assumed to be linearly distributed across the system, such as shown in figure 2.4, which is an example taken from the simulation of the system in figure 2.3, and applies a 1V-bias across the barriers. The effect of a bias voltage is included inside the solving algorithm directly in Schrödinger's equation, as it can be summed to the potential energy, thus "tilting" the energy profile of the system in one direction along the x-axis.

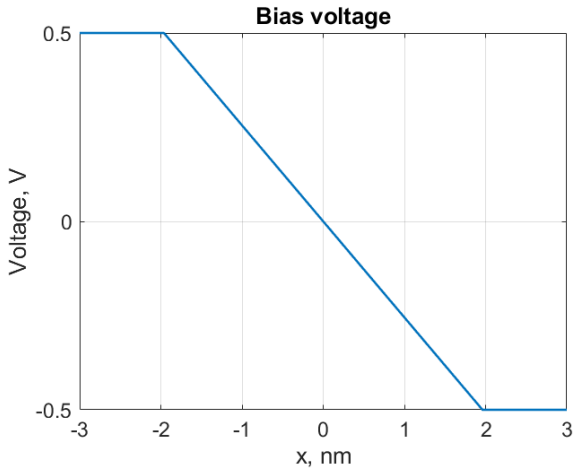

Figure 2.4: 1V, linear voltage between the contacts.

Therefore, for each iteration on the bias voltage a FEM system of equations in the form (2.13) is solved and a new transmission probability is derived via equation (2.15); then, the Landauer-Büttiker formula (1.23) is used to obtain a current value, corresponding to the static current flowing through the system for that

particular value of applied voltage. At the end of the procedure, an I-V characteristics is constructed.

Unfortunately, the implementation which was expected to work even outside of equilibrium proved to be inadequate for bias voltages higher than approximately $0.1\ V$, independently of the simulated system. This issue has been at first spotted in the current I-V characteristics: although it showed an overall exponential trend as expected, it also presented neither steps nor negative differential conductance regions which are features of the Coulomb blockade phenomenon.

After a more careful analysis, the issue has been identified in the tunneling probability derived by the FEM model; as a reminder, the transmission probability is here calculated via equation (2.15).

By definition of a particle's wavefunction, its squared absolute value should have a maximum value of one, since it represents a probability; instead, as shown in figure 2.5, which is the same case presented in figure 2.3, the first tunneling peak reaches above one for bias voltages higher than approximately $0.1\ V$ and, as the applied voltage further increases, this trend becomes more and more prevalent. Moreover, the other peaks follow soon after in this physically meaningless behaviour.

As it has already been stated, the breaking point seems to be around $0.1\ V$, which is when the decreasing trend of the first peak starts to invert. As a consequence, the integral in the Landauer-Büttiker formula (1.23) starts to increase and the current soon diverges to senseless values.

For these reasons, a more sophisticated but also much more computationally expensive model has been experimented with, which is the *Non-Equilibrium Green's Functions* approach, often shortened to *NEGF*. This model is presented in section 2.2.

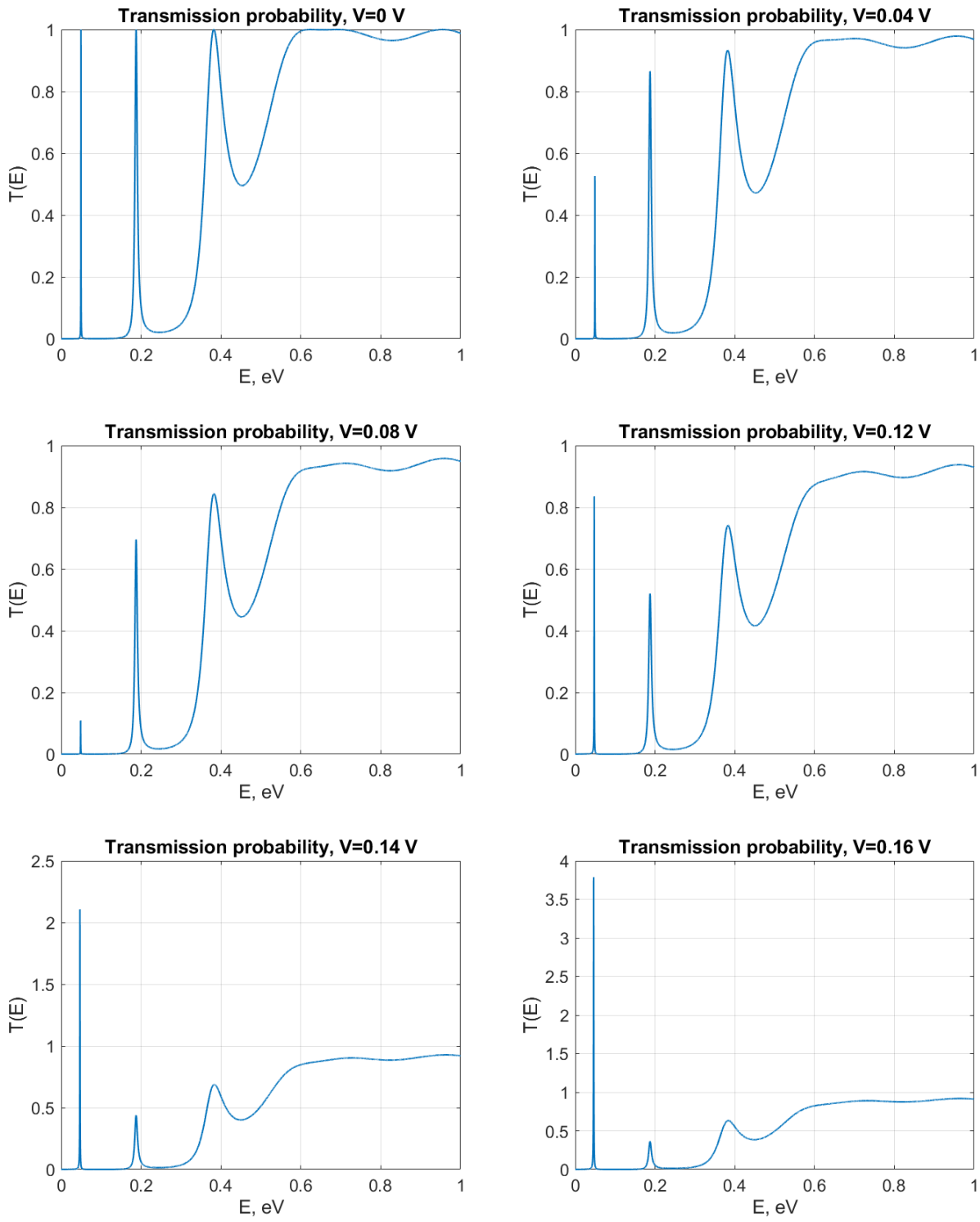

Figure 2.5: FEM transmission probability, evolution with increasing bias.

2.2 NEGF formalism

An introduction to Green's functions can be found in [11]. For non-interacting transport this approach is closely related to the scattering matrix concept presented in section 1.1 for the tunneling across a double potential barrier.

However, the NEGF formalism provides a microscopic theory of quantum transport beyond the ballistic limit considered here: interactions such as electron-phonon ones give rise to excitations inside the conductor that cannot be modelled by simple scattering matrices.

Using the notation found in [4], the concept of Green's function appears in many physical contexts and, in general, it is applicable whenever the response R of a system is related to the excitation S through a differential operator D_{op}:

$$D_{op}R = S \tag{2.16}$$

Defining a Green's function, the response can be expressed as:

$$R = D_{op}^{-1}S \ , \qquad G \equiv D_{op}^{-1} \tag{2.17}$$

In particular, a one-particle Schrödinger-like problem can be formulated as:

$$[E - H]\,\psi(\boldsymbol{r}) = S \tag{2.18}$$

so that

$$G(\boldsymbol{r}, E) = [E - H]^{-1} = \left(E - U(\boldsymbol{r}) + \frac{\hbar^2}{2m}\nabla^2\right)^{-1} \tag{2.19}$$

in which H is the Hamiltonian operator and E the energy eigenvalue.

2.2.1 Retarded and advanced Green's functions

Since the inverse of a differential operator is not uniquely defined until the boundary conditions are specified, it is common to define two different Green's functions; they are usually referred to as *retarded* and *advanced* Green's functions, respectively.

The difference can be highlighted with a simple example. Considering a one-dimensional system, and using equation (2.19) it is possible to write

$$\left(E - U(x) + \frac{\hbar^2}{2m}\frac{d^2}{dx^2}\right) G(x, x') = \delta(x - x') \tag{2.20}$$

which resembles a Schrödinger equation for the Green's function, except for the excitation source term $\delta(x - x')$ on the right-hand side of the equation.

Therefore, the Green's function can be seen as the wavefunction evaluated at x due to a point-like source placed at x'. This excitation is expected to give rise to two propagating waves outgoing from the point x': one directed towards the positive x-direction, and one directed towards the negative x-direction.

In order to satisfy equation (2.20), the two solutions must be continuous at $x = x'$ while their first derivative must be discontinuous at the same point. This allows to obtain an expression for the Green's function:

$$G^R(x, x') = -\frac{i}{\hbar v}\exp\{ik\,|x - x'|\} \ , \qquad v = \frac{\hbar k}{m} \ , \quad k = \sqrt{\frac{2m(E - U(x))}{\hbar^2}} \tag{2.21}$$

which is commonly named *retarded* Green's function; however, there is also another viable solution that satisfies (2.20):

$$G^A(x, x') = \frac{i}{\hbar v}\exp\{-ik\,|x - x'|\} \ , \qquad v = \frac{\hbar k}{m} \ , \quad k = \sqrt{\frac{2m(E - U(x))}{\hbar^2}} \tag{2.22}$$

which is called *advanced* Green's function. In both equations (2.21) and (2.22) v is the particle velocity, and k its wavenumber.

Both these solutions satisfy equation (2.20), but they correspond to different boundary conditions: G^R corresponds to outgoing waves originating at x'; while G^A corresponds to incoming waves originating far away from the source.

In addition, knowing that G^R and G^A are both bounded linear operator, it is possible to deduce that the retarded and advanced Green's functions are one the Hermitian conjugate of the other. In formula, it can be written as:

$$\left(G^A\right) = \left(G^R\right)^\dagger \tag{2.23}$$

2.2.2 The infinitesimal η

One method to incorporate the boundary conditions into equation (2.20) is to add an infinitesimal imaginary part to the energy. Writing the equation for the retarded Green's function:

$$\left(E - U(x) + \frac{\hbar^2}{2m}\frac{d^2}{dx^2} + i\eta\right) G^R(x, x') = \delta(x - x') \ , \qquad \eta > 0 \tag{2.24}$$

the imaginary part $i\eta$ introduces a positive imaginary component to the wavenumber k, which makes the solution grow indefinitely far away from the excitation point x':

$$k' = \sqrt{\frac{2m(E - U(x) + i\eta)}{\hbar^2}} \approx \sqrt{\frac{2m(E - U(x))}{\hbar^2}} \left[1 + \frac{i\eta}{2(E - U(x))}\right] = k(1 + i\delta) \tag{2.25}$$

As a consequence, G^R is the only solution that remains bounded and is considered acceptable.

Similarly, the equation for the advanced Green's function is:

$$\left(E - U(x) + \frac{\hbar^2}{2m}\frac{d^2}{dx^2} - i\eta\right) G^R(x, x') = \delta(x - x') \ , \qquad \eta > 0 \tag{2.26}$$

Therefore, in general, the definition of Green's functions (2.19) is split into two: G^R and G^A are defined as

$$G^R = [E - H + i\eta]^{-1} \tag{2.27}$$

and

$$G^A = [E - H - i\eta]^{-1} \tag{2.28}$$

respectively, with $\eta \to 0^+$.

2.2.3 Matrix formulation for the numerical solution

The procedure to derive the Green's functions involves the solution of equation (2.20), and a common approach to solve this kind of differential equations is to discretize the spatial coordinate so that the Green's functions become matrices. Taking the retarded Green's function as an example:

$$G^R(x, x') \quad \to \quad G^R(i, j) \tag{2.29}$$

and the differential equation (2.20) becomes a matrix equation. According to [12], the same matrices $[H]$ and $[M]$ derived in section 2.1 for the FEM solution of Schrödiner's equation can be used for this purpose; dropping the square brackets when referring to them to simplify the notation, equation (2.20) becomes:

$$\left[(E + i\eta)\, M - H\right] \left[G^R\right] = [I] \tag{2.30}$$

in which $[I]$ is the identity matrix.
The retarded Green's function can be obtained inverting equation (2.30) numerically:

$$\left[G^R\right] = \left[(E + i\eta)\, M - H\right]^{-1} \tag{2.31}$$

At this point, boundary conditions are yet to be explicitly derived: they are not introduced by substituting the first and last elements of matrices $[H]$ and $[M]$, such as in section 2.1, but they are implicitly contained in the infinitesimal η. An explicit expression will be derived shortly.

2.2.4 Matrix truncation and *self-energy* term

In principle, equation (2.20) spans over the entire x-axis; thus, its matrix form (2.30) should deal with infinite-dimensional matrices since the system is open and connected to leads that stretch out to infinity.

However, the system must have a finite number of equations in order to be solved by a calculator; therefore, matrices have to be truncated at some point along the x-axis.

The truncation has to be performed with particular care since simply truncating the matrices would result into the system being transformed into a close one with fully reflecting boundaries. Thus, the truncations must be done in a way that maintains the system open and with non-reflecting boundary conditions, such as in section 2.1 for the FEM implementation.

The solution provided by [4] and [11] involves the partition of the overall Green's function into sub-matrices:

$$G^R = \begin{bmatrix} G^R_D & G^R_{DR} \\ G^R_{RD} & G^R_R \end{bmatrix} = \begin{bmatrix} (E + i\eta)\, M_D - H_D & -\tau \\ -\tau^\dagger & (E + i\eta)\, M_R - H_R \end{bmatrix}^{-1} \tag{2.32}$$

in which $\tau = H_{DR}$ is the coupling Hamiltonian between lead and conductor. In this format, G^R_D represents the isolated lead and G^R_R the isolated conductor. Off-diagonal terms are different from zero only for nodes in the conductor which are adjacent to the leads; hence, in a two-terminal device, only the first one and the last one.

The sub-matrix G^R_R is the most relevant part since it is the part describing the system under analysis and is the only part that needs solving.

Starting from the partition (2.32) and using matrix identities such as (2.30), it is possible to write:

$$\begin{cases} \left[(E + i\eta)\, M_D - H_D\right] G^R_{DR} - \tau G^R_R = 0 & (2.33) \\ \left[(E + i\eta)\, M_R - H_R\right] G^R_R - \tau^\dagger G^R_{DR} = I & (2.34) \end{cases}$$

Then,

$$G^R_{DR} = \left[(E + i\eta)\, M_D - H_D\right]^{-1} \tau\; G^R_R\,, \qquad \left[(E + i\eta)\, M_D - H_D\right]^{-1} = g^R_R \tag{2.35}$$

derives from equation (2.33), and by substituting it into equation (2.34) an expression for the system Green's function is obtained:

$$\begin{aligned} &\left[(E + i\eta)\, M_R - H_R\right] G^R_R - \tau^\dagger g^R_R \tau\; G^R_R = I \quad \Rightarrow \\ \Rightarrow \quad &\left[(E + i\eta)\, M_R - H_R - \tau^\dagger g^R_R \tau\right] G^R_R = I \end{aligned} \tag{2.36}$$

Finally, naming $\tau^\dagger g^R_R \tau = \Sigma^R$, the truncated matrix equation to be solved is:

$$G^R_R = \left[E M_R - H_R - \Sigma^R\right]^{-1} \tag{2.37}$$

Equation (2.37) is also known as *Dyson's equation*; it shows that the effect of the infinite leads is taken into account in the term Σ^R, also called *self-energy*. This means that the contacts Hamiltonian is "folded"

into the device Hamiltonian; this concept allows to eliminate the infinite leads and work only in the device sub-space whose dimensions are substantially smaller.

The self-energy can be viewed as an *effective* Hamiltonian arising from the interaction of the conductor with the contacts. A similar term is often used to account for the interaction between electrons with phonons in systems that require these kinds of interactions; hence, by analogy, Σ^R is the self-energy due to the leads.

The presence of infinite leads is taken into account exactly through the term $\tau^\dagger g_R^R \tau$, in which g_R^R represents the Green's function for an isolated contact and can usually be derived analytically.

Unlike η, Σ^R is not necessarily an infinitesimal; that is why η has been neglected in equation (2.37).

Finally, assuming different leads to be independent of one another, their effects are additive and a total self-energy can be obtained as a summation of the individual ones of each lead:

$$\Sigma^R = \sum_p \Sigma_p^R \tag{2.38}$$

This assumption is reasonable due to the starting hypothesis on lead-conductor coupling terms being different from zero only for nodes which are adjacent to the leads.

From here on, G^R will be used to denote G_R^R since it is the only Green's function containing relevant information on the system under analysis. An equivalent notation will be used when referring to the FEM stiffness and mass matrices, $[H_R]$ and $[M_R]$, that will be simply denoted as $[H]$ and $[M]$, respectively.

2.2.5 Transmission function and current

It is shown in [4] that having an expression for the Green's function, the individual scattering matrix elements of the system can be derived through the *Fisher-Lee relation* and, with those, the transmission function of electrons across the system. Scattering matrix and the Green's functions-based methods are proven to be exactly equivalent in [13].

The Fisher-Lee relation writes:

$$s_{nm} = -\delta_{nm} + i\hbar\sqrt{v_n v_m} \iint \chi_n(y_q) \left[G_{qp}^R(y_q; y_p)\right] \chi_m(y_p)\, dy_q dy_p \tag{2.39}$$

in which v is the electron velocity, and $\chi(y)$ its transverse component of the electron wavefunction, according to the factorization (1.4).

Finally, the transmission function for a two-terminal device can be expressed in compact form as:

$$T(E) = Tr[\Gamma_1 G^R \Gamma_2 G^A] \tag{2.40}$$

in which *Tr* stands for *trace* operator, and the elements of matrices $\Gamma_{(1,2)}$ can be expressed in terms of the self-energies due to individual leads:

$$\Gamma_{(1,2)} = i\left[\Sigma_{(1,2)}^R - \Sigma_{(1,2)}^A\right] \tag{2.41}$$

in which the advanced self-energy Σ^A is the Hermitian conjugate of the retarded self-energy Σ^R. $\Gamma_{(1,2)}$ are called *broadening functions* and represent the coupling between conductor and leads.

Having a way to derive the transmission function of the system from Green's functions and self-energies such as in equation (2.40), the current can be calculated via the Landauer-Büttiker formula (1.23) presented in section 1.2.

In order to prove equation (2.40) and the validity of the Landauer-Büttiker formula to derive the total current, a few more quantities need to be defined; namely, the *spectral function* and *lesser* and *greater* Green's functions, which will be discussed in the following sections.

2.2.6 Density matrix, spectral function and local density of states

In the simplified description presented in [11], the attention is focused on the coherent transport in steady-state regime. Under these assumptions, at equilibrium, the electron concentration is obtained by filling up the eigenstates $\psi_j(x)$ of Schrödinger's equation according to the Fermi-Dirac distribution (1.14):

$$n(x) = \sum_{\alpha} \left[|\psi_\alpha(x)|^2 \, f(E_\alpha - \mu) \right] \tag{2.42}$$

When a bias voltage is applied, contacts are at a different chemical potential μ such as depicted in section 1.2 when discussing the Landauer-Büttier formula: the left-hand lead is assumed to inject a thermal equilibrium flux of electrons into the device; some are reflected and some transmitted to the right-hand lead. An analogous argument applies to the right-hand lead, and leads are assumed to be perfect absorbers.

At the leads the solution is a known Fermi function; however, inside the device states α, β are occupied in a *correlated* manner which is described by a density matrix:

$$\rho(r, r') = \sum_{\alpha,\beta} \left[\psi_\alpha(x) \tilde{\rho}_{\alpha\beta} \psi_\beta(x') \right] \tag{2.43}$$

In the eigenstate representation, the equilibrium density matrix for $k_{/\!/} = 0$, such as in this description, assumes the form:

$$[\tilde{\rho}] = \begin{bmatrix} f(E_1 - \mu) & 0 & 0 & \dots \\ 0 & f(E_2 - \mu) & 0 & \dots \\ 0 & 0 & f(E_3 - \mu) & \dots \\ \dots & \dots & \dots & \dots \end{bmatrix} \tag{2.44}$$

in which E_j are the eigenvalues of the Hamiltonian H.

To obtain the diagonal density matrix $[\rho]$ in real space coordinates a unitary transformation is required:

$$[\rho] = [V] \, [\tilde{\rho}] \, [V]^\dagger \tag{2.45}$$

in which $[V]$ are matrices whose column vectors are the eigenvectors of $M^{-1/2} H M^{-1/2}$; H and M are the FEM stiffness and mass matrices, respectively, as derived in section 2.1.

Hence, equation (2.45) can be written in compact form as:

$$[\rho] = \int f(E - \mu) \delta([EM - H]) \, dE \tag{2.46}$$

in which δ denotes a Kronecker delta; substituting the expression:

$$2\pi\delta(x) = \lim_{\epsilon \to \eta} \left(\frac{2\epsilon}{x^2 + \epsilon^2} \right) = \frac{i}{x + i\eta} - \frac{i}{x - i\eta} \, , \qquad \eta \to 0^+ \tag{2.47}$$

into equation (2.46), is possible to write:

$$[\rho] = \int f(E - \mu) \frac{i}{2\pi} \left(\left[(E + i\eta) M - H \right]^{-1} - \left[(E - i\eta) M - H \right]^{-1} \right) \, dE =$$

$$= \int f(E - \mu) \left[\mathcal{A}(E) \right] \frac{dE}{2\pi} \tag{2.48}$$

in which the retarded and advanced Green's functions can be recognized, expressed in their matrix form with respect to equations (2.27) and (2.28), respectively. Finally, it is possible to define the spectral function $[\mathcal{A}(E)]$ as:

$$[\mathcal{A}(E)] = i \left(\left[(E + i\eta) M - H \right]^{-1} - \left[(E - i\eta) M - H \right]^{-1} \right)$$

$$= i \left(\left[G^R(E) \right] - \left[G^A(E) \right] \right) \tag{2.49}$$

In particular, $[\mathcal{A}(E)]/2\pi$ is the real-space representation of the local density of states.

In general, mesoscopic conductors often display significant spatial variations in the local density of states which, in turn, translates into a unique nature of conduction through the sample.

2.2.7 A more rigorous definition of the one-particle Green's functions

A more rigorous definition of the one-particle Green's functions can be found in [9], [12] and [14]. However, in many-bodies theory a Green's functions describes the quantum statistical ensemble average associated to a pair of creation-annihilation operators, and they are useful in solving perturbation theory problems [15]. For non-interacting systems of particles the many-bodies Green's functions are equivalent to the one-particle Green's functions; this will be used to justify equation (2.40) and the Landauer-Büttiker (1.23) formula for the current calculation [9], [12].

The addition of a perturbation to the time-independent one-particle Schödinger equation (1.1) can be written as:

$$[H_0(\boldsymbol{r}) + W(\boldsymbol{r})]\,\psi_n(\boldsymbol{r}) = E_n\psi_n(\boldsymbol{r}) \tag{2.50}$$

in which $H_0(\boldsymbol{r})$ is the unperturbed Hamiltonian, simply denoted as $H(\boldsymbol{r})$ in equation (1.1), and $W(\boldsymbol{r})$ is the perturbation for the system.

The differential equation for the Green's function is written as in equation (2.20); substituting it into (2.50), Schrödinger's equation can be rewritten as:

$$\left[G_0^{-1}(\boldsymbol{r}, E) - W(\boldsymbol{r})\right]\psi_n(\boldsymbol{r}) = 0 \tag{2.51}$$

in which the zero at subscript of the Green's function is specified to highlight this is the Green's function of the unperturbed system.

The solution of equation (2.51) is found by inspection; it takes the form:

$$\psi_n(\boldsymbol{r}) = \psi_n^0(\boldsymbol{r}) + \int G_0(\boldsymbol{r}, \boldsymbol{r}', E)W(\boldsymbol{r}')\psi_n(\boldsymbol{r}')\; d\boldsymbol{r}' \tag{2.52}$$

and can be verified by inserting $\psi_n(\boldsymbol{r})$ into equation (2.51), and then using (2.20). The integral in equation (2.52) can be solved by iteration and, up to first order in W, the solution is:

$$\psi_n(\boldsymbol{r}) = \psi_n^0(\boldsymbol{r}) + \int G_0(\boldsymbol{r}, \boldsymbol{r}', E)W(\boldsymbol{r}')\psi_n^0(\boldsymbol{r}')\; d\boldsymbol{r}' + \mathcal{O}\left(W^2\right) \tag{2.53}$$

in which ψ_n^0 is an eigenfunction of H_0, with energy E_n. This iterative procedure is just the solution method for the ordinary, non-degenerate perturbation theory.

Including the time dependence into Schrödinger's equation as well as a perturbation $W(\boldsymbol{r})$ to the Hamiltonian $H_0(\boldsymbol{r})$, it is possible to write:

$$\left[i\frac{\partial}{\partial t} - H_0(\boldsymbol{r}) - W(\boldsymbol{r})\right]\psi_n(\boldsymbol{r}, t) = 0 \tag{2.54}$$

Analogously to equation (2.20), the differential equations for the Green's functions are:

$$\left[i\frac{\partial}{\partial t} - H_0(\boldsymbol{r})\right]G_0(\boldsymbol{r}, \boldsymbol{r}'; t, t') = \delta(\boldsymbol{r} - \boldsymbol{r}')\delta(t - t') \tag{2.55}$$

$$\left[i\frac{\partial}{\partial t} - H_0(\boldsymbol{r}) - W(\boldsymbol{r})\right]G(\boldsymbol{r}, \boldsymbol{r}'; t, t') = \delta(\boldsymbol{r} - \boldsymbol{r}')\delta(t - t') \tag{2.56}$$

for the unperturbed and perturbed cases, respectively.

Proceeding as in the time-independent case, equation (2.55) is substituted into the time-dependent Schrödinger equation (2.54) and the solution is found by inspection; in particular, the wavefunction can be equivalently expressed either in terms of G_0 or G as:

$$\psi_n(\boldsymbol{r},t) = \psi_n^0(\boldsymbol{r},t) + \int d\boldsymbol{r}' \int dt' G_0(\boldsymbol{r},\boldsymbol{r}';t,t')W(\boldsymbol{r}')\psi_n(\boldsymbol{r}',t') \tag{2.57}$$

$$\psi_n(\boldsymbol{r},t) = \psi_n^0(\boldsymbol{r},t) + \int d\boldsymbol{r}' \int dt' G(\boldsymbol{r},\boldsymbol{r}';t,t')W(\boldsymbol{r}')\psi_n^0(\boldsymbol{r}',t') \tag{2.58}$$

As for the static case, the solution can be iterated up to any order in W.

The time-dependent Green's function $G(\boldsymbol{r},\boldsymbol{r}';t,t')$ is often also called a *propagator*: if the wavefunction is known at some time t', then the wavefunction at later times can be derived as:

$$\psi_n(\boldsymbol{r},t) = \int d\boldsymbol{r}' \int dt' G(\boldsymbol{r},\boldsymbol{r}';t,t')\psi_n(\boldsymbol{r}',t') \tag{2.59}$$

which can be verified by substituting equation (2.59) into Schrödinger's equation (2.54), and then using (2.56). An equivalent way to express the Green's function, which better demonstrates it is indeed a quantum mechanical propagator, is:

$$G(\boldsymbol{r},\boldsymbol{r}';t,t') = -i\theta\,(t-t')\,\langle \boldsymbol{r}|\, e^{-iH(t-t')}\,|\boldsymbol{r}'\rangle \tag{2.60}$$

which is also solution of (2.56). Equation (2.60) expresses the amplitude for the particle to be in state $|\boldsymbol{r}\rangle$ at time t, given that it was in state $|\boldsymbol{r}'\rangle$ at time t'.

2.2.8 Single-particle Green's function of many-body systems

When defining the Green's functions of many-body systems, it is not immediately clear that they are solutions to differential equations such as for the one-particle Green's functions defined starting from the Schrödinger equation.

Furthermore, in many-body systems it is convenient to define additional Green's functions rather than working only with the retarded and advanced ones.

The retarded Green's function takes the form:

$$G^R(\boldsymbol{r},\boldsymbol{r}';t,t') = -i\theta\,(t-t')\left\langle \left[\Psi(\boldsymbol{r},t),\Psi^\dagger(\boldsymbol{r}',t')\right]_{(B,F)}\right\rangle \tag{2.61}$$

in which $\Psi(\boldsymbol{r},t)$ is used to denote the field operator that generates a particle in position $\boldsymbol{r}$ and time t, θ is a Heaviside step function, and the anti-commutator is defined as

$$\begin{aligned}[A,B]_B &= AB - BA \\ [A,B]_F &= AB + BA\end{aligned} \tag{2.62}$$

and B, F stand for bosons and fermions, respectively. Equation (2.61) is indeed identical to equation (2.60) for non-interacting systems of particles, and equation (2.23) continues to hold between retarded and advanced Green's functions.

It is convenient to define two more Green's functions, named *greater* and *lesser* Green's functions:

$$G^>(\boldsymbol{r},\boldsymbol{r}';t,t') = -\,i\left\langle \Psi(\boldsymbol{r},t)\cdot\Psi^\dagger(\boldsymbol{r}',t')\right\rangle \tag{2.63}$$

$$G^<(\boldsymbol{r},\boldsymbol{r}';t,t') = -\,i\,(\pm 1)\left\langle \Psi^\dagger(\boldsymbol{r}',t')\cdot\Psi(\boldsymbol{r},t)\right\rangle \tag{2.64}$$

so that the retarded and advanced Green's functions can be expressed also as:

$$G^R(\boldsymbol{r},\boldsymbol{r}';t,t') = \theta(t-t')\left[G^>(\boldsymbol{r},\boldsymbol{r}';t,t') - G^<(\boldsymbol{r},\boldsymbol{r}';t,t')\right] \tag{2.65}$$

$$G^A(\boldsymbol{r},\boldsymbol{r}';t,t') = \theta(t'-t)\left[G^<(\boldsymbol{r},\boldsymbol{r}';t,t') - G^>(\boldsymbol{r},\boldsymbol{r}';t,t')\right] \tag{2.66}$$

It is straightforward to show that $G^R - G^A = G^> - G^<$; moreover, equation (2.23) holds between G^R and G^A, while a similar one holds between $G^>$ and $G^<$:

$$G^> = -\left(G^<\right)^\dagger \tag{2.67}$$

which reduces the number of independent Green's functions to two.

In particular, the lesser Green's function is also referred to as *correlation function* for electrons; similarly to the density matrix, which generalizes the concept of a distribution function, such as the Fermi-Dirac distribution, including additional information on the phase correlation, the lesser Green's function generalizes the concept of density matrix adding information on the correlation between the amplitude of a particle's wavefunction in state $|\boldsymbol{r}\rangle$ at time t and that in state $|\boldsymbol{r}'\rangle$ at time t'. The density matrix $\rho(\boldsymbol{r},\boldsymbol{r}';t)$ can be seen as a subset of the lesser Green's function for $t' = t$:

$$\rho(\boldsymbol{r},\boldsymbol{r}';t) = \left[G^<(\boldsymbol{r},\boldsymbol{r}';t,t')\right]_{t'=t} \tag{2.68}$$

Assuming the particles to be in thermal equilibrium, and focusing on stationary states within the systems, it is possible to express the Green's functions in terms of the time difference $t - t'$ rather than the individual times t and t'. This allows to more conveniently express the Green's functions in the energy domain rather than in time, which can be achieved with a Fourier transform of the Green's functions:

$$G^\alpha(\boldsymbol{r},\boldsymbol{r}';E) = \int G^\alpha(\boldsymbol{r},\boldsymbol{r}';t)e^{iEt/\hbar}\,dt \tag{2.69}$$

in which α can stand for any of R, A, $>$ or $<$.

In the energy representation, relation (2.68) becomes an integral over the energy variable:

$$\rho(\boldsymbol{r},\boldsymbol{r}';t) = \left[G^<(\boldsymbol{r},\boldsymbol{r}';t,t')\right]_{t'=t} = \int \frac{1}{2\pi} G^<(\boldsymbol{r},\boldsymbol{r}';E)\,dE \tag{2.70}$$

Thus, diagonal elements of the lesser Green's function represent the number of electrons occupying a particular state, such as in (2.44), and equation (2.70) can be used to write the electron density as:

$$n(\boldsymbol{r}) = \left[G^<(\boldsymbol{r},\boldsymbol{r}';t,t')\right]_{\boldsymbol{r}'=\boldsymbol{r},t'=t} = \int \frac{1}{2\pi} G^<(\boldsymbol{r},\boldsymbol{r};E)\,dE \tag{2.71}$$

Relation (2.71) is valid also for the electron density per unit energy:

$$2\pi n(\boldsymbol{r};E) = G^<(\boldsymbol{r},\boldsymbol{r};E) \tag{2.72}$$

In general, lesser and greater Green's functions can be derived from the retarded and advanced ones via Keldysh equation:

$$G^{\lessgtr}(\boldsymbol{r},\boldsymbol{r}';E) = \int d\boldsymbol{r}_1 \int d\boldsymbol{r}_2\; G^R(\boldsymbol{r},\boldsymbol{r}_1;E)\Sigma^{\lessgtr}(\boldsymbol{r}_1,\boldsymbol{r}_2;E)G^A(\boldsymbol{r}_2,\boldsymbol{r}';E) \tag{2.73}$$

However, at thermal equilibrium, they are related by the simpler *fluctuation-dissipation theorem* [14], [16]:

$$G^<(\boldsymbol{r},\boldsymbol{r}';E) = if\,(E-\mu)\,\mathcal{A}(\boldsymbol{r},\boldsymbol{r}';E) \tag{2.74}$$

$$G^>(\boldsymbol{r},\boldsymbol{r}';E) = i\left[f\,(E-\mu) - 1\right]\mathcal{A}(\boldsymbol{r},\boldsymbol{r}';E) \tag{2.75}$$

in which $f(E-\mu)$ is the Fermi-Dirac distribution of electrons, and $\mathcal{A}$ is the spectral function defined in (2.49). Similarly, the lesser and greater self-energies can be expresses as:

$$\Sigma^{<}(\boldsymbol{r},\boldsymbol{r}';E) = if(E-\mu)\Gamma(\boldsymbol{r},\boldsymbol{r}';E) \tag{2.76}$$

$$\Sigma^{>}(\boldsymbol{r},\boldsymbol{r}';E) = i\left[f(E-\mu)-1\right]\Gamma(\boldsymbol{r},\boldsymbol{r}';E) \tag{2.77}$$

in which Γ is the broadening function, as defined in equation (2.41).

2.2.9 Current density operator

Having defined the four Green's functions with their corresponding self-energies, it is now possible to derive the formula for the total current flowing through the system when a bias voltage is applied, and verify it is indeed the same as the Landauer-Büttiker formula (1.23), with transmission probability given by (2.40); but first, the current density operator needs to be defined.

The general expression for calculating the current density from the wavefunction is given by [17]:

$$\boldsymbol{J} = \frac{e}{2m}\left(\Psi\left[(\boldsymbol{p}-e\boldsymbol{A})\,\Psi\right]^{*} + \Psi^{*}\left[(\boldsymbol{p}-e\boldsymbol{A})\,\Psi\right]\right) \tag{2.78}$$

in which $\boldsymbol{p} = -i\hbar\nabla$ is the momentum operator, and $\boldsymbol{A}$ a generic vector potential. The wavefunction is in general composed of both an incident and a reflected component, respectively:

$$\Psi_i = \frac{1}{\sqrt{L_x}}\chi^{+}(y)e^{ik^{+}x} \tag{2.79}$$

$$\Psi_r = \frac{1}{\sqrt{L_x}}r\chi^{-}(y)e^{-ik^{-}x} \tag{2.80}$$

Equation (2.78) can be also written as:

$$\boldsymbol{J}(\boldsymbol{r};E) = \frac{e}{2m}\left[(\boldsymbol{p}-\boldsymbol{p}')\,\Psi(\boldsymbol{r})\Psi^{*}(\boldsymbol{r}')\right]_{\boldsymbol{r}'=\boldsymbol{r}} - \frac{e^2}{m}\boldsymbol{A}(\boldsymbol{r})\left[\Psi(\boldsymbol{r})\Psi^{*}(\boldsymbol{r}')\right]_{\boldsymbol{r}'=\boldsymbol{r}} \tag{2.81}$$

in which momentum operators $\boldsymbol{p}$ and $\boldsymbol{p}'$ operate on $\boldsymbol{r}$ and $\boldsymbol{r}'$, respectively. Writing the electron density in terms of the wavefunction as:

$$n(\boldsymbol{r};E) = \Psi(\boldsymbol{r})\Psi^{*}(\boldsymbol{r}) = \frac{G^{<}(\boldsymbol{r},\boldsymbol{r};E)}{2\pi} \tag{2.82}$$

as in (2.72), is is possible to express equation (2.81) in terms of the lesser Green's function:

$$2\pi\boldsymbol{J}(\boldsymbol{r};E) = \left[-\frac{ie\hbar}{2m}\left(\nabla-\nabla'\right)G^{<}(\boldsymbol{r},\boldsymbol{r}';E) - \frac{e^2}{m}\boldsymbol{A}(\boldsymbol{r})G^{<}(\boldsymbol{r},\boldsymbol{r}';E)\right]_{\boldsymbol{r}'=\boldsymbol{r}} \tag{2.83}$$

and the terminal current per unit energy can be obtained integrating (2.83) over the cross section of the corresponding contact:

$$i_p(E) = \int_{S_p}\boldsymbol{J}(\boldsymbol{r};E)\cdot d\boldsymbol{S} \tag{2.84}$$

in which S_p is the surface separating the conductor from contact p.

In addition, equation (2.83) can be integrated over the energy variable to obtain the current flow pattern across the device:

$$\boldsymbol{J}(\boldsymbol{r}) = 2\times\int\boldsymbol{J}(\boldsymbol{r};E)\;dE \tag{2.85}$$

in which a factor two is required to account for the spin multiplicity.

This approach is better suited if the interest is on the current flow pattern inside the conductor; however, the terminal current can also be derived directly without calculating the current density as in [4],[12], [18], by defining a *current operator* whose diagonal elements are equal to the divergence of the current density operator defined in this section.

2.2.10 Current operator and relation to the Landauer-Büttiker formula

Knowing that, in general, given the current density $\boldsymbol{J}(\boldsymbol{r};E)$, the total current can be obtained from its divergence:

$$I(E) = \nabla \cdot \boldsymbol{J}(\boldsymbol{r};E) \tag{2.86}$$

If the focus is on the total current flowing through the conductor, it is convenient to define a *current operator* in such a way that its diagonal elements satisfy (2.86) rather than working with the current density operator.

To derive an explicit expression for the divergence of the current density operator some observations have to be made. Starting from the matrix formulation (2.37), and expressing it in position representation, an equation equivalent to (2.26) is obtained:

$$[E - H]\, G^R(\boldsymbol{r},\boldsymbol{r}') - \int \Sigma^R(\boldsymbol{r},\boldsymbol{r}_1) G^R(\boldsymbol{r}_1,\boldsymbol{r}')\; d\boldsymbol{r}_1 = \delta(\boldsymbol{r}-\boldsymbol{r}') \tag{2.87}$$

As stated when introducing the retarded Green's function, $G^R(\boldsymbol{r},\boldsymbol{r}')$ can be visualized as the wavefunction evaluated at point $\boldsymbol{r}$ due to an excitation at point $\boldsymbol{r}'$; leaving the excitation term on the right-hand side of (2.87) out of the equation a Schrödinger-like equation is obtained, which describes the dynamics of an electron inside the system:

$$H\Psi(\boldsymbol{r}) + \int \Sigma^R(\boldsymbol{r},\boldsymbol{r}_1)\Psi(\boldsymbol{r}_1)\; d\boldsymbol{r}_1 = E\Psi(\boldsymbol{r}) \tag{2.88}$$

In the general current density formulation (2.78), the momentum operator $\boldsymbol{p} = -i\hbar\nabla$ is equal to zero as long as the wavefunction Ψ obeys the time-independent Schrödinger equation; however, if the wavefunction obeys the modified Schrödinger's equation (2.88) then the divergence of the current density operator is non-zero, and can be expressed in terms of the wavefunction as:

$$i\hbar\nabla\cdot\boldsymbol{J} = e\left(\left[H\Psi\right]^*\Psi - \Psi^*\left[H\Psi\right]\right) \tag{2.89}$$

and rewritten in an equivalent form to introduce the lesser Green's function instead of the wavefunction:

$$i\hbar\nabla\cdot\boldsymbol{J}(\boldsymbol{r};E) = e\left(\left[H(\boldsymbol{r}) - H^*(\boldsymbol{r}')\right]\Psi(\boldsymbol{r})\Psi^*(\boldsymbol{r}')\right)_{\boldsymbol{r}'=\boldsymbol{r}} \tag{2.90}$$

Using again the identity (2.82), equation (2.90) becomes:

$$i2\pi\hbar\nabla\cdot\boldsymbol{J}(\boldsymbol{r};E) = -e\left(\left[H(\boldsymbol{r}) - H^*(\boldsymbol{r}')\right]G^<(\boldsymbol{r},\boldsymbol{r}')\right)_{\boldsymbol{r}'=\boldsymbol{r}} \tag{2.91}$$

Then, the current operator can be defined an in [4], [12] and [18]:

$$I_{op}(\boldsymbol{r},\boldsymbol{r}';E) = \frac{e}{h}\left[H(\boldsymbol{r})G^<(\boldsymbol{r},\boldsymbol{r}';E) - G^<(\boldsymbol{r}',\boldsymbol{r};E)H(\boldsymbol{r}')\right] \tag{2.92}$$

whose diagonal elements satisfy (2.86). The total current is evaluated over a surface S enclosing the system:

$$\begin{aligned}
I(E) =& \int dE \oint_S d\boldsymbol{S}\cdot\boldsymbol{J}(\boldsymbol{r};E) = \\
=& \int dE \int d\boldsymbol{r}\; I_{op}(\boldsymbol{r},\boldsymbol{r}';E) = \\
=& \frac{e}{h}\int dE \int d\boldsymbol{r} \sum_{ij}\left[H(\boldsymbol{r})G^<_{ij}(E)\phi_i(\boldsymbol{r})\phi_j^*(\boldsymbol{r}) - G^<_{ij}(E)\phi(\boldsymbol{r})\phi^*(\boldsymbol{r})H(\boldsymbol{r})\right] = \\
=& \frac{e}{h}\int dE \sum_{ij}\left[H_{ij}G^<_{ij}(E) - G^<_{ij}(E)H_{ij}\right] \\
=& \frac{e}{h}\int dE\; Tr\left[HG^<(E) - G^<(E)H\right]
\end{aligned} \tag{2.93}$$

In equation (2.93), the flux integral across the closed surface S has been turned into a volume integral using the divergence theorem together with equation (2.86), and the integral over real space coordinates has been transformed into the matrix equation involving the Hamiltonian and lesser Green's function matrices, such as in [12] and [19].

Finally, taking into account only the coherent component of the current, it is possible to make use of equalities granted by the fluctuation-dissipation theorem (2.74)-(2.77) and the Keldysh equation (2.73), that in matrix form writes:

$$G^{\lessgtr} = G^R \Sigma^{\lessgtr} G^A \tag{2.94}$$

and makes it is possible to obtain:

$$I(E) = 2 \times \frac{e}{h} \int dE \; Tr \left\{ \Gamma_1 \left[f(E-\mu_1)\mathcal{A}(E) + iG^<(E) \right] \right\} \tag{2.95}$$

in which $\mathcal{A}(E)$ is the spectral function matrix defined in (2.49), and a factor two is added to account for the spin multiplicity. Finally, equation (2.95) can be rewritten as:

$$\begin{aligned} I(E) =& \frac{2e}{h} \int Tr \left[\Gamma_1 G^R \Gamma_2 G^A \right] \left[f(E-\mu_1) - f(E-\mu_2) \right] dE = \\ =& \frac{2e}{h} \int T(E) \left[f(E-\mu_1) - f(E-\mu_2) \right] dE \end{aligned} \tag{2.96}$$

which is the Landauer-Büttiker formula (1.23), with transmission function $T(E)$ given by (2.40), and broadening functions $\Gamma_{(1,2)}$ defined as in (2.41).

2.2.11 Summary of the solution procedure

The NEGF algorithm is much more computationally expensive than the FEM algorithm presented in section 2.1; therefore, the adopted resolution can really affect the speed of simulation and, in some cases, using a more refined mesh was not the correct choice when trying to improve the results quality.

First, discretization mesh for the real space variable x and the energy variable have to be defined before implementing the FEM algorithm of section 2.1.

Since in the implemented model the potential energy profile $U(x)$ that appears in the Schrödinger equation presents abrupt discontinuities and is piece-wise constant, such as in figures 1.1 or 1.2, the x-axis mesh does not need to be particularly refined. A value of 53 mesh points was used in single-barrier simulations and a value of 105 was used in most of double-barrier simulations, with some adjustments in some problematic cases. These values were found after several attempts at reducing the complexity of algorithm, in an attempt to make the code as fast as possible at performing the required calculations.

On the other hand, the energy axis needs to be sufficiently refined to produce a reliable transmission probability $T(E)$, to be integrated according to equation (2.96) in order to derive the total current. The required number of energy mesh points proved to be extremely high with a lot of variability, depending on the complexity of the system to simulate. In particular, double-barrier systems with a lot of confined energy levels required an order of magnitude of 10^5 energy mesh points or higher because the lower-energy levels contributed to $T(E)$ with extremely narrow transmission peaks that were difficult to resolve. In such cases, the higher the number of confined levels, the more the system resembles an ideal one with infinite barriers, in which transmission is only allowed for those specific energy values corresponding to the position of confined levels between the barriers.

After defining the x and energy axes, the bias voltage can be initialized such as in section 2.1: the voltage drop is distributed linearly across the system, and contacts with the reservoirs are assumed to be ideal; hence, the voltage profile remains flat at the beginning and at the end of the simulation domain. The bias voltage

enters Schrödinger's equation together with the potential energy profile, progressively "tilting" the system's equilibrium potential energy in one direction as the bias increases.

Having defined these quantities, the loop over the bias voltage can start. At each iteration, the algorithm adds the equilibrium potential energy to the bias voltage profile and derives the FEM stiffness and mass matrices for Schrödinger's equation, H and M, respectively, as in section 2.1; the only difference is that this time boundary conditions are not introduced yet.

Matrices H and M are used to derive the retarded Green's function according to Dyson's equation (2.37):

$$G^R = \left[EM - H - \Sigma^R\right]^{-1} \tag{2.97}$$

in which Σ^R is the total self-energy due to the leads in matrix form and, as in (2.38) it only contains the effects of the two contacts as first and last elements, which are the same as the boundary conditions of the FEM model.

Finally, it is possible to obtain the advanced Green's function as the Hermitian conjugate of the retarded Green's function with (2.33), and the broadening functions with (2.41):

$$\left[G^A\right] = \left[G^R\right]^\dagger \tag{2.98}$$

$$\left[\Sigma^A\right] = \left[\Sigma^R\right]^\dagger \tag{2.99}$$

$$\Gamma_{(1,2)} = i\left[\Sigma^R_{(1,2)} - \Sigma^A_{(1,2)}\right] \tag{2.100}$$

Matrices (2.97) and (2.98) are then used to derive the spectral function $\mathcal{A}(E)$ according to (2.49) and, dividing it by 2π, the real-space representation of the local density of states:

$$[\mathcal{A}(E)] = i\left(\left[G^R(E)\right] - \left[G^A(E)\right]\right) \tag{2.101}$$

while matrices (2.98) and (2.100) are used to calculate the transmission probability $T(E)$ as in (2.40):

$$T(E) = Tr\left[\Gamma_1 G^R \Gamma_2 G^A\right] \tag{2.102}$$

Finally, the current is obtained via Landauer-Büttiker formula (2.102), in which $\mu_1 - \mu_2 = e \cdot V$, and V is the applied bias voltage:

$$I(E) = \frac{2e}{h}\int T(E)\left[f(E-\mu_1) - f(E-\mu_2)\right] dE \tag{2.103}$$

Lesser and greater Green's functions, together with their corresponding self-energies, are required to prove some implemented equations, namely (2.102) and (2.103); however, they do not appear directly in the final expressions of those equations, so they do not appear in the solving algorithm either. A schematic pseudocode of the solving algorithm is shown in the next section.

2.2.12 Pseudocode of the NEGF solving algorithm

Algorithm 2: Solution procedure by NEGF

Data: x, *Energy*, *Bias*, U_{eq}
Result: Current I, Local Density of States $LDOS$
Initialization;
for *Bias* **do**
  $U = U_{eq} + q \cdot Bias$;
  $\mu_1 = E_F + q \cdot Bias/2$;
  $\mu_2 = E_F - q \cdot Bias/2$;
  for x **do**
    Define FEM matrices;
    H = stiffness matrix;
    M = mass matrix;
  end
  for *Energy* **do**
    $A = Energy \cdot M - H$;
    $k_{\text{Left}} = \sqrt{\dfrac{2m(Energy - U(1))}{\hbar^2}}$;
    $k_{\text{Right}} = \sqrt{\dfrac{2m(Energy - U(end))}{\hbar^2}}$;
    $\Sigma_1(1,1)$ = interaction with the left contact (boundary condition);
    $\Sigma_2(end, end)$ = interaction with the right contact (boundary condition);
    $\Sigma = \Sigma_1 + \Sigma_2$;
    $G^R = \text{inv}(A - \Sigma)$;
    $G^A = \left(G^R\right)^\dagger$;
    $\Gamma_1 = i\left(\Sigma_1 - \Sigma_1^\dagger\right)$;
    $\Gamma_2 = i\left(\Sigma_2 - \Sigma_2^\dagger\right)$;
    $\mathcal{A} = i\left(G^R - G^A\right)$;
    $LDOS(Energy) = \dfrac{diag(\mathcal{A})}{2\pi}$;
    $T(Energy) = \text{Re}\left[\text{Tr}\left(\Gamma_1 G^R \Gamma_2 G^A\right)\right]$;
  end
  $I(Bias) = \dfrac{2e}{h} \int T(Energy)\left[f(Energy - \mu_1) - f(Energy - \mu_2)\right] dE$;
end

2.2.13 Model testing and validation

Before trying to simulate resonant tunneling devices in an attempt to observe the Coulomb blockade effects on the total current, the model was tested with simple, known systems in order to prove its validity by reproducing expected results such as an Ohmic current behaviour with a flat $U(x)$ emulating a ballistic device, and an exponential current trend in case of a single-barrier tunneling device. All simulations have been performed at ambient temperature: $T = 300\ K$

The ballistic device is shown in figure 2.6. The potential energy profile at equilibrium is represented by the black line labelled $U(x)$, and the blue line is the equilibrium chemical potential which is unique across the system when no bias voltage is applied.

The progressively increasing voltage drop between the contacts is implemented exactly as in the FEM model, and an example is shown in figure 2.4.

The red map represents the local density of states on a logarithmic scale, from here on shortened to LDOS, evaluated from the spectral function (2.101); the density is nearly uniform for all energies and equally distributed along the x-axis, which is expected from a ballistic device in which electrons are free to drift from one contact to the other without encountering any obstacles or interactions.

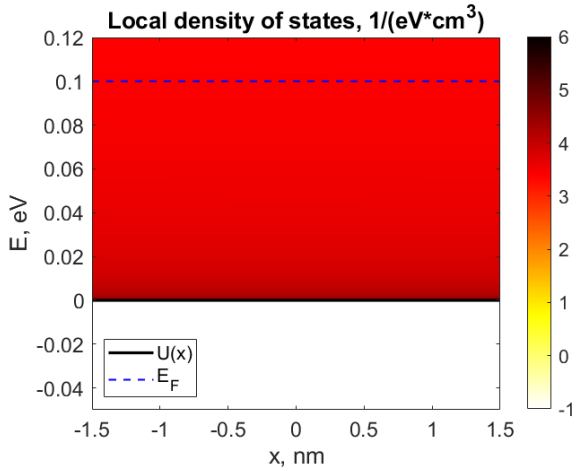

Figure 2.6: Ballistic device, equilibrium LDOS.

Figure 2.7 shows on the left the transmission probability (2.102) as a function of the electron energy in the same equilibrium condition as in figure 2.6 and, as it is clearly visible from the plot, it reflects the previous statement about incoming electrons being free to drift across the ballistic device, since they are transmitted with probability equal to one independently of their energy.

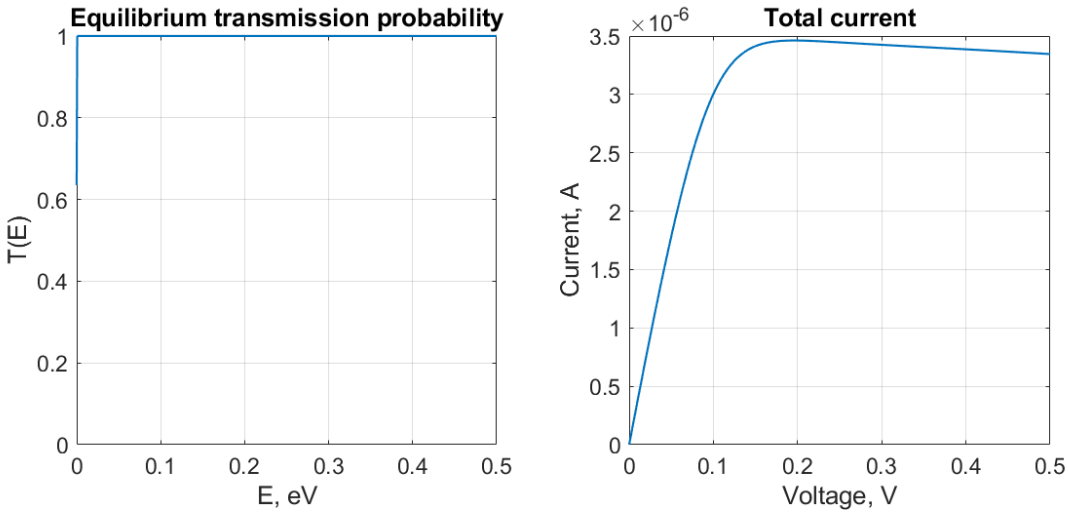

Figure 2.7: Ballistic device, equilibrium transmission probability and total current.

On the right of figure 2.7, as well as in figure 2.8, is the total current plotted on a linear and logarithmic axis, respectively. Both plots show a current which is a linear function of the bias voltage as long as $e \cdot V \lessapprox E_F = 0.1eV$; as the bias voltage increases further, the device saturates and the current starts to slowly decrease.

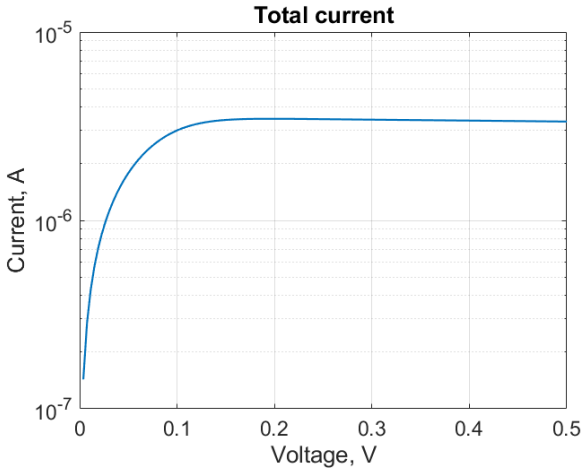

Figure 2.8: Ballistic device, total current.

The slope of the linear portion of the total current on the right in figure 2.7 is directly related to the conductance of the contacts, since the device is ballistic [4].

The quantum of conductance is defined as:

$$G_0 = \frac{2e^2}{h} \approx 77.481\ \mu S \tag{2.104}$$

and in terms of electrical resistance it becomes:

$$R_0 = G_0^{-1} = \frac{h}{2e^2} \approx 12.906\ k\Omega \tag{2.105}$$

The conductance of the simulated system has been evaluated through the slope obtained interpolating the linear portion of the total current; the derived value and its corresponding electrical resistance are:

$$G \approx 36.262\ \mu S \tag{2.106}$$

$$R \approx 27.577\ k\Omega \tag{2.107}$$

The extrapolated G value can be lower than the quantum of conductance G_0 due to there being a left-hand and right-hand contact which are connected in series through the ballistic device which is the system under analysis. This is confirmed by both simulations and experiments, such as in [20].

The ratio $R/R_0 \approx 2.1$; thus, the two contacts introduce an overall electrical resistance which is nearly double the inverse of the quantum of conductance; the G and R values are temperature-dependent and, as the temperature decreases, they modify so that the ratio $R/R_0 \to 2$

The test single-barrier tunneling device is the same one employed in section 2.1 for the FEM implementation and shown for reference in figure 2.2.

A comparison has been made among the equilibrium transmission probabilities derived from the analytic expression (1.6), the FEM solution, and the NEGF solution; the result is reported in figure 2.9. Analytic and FEM solutions have already been compared in figure 2.2 and shown to be exactly coincident with each other; the same two curves have been plotted in 2.9, together with the transmission probability derived with the NEGF approach according to equation (2.102), and all three solutions are in nearly perfect agreement with one another. The transmission probability rises exponentially as long as the electron energy is inferior to the barrier's; while it stabilizes near unity for electron energies which are superior to the barrier's.

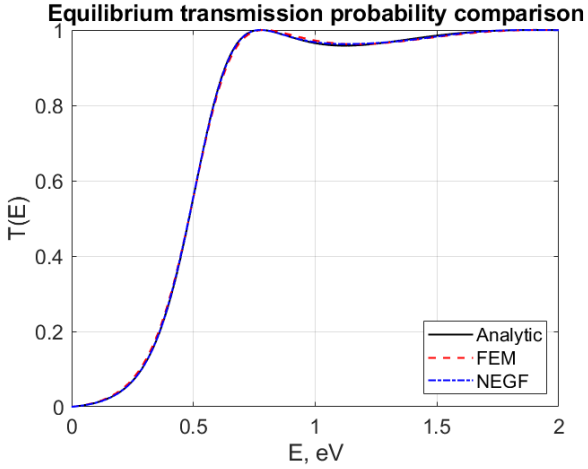

Figure 2.9: Single-barrier tunneling device, equilibrium transmission probability comparison.

Differences between the FEM and NEGF implementations arise again when a bias voltage is applied to the system: the FEM transmission probability, such as the one shown for the double-barrier system in figure 2.5, evolves with bias in a physically incorrect way, without going to zero in the low-energy range when the increasing bias voltage rises the potential energy profile near the left-hand contact.

This kind of incorrect behaviour is not present in the NEGF transmission probability, which evolves with bias in a physically meaningful way. This is reflected in the total current derived from the NEGF transmission probability, which is reported in figure 2.10 for an equilibrium chemical potential equal to 0.1 eV.

The same current is shown in both linear and logarithmic axis in figures 2.10a and 2.10b, respectively. Both plots clearly show the exponential current trend which is characteristic of a single-barrier tunneling

device; in particular, the logarithmic plot in figure 2.10b presents a linear trend, with a well-defined slope which again proves the exponential nature of the total current.

At first sight, the current in the low-bias region presents an anomalous behaviour for $V < 0.1\ V$, being more similar to an Ohmic I-V characteristics rather than an exponential function; however, also textbook examples, such as those found in [11], show this kind of trend in the low-bias region.

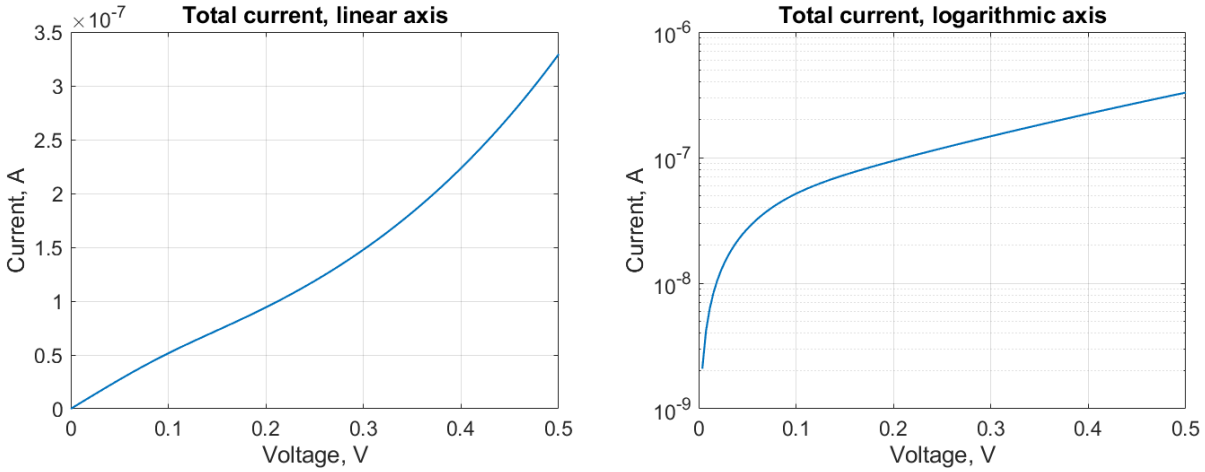

(a) Linear axis.

(b) Logarithmic axis.

Figure 2.10: Single-barrier tunneling device total current.

Finally, the same double-barrier resonant tunneling system used as a test in the FEM model and presented in section 2.1, figure 2.3 has been simulated with the NEGF algorithm. The system is reported again in figure 2.11, together with the LDOS derived from the NEGF matrices according to (2.101) exactly as in the previous test device.

Again, the LDOS has been plotted on a logarithmic colour scale so that the reference colour scale near the plot refers to the orders of magnitude of the local density of states, instead of its exact values; this choice has been made in order to better enhance the colour contrast and highlight the presence of high-density regions within the barriers that otherwise would have been barely visible on a linear scale. This functional choice has become the new standard in this work for the visualization of double-barrier systems' LDOS due to it being a practical solution to clearly portrait the confined energy levels.

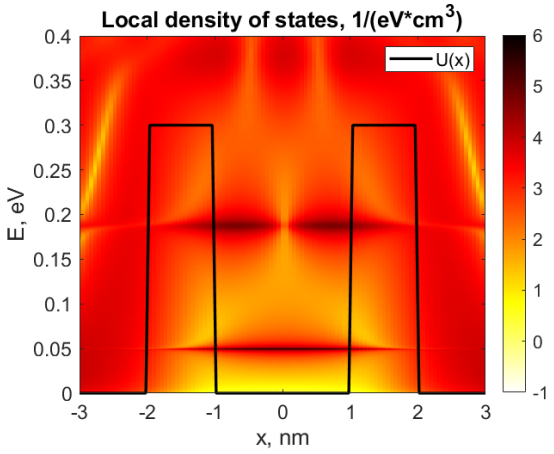

Figure 2.11: Double-barrier resonant tunneling device, equilibrium LDOS.

The LDOS in figure 2.11 serves also the purpose of verifying the numbering of confined energy levels since high-density regions reflect the number of nodes the confined wavefunction presents. In this case, the lowest confined state does not present any node just as its corresponding wavefunction; while the second confined state presents one node around $x = 0$ in figure 2.11 similarly to the corresponding wavefunction.

An outline of a third energy level is hinted at by the three higher-density regions around 0.4 eV, slightly above the barriers; however, that energy region sits outside the barriers and it only resemble an energy level. This is also confirmed by the transmission probability in figure 2.12 which presents two narrow tunneling peaks for energies within the barriers and a wider, incomplete peak around $E = 0.4$ eV.

Figure 2.12 shows a comparison of the equilibrium tunneling probability derived according to the analytic expression (1.12) together with the FEM and NEGF solutions. At equilibrium, FEM and NEGF results are nearly indistinguishable from each other, and they are in overall good agreement with the analytic formula; this is particularly true in the confinement region, for energies inferior to 0.3 eV of the barriers, which is the most relevant portion. Instead, as already observed when dealing with the FEM solution, at higher energies both of them differentiate slightly from the analytic expression. However, that should not be a cause of concern since, in such devices, conduction is usually made to occur due to confined levels, in order to better visualize the current steps and oscillations characteristic of the coulomb blockade phenomenon.

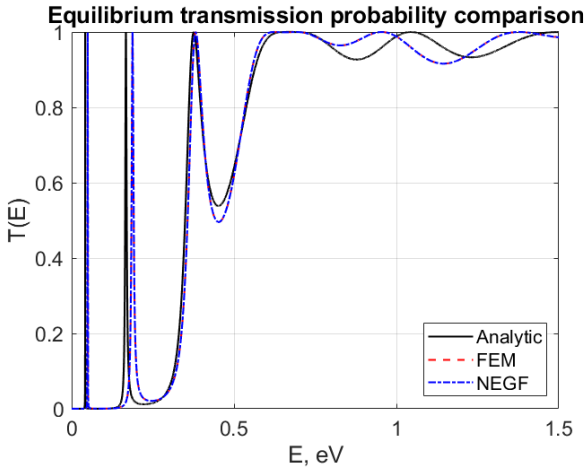

Figure 2.12: Double-barrier resonant tunneling device, equilibrium transmission probability comparison.

Figure 2.13 shows the evolution of the NEGF model transmission probability after a few initial voltage steps; similarly to how figure 2.5 does for the FEM model.

The NEGF solution is more consistent than the FEM one regarding how the transmission probability should intuitively change with an applied bias voltage: as the energy at the left-hand contact progressively rises, transmission through the lower-energy level becomes gradually less likely, until it is no longer possible due to there being no more electrons with such energies incoming from the contact.

In addition, the NEGF transmission probability does not suffer from the incorrect trend the FEM one assumes for bias voltages higher than approximately 0.1 V, in which peaks start to reach above unity. Instead, the NEGF transmission probability always remains in the range $[0, 1]$ for all energies, independently of the applied bias voltage.

The resulting current for the double-barrier resonant tunneling device, obtained integrating the NEGF tunneling probability (2.101) according to (2.102), is shown in figure 2.14.

The current in figure 2.14a presents two clear oscillations which are one of the signature characteristics of the Coulomb blockade phenomenon, together with the staircase current behaviour. Each oscillation in the current can be related to one of the two confined levels, since the information contained in the transmission

probability states that when incoming electrons have a kinetic energy sufficiently near to the position of a confined level they are transmitted through the system with probability equal to unity. In this situation, the current reaches a maximum.

At the same time, the overall trend of the current is still exponential with the bias voltage, and is shown in figure 2.14b. The limited bias range does not make it very clear; however, this is evident from figure 2.15 which is a simulation of the same system under a higher bias voltage.

The distance between barriers is equal to 2 nm as shown in figure 2.11 and, as stated in [3], a nanoparticle of this size presents negative differential resistance dV/dI within its I-V characteristics. Such regions are present in this case as well, corresponding to a decreasing current right after a peak is reached.

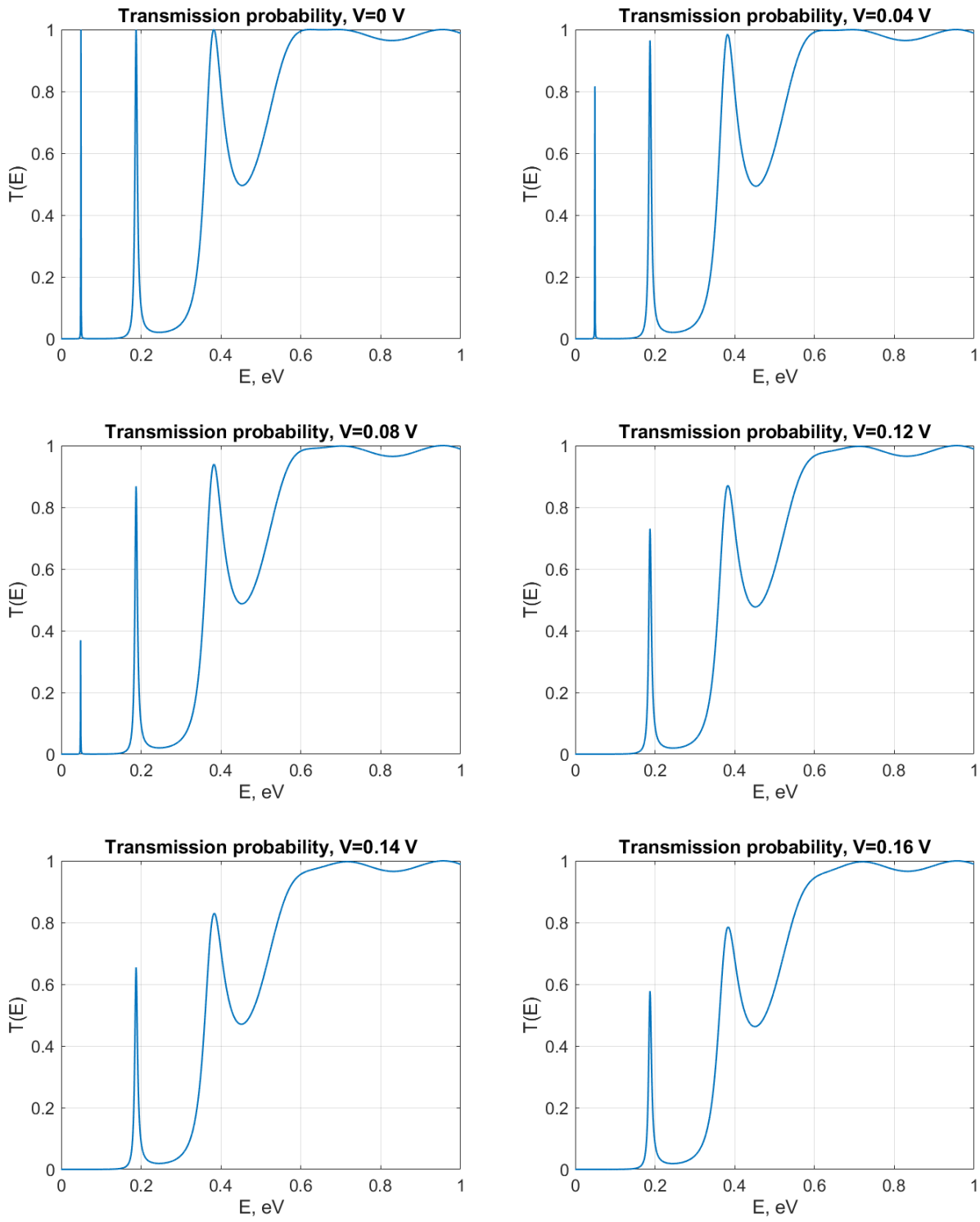

Figure 2.13: NEGF transmission probability, evolution with increasing bias.

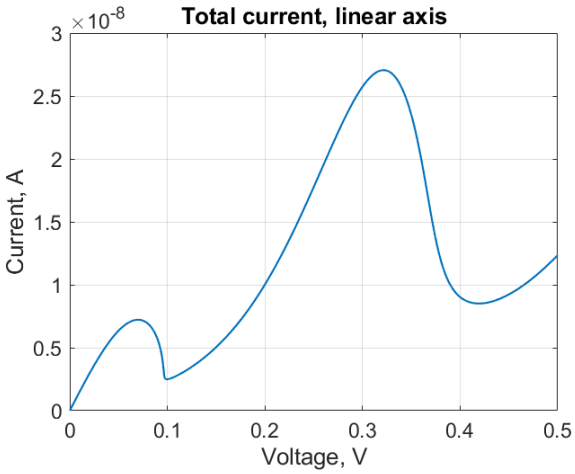

(a) Linear axis.

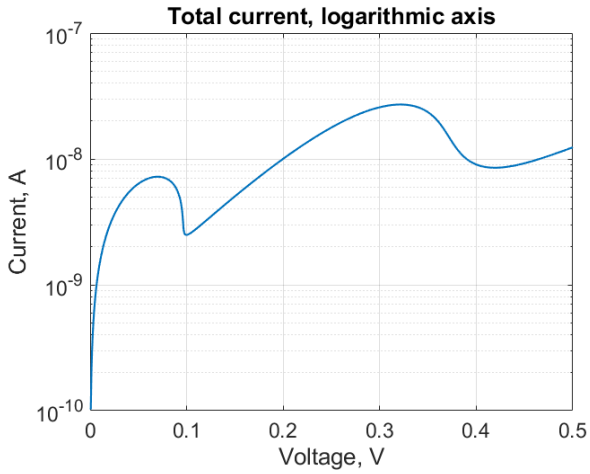

(b) Logarithmic axis.

Figure 2.14: Double-barrier resonant tunneling device, total current.

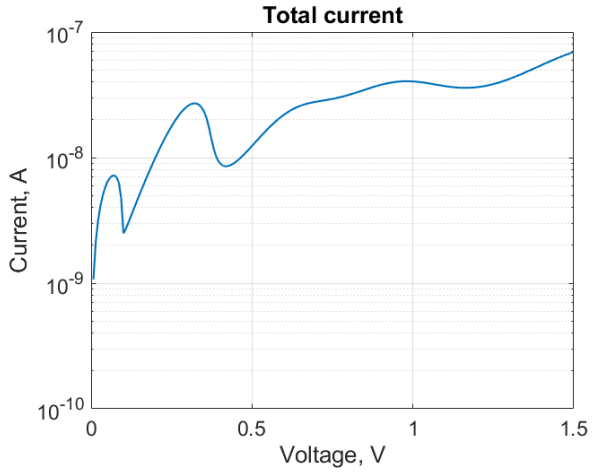

Figure 2.15: Higher bias total current, logarithmic axis.

Chapter 3

The influence of geometrical parameters on the Coulomb blockade

As a first analysis, the effect of varying geometrical parameters, such as the thickness of tunneling barriers, energy discontinuity and distance between barriers, has been studied on progressively more complex systems with an increasing amount of confined energy levels within the barriers, in order to observe their effects on the total current.

The bias voltage has been applied in a similar manner as in figure 2.4. This choice allows to selectively include within the bias window one energy level at a time, starting from the lowest-energy one, while at the same time all the others are not able to contribute to conduction.

With this approach, the effect of each energy level on the total current can be separated from the others.

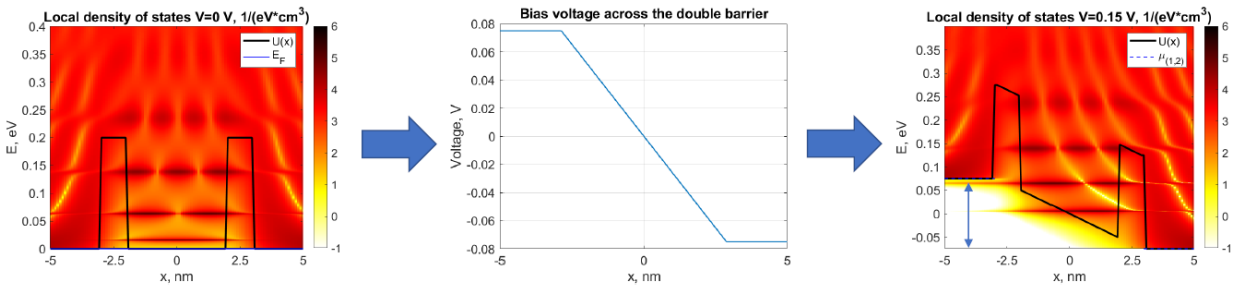

Figure 3.1: Graphical representation of a bias voltage such that only one energy level is conducting at a time.

As shown in figure 3.1, applying a similar bias voltage, electronic states are allowed to exist only for energies higher than $U(x)$ and the local density of states rapidly decays to zero as $E < U(x)$, represented by the white colour in the local density of states map. This means that there cannot be electrons with such energies since there are no states to be occupied by them; this is unrealistic for a metal contact and is the approach rather used for semiconductor heterostructures in which $U(x)$ would represent the conduction band edge.

Nonetheless, this proves to be useful when trying to highlight the effect of each individual energy level on the total current.

As a reminder, all density of states are plotted on a logarithmic axis; therefore, the colour scale denotes its order of magnitude rather than its actual value. For a better representation, values whose order of magnitude is 6 or higher have been assigned the black colour, while all the values whose order of magnitude is -1 or lower are represented in white.

3.1 Effect of the barriers thickness

The effect of varying barriers thickness has been observed by fixing the tunneling barriers and the distance between them. This parameter is associated with the thickness of the shell enclosing the nanoparticle metallic core; it is usually constituted by either a metal oxide, such as in [21], or an organic compound such as a thiol, as in [22]. [23] and [24]. In general, the purpose of the shell is to stabilize the core during the nanoparticle synthesis, and limit its growth in size.

The barriers have been fixed to an energy value equal to 0.2 eV, and the distance between them is 2 nm. These parameters allow the presence of two confined energy levels in all analysed cases. Then, the system has been simulated for different thicknesses of barriers.

Even slight variations in the barriers thickness produce highly noticeable changes in the current intensity, which is expected since the tunneling current is a decreasing exponential function of the barriers thickness, as stated by equation (1.7) and proven in appendix A by equation (A.16).

Figure 3.2 presents the simulated system with thickness of barriers equal to 1 nm, here used as a graphical example, together with different transmission functions derived for three analysed systems with different barriers thickness. It is possible to notice that, as the barriers become thicker, tunneling peaks become narrower; this means confinement becomes stronger and more similar to an ideal scenario in which energy levels are defined by one exact energy value. At the same time, the tunneling probability of electrons decreases significantly for energy values that lie in the gap between two consecutive energy levels.

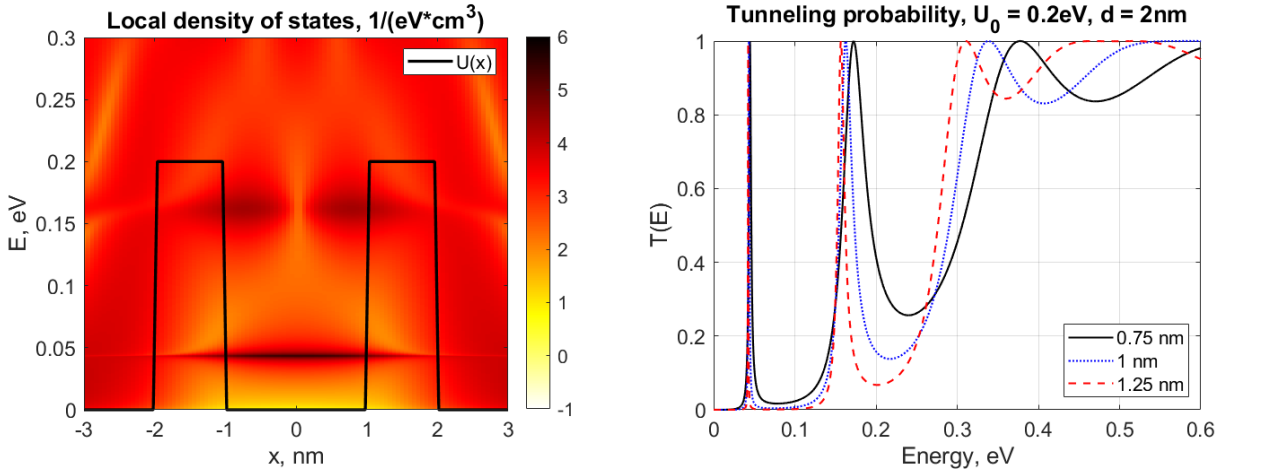

(a) Double-barrier system with $t = 1$ nm.

(b) Transmission function for different barriers thicknesses.

Figure 3.2: Reference simulated system for barriers thickness comparison and transmission functions.

The total currents are reported in figure 3.3, both on a linear and a logarithmic axis. Two resonances, corresponding to the confined energy levels, are observable in the low-bias region; then, the current profile stabilizes and starts increasing in every system.

Although the barriers thickness has a significant influence on the average current, it does not affect the shape of resonant oscillations. The logarithmic plot in figure 3.3b shows that the amplitude of the resonant oscillations, relatively to the average current value, is not much affected by different values of thickness: even if, on a linear axis, the oscillations seems to dampen as the thickness of barriers increases, as shown in figure 3.3a, they are indeed scaled proportionally to their average current curve.

The overall current trend is exponential for thickness values around 1 nm; however, when increasing it to around 2 nm and above, tunneling becomes negligible, and the resulting current becomes more and more linear with the voltage, which is characteristic of an electrical resistance. This means that electrons are not

able to drift across the system by tunneling across the barriers, but they need to have sufficient energy to overcome them.

Nonetheless, for thickness values which are significant as far as tunneling is concerned, the currents have always been found to be similar to figure 3.3; therefore, since the amplitude of resonances is scaled accordingly to the average current profile, the thickness is not one of the main factors in determining whether the total current presents resonant oscillations rather than a staircase behaviour.

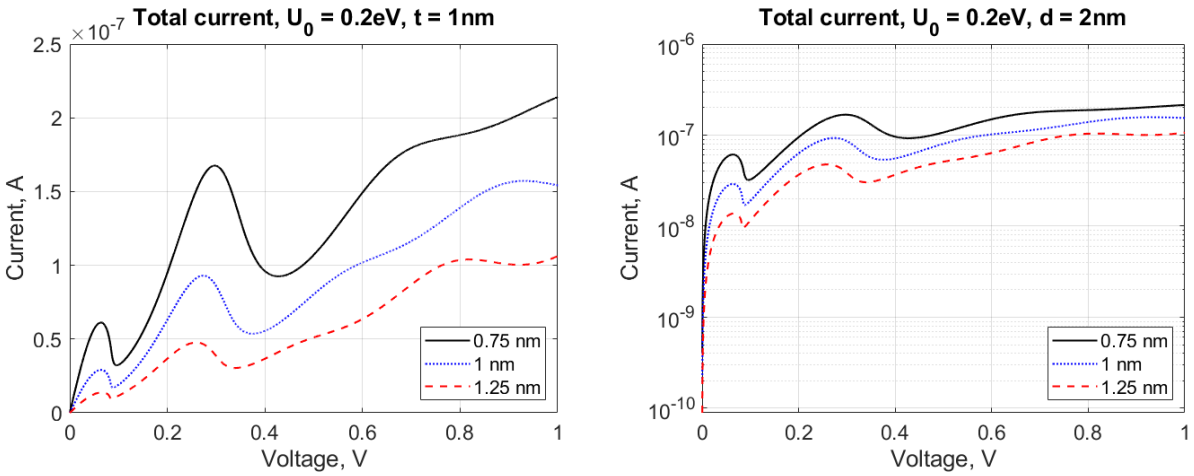

(a) Linear current axis.

(b) Logarithmic current axis.

Figure 3.3: Total current comparison for different barriers thicknesses.

3.2 Effect of the "barriers height": the U_0 value

Another parameter that can be varied is the "height" of tunneling barriers, i.e the energy discontinuity between the reference zero energy, which corresponds to the equilibrium chemical potential of the contacts, and the edge of the quantum well region encompassed by the barriers.

This parameters is the value labelled as U_0 in equation (A.1), and it directly affects the number of confined energy levels, thus the number of oscillations and steps in the I-V characteristics.

In this analysis, the thickness of barriers has been fixed to 1 nm, while the particle dimension to 2 nm, which are the parameters of the system in figure 3.2a; then, the value U_0 has been progressively increased.

Similarly to the analysis performed in section 3.1 for different barriers thicknesses, initially there are two confined energy levels; however, in this case, increasing U_0 a third peak of the transmission function in figure 3.4a assumes more and more the features characteristic of a confined energy level: it becomes progressively narrower and the tunneling probability for nearby energies tends to zero. However, an actual third confined energy level is observed for the first time with $U_0 = 0.45\ eV$, as in figure 3.4b.

For the purpose of controlling the energy levels positions, changing U_0 is more effective than working on the barriers thickness. Figure 3.4a shows that as U_0 increases, the levels positions also shift to slightly higher energies, and the shift becomes more visible as the energy level is closer to the barriers edge. However, the lower-energy level is barely affected by the increase of U_0 and its shift is minimal; thus, it is reasonable to assume that in a more complex system, with many confined energy levels, only those that are closer to the barriers edge will be affected by a change in U_0.

This means that U_0 is not the crucial parameter in determining the energy levels positions.

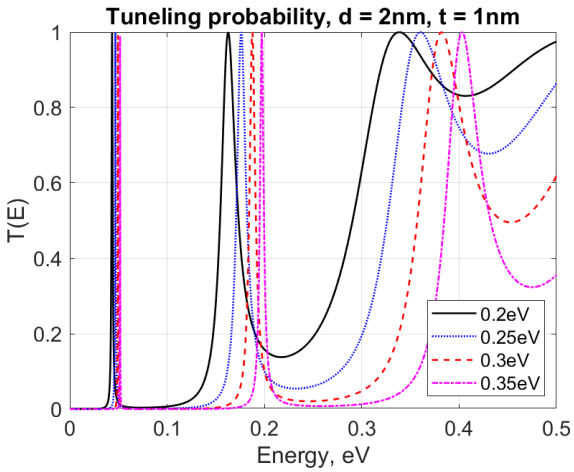

(a) Transmission function for different U_0 values.

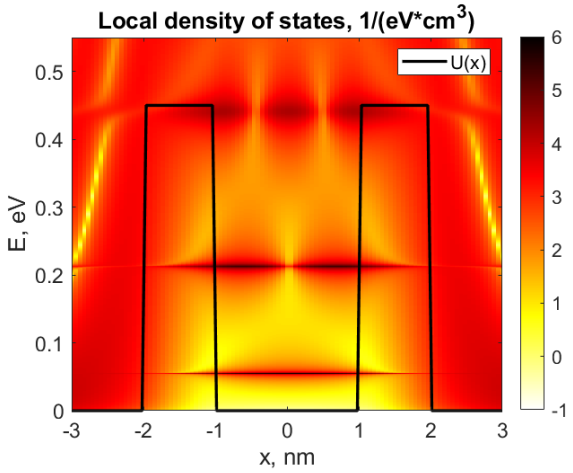

(b) First instance of a third confined energy level.

Figure 3.4: Transmission analysis for different U_0 values.

The total currents derived for the different U_0 values are reported in figure 3.5. As for the analysis with varying barriers thickness, an increase in U_0 causes the current to be reduced quite significantly; however, despite the slight shift to higher voltages due to the energy levels repositioning, the shape of the current oscillations is not particularly affected, which is better highlighted by the logarithmic plot in figure 3.5b.

Therefore, similarly to the case analysed in section 3.1, it is reasonable to assume that the U_0 value is not the main parameter determining the current shape, even though it has a more relevant role than the barriers thickness.

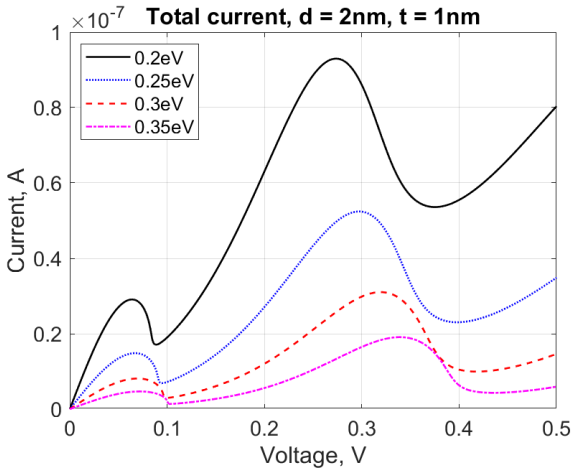

(a) Linear current axis.

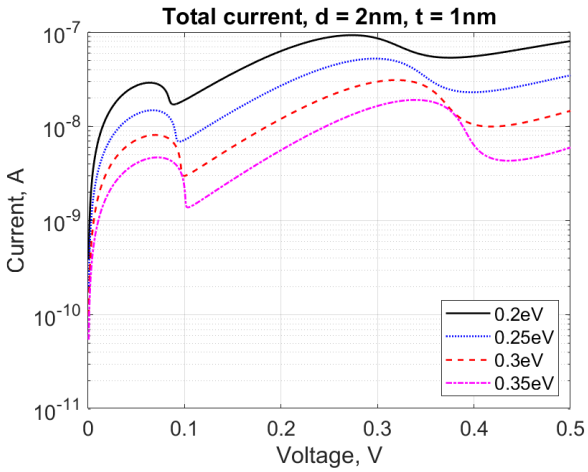

(b) Logarithmic current axis.

Figure 3.5: Total current for different U_0 values.

3.3 Effect of the distance between barriers

Finally, the last parameter that can be modified is the nanoparticle size, i.e the distance between energy barriers.

As in the previous sections, the other parameters have been kept unchanged in order to identify the role of the nanoparticle size only. In particular, the barriers thickness has been fixed to 1 nm and $U_0 = 0.2\ eV$.

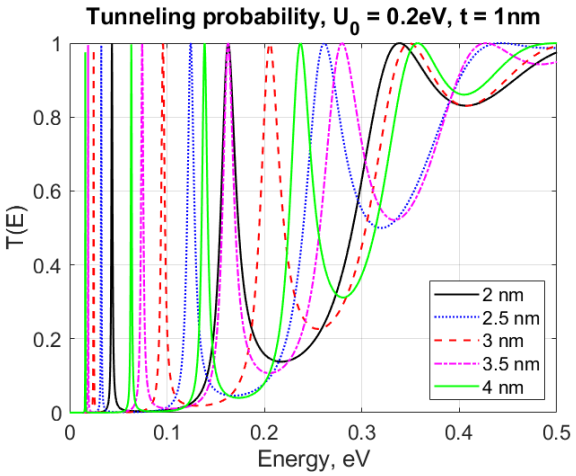

Figure 3.6: Transmission function for different nanoparticle sizes.

In sections 3.1 and 3.2 it has been proven that, respectively, barriers thickness and height only play a minor role in determining the distribution of energy levels within the nanoparticle; as a result, tunneling peaks were slightly affected by a variation in those parameters, and so the current.

Conversely, figure 3.6 appears much more chaotic with respect to the corresponding figures 3.2b and 3.4a obtained by varying the thickness of barriers and the U_0 value; however, it shows how varying the nanoparticle size by a few nanometres drastically affects the number and distribution of confined energy levels, which is also proved by [3]. In particular, as the distance between barriers increases, the energy levels shift towards lower energies, and are allowed to sit closer to one another; starting with two confined levels at 2 nm, this trend allows the inclusion of a third level in the 3.5 nm and 4 nm systems.

As a result of the energy levels repositioning, oscillations in the current-voltage characteristics are also highly dependent on the nanoparticle size, as shown by figure 3.7.

Figure 3.7a confirms the addition of a third energy level within the barriers in the 3.5 nm and 4 nm systems, which emerges as a third current oscillation.

Furthermore, figure 3.7b offers a closer look at the evolution of the first oscillation as the nanoparticle increases in size: due to energy levels being allowed to sit closer to one another in larger particles, the negative differential resistance portion of the oscillation becomes more and more narrow until it ceases to exist in the two larger systems which present a current step rather than an oscillation. This is caused by the second energy level that, being closer to the first one in a larger particle, becomes more easily available for conduction than in smaller particles. Therefore, a smaller bias is required to make its tunneling peak enter the bias window dictated by the difference between the contacts chemical potentials, according to the Landauer-Büttiker formula (2.103) for the current. This results in the first and second energy levels being able to conduct simultaneously, rather than individually such as in the 2 nm- to 3 nm-large systems.

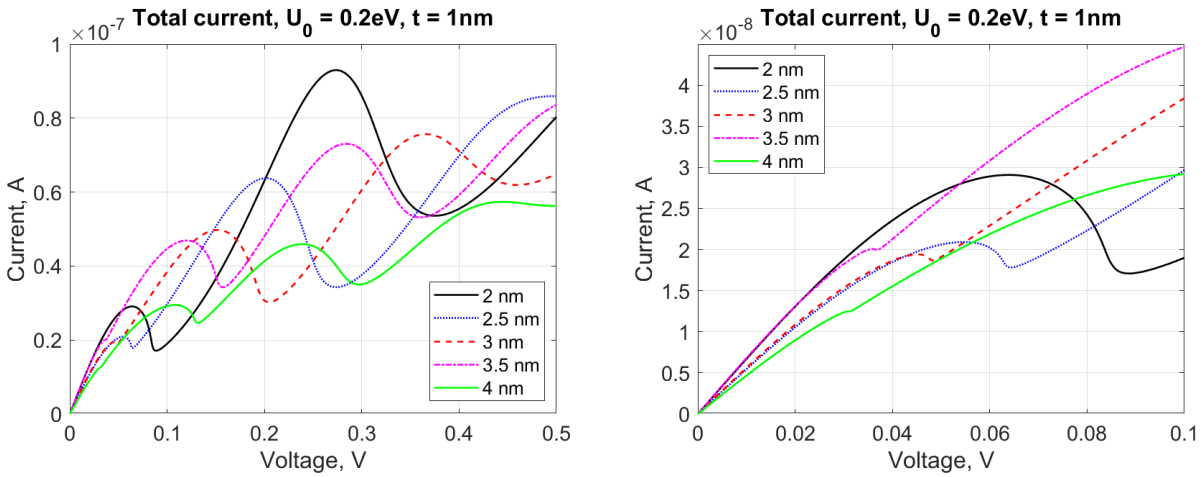

(a) Total current, linear axis.

(b) Detail of the first oscillation.

Figure 3.7: Total current for different nanoparticle sizes.

Thus, in this section, it has been proved that the most effective method of controlling the energy levels distribution inside the nanoparticle is changing its size. In turn, it allows to state that, as the energy levels become more and more densely packed within the nanoparticle, the current trend transitions from resonant oscillations with negative differential resistance to a staircase-like behaviour.

In this particular case, the transition is fully completed as far as the first oscillation is concerned; however, the same pattern can already been observed in the second oscillation, which is severely dampened in the 4 nm system with respect to the 2 nm system.

3.4 Relation between transmission and current peaks

Transmission and current peaks - or steps - are related through the Landauer-Büttiker formula (2.103), and each current oscillation derives from a transmission peak which, in turn, corresponds to a confined energy level.

These relations have been further investigated considering a slightly more complex system such as the one shown in figure 3.8a, which is characterized by five confined energy levels. In this system $U_0 = 0.3\ eV$, the barriers are 1 nm-thick and 5 nm-distant from each other.

As the number of confined energy levels within the barriers increases, the lower-energy levels gets more and more reminiscent of an ideal quantum well with infinite barriers: their transmission peaks in figure 3.8b become more narrow and centered around the energy value associated to each level.

This trend is also noticeable in the local density of states shown in figure 3.8a, which drastically reduces in the region between consecutive energy levels far away from the barriers edge. As a reminder, the colour scale in each and every LDOS plot is logarithmic; thus, it is a representation of the order of magnitude of the LDOS, rather than its actual value.

Observations regarding the effect of each geometrical parameter analysed in sections 3.1 to 3.3 have been confirmed to be valid also in more complex systems such as the one under study in this section, and the correlation between transmission and current peaks has been found to be independent of them.

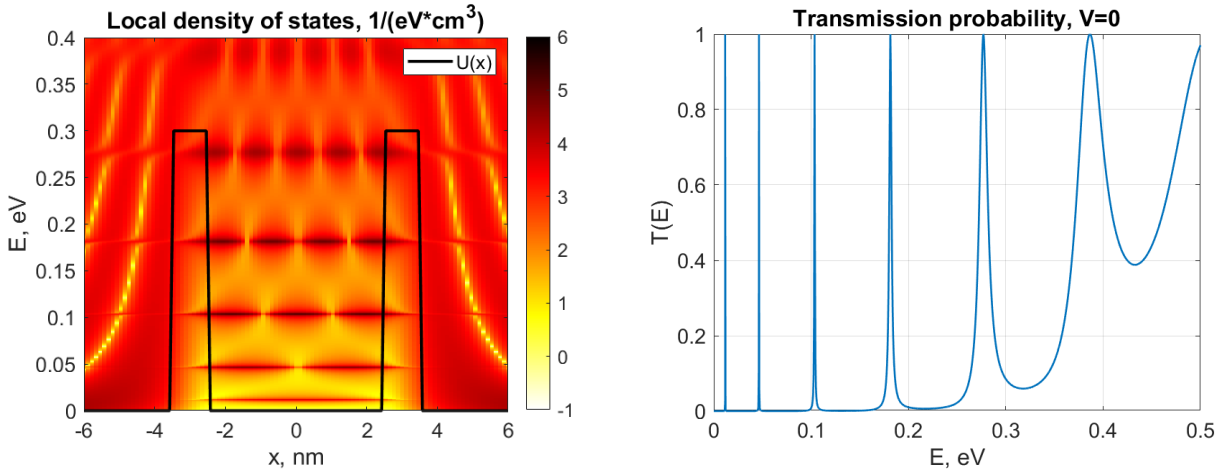

(a) Local density of states.

(b) Equilibrium transmission function.

Figure 3.8: Five-levels system used for the peaks analysis.

The resulting current is reported in figure 3.9. Due to there being five confined energy levels, the total current presents one narrow step and four oscillations of increasing amplitude as the bias voltage rises.

The low-bias current step, which is barely noticeable in the complete curve of figure 3.9a, is shown in detail in figure 3.9b.

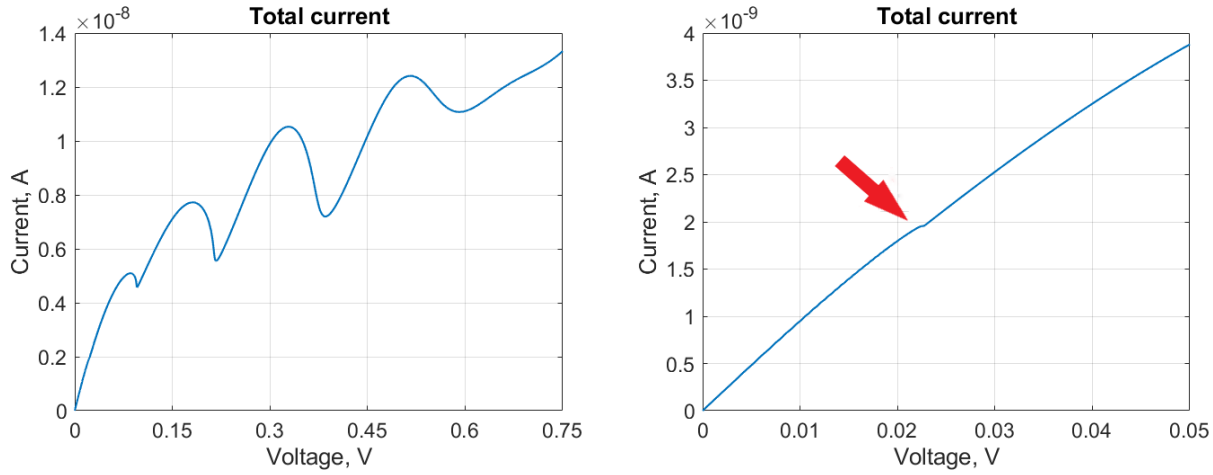

(a) Total current.

(b) Closer look on the first step.

Figure 3.9: Simulation results of the system used for the peaks analysis.

Contributions of first and second energy levels to the total current are barely distinguishable from each other; the reason is that simulations are performed at room temperature, in particular $T = 300\ K$, and the Fermi-Dirac functions of electrons in the contacts present a smooth step centered around each contact chemical potential, similar to the graphical representation in figure 1.3, not an abrupt one such as at temperatures near the absolute zero. For this reason, a few electrons are allowed to have energy above the contacts chemical potential up to a limit which is generally considered to be in the range of a few integer multiples of $k_B T$ above the chemical potential; $k_B \approx 1.38 \cdot 10^{-23}\ JK^{-1}$ is the Boltzmann constant, and T the absolute temperature.

At a temperature equal to 300 K, the product k_BT is equal to:

$$k_BT \approx 25.8\ meV \tag{3.1}$$

while the gap between first and second energy levels, measured from the transmission peaks in figure 3.8b, is approximately equal to 34.7 meV, which is less than a factor of two away from k_BT. This justifies the contributions of the first two levels being nearly indistinguishable from each other.

Peaks positions have been measured from the transmission function in figure 3.8b, and similarly the gap between consecutive peaks. For these purposes, only the central value of each peak has been taken into consideration, which correspond to a tunneling probability identically equal to unity. These measurements for the system in figure 3.8a have been reported in tables 3.1a and 3.1b, respectively.

Peak number	Energy, eV	Voltage, V
1	0.0117	0.0227
2	0.0464	0.0857
3	0.1036	0.1814
4	0.1814	0.3286
5	0.2770	0.5159

(a) Peaks positions, $U_0 = 0.3\ eV$, $t = 1\ nm$.

Peak distance	Energy, eV	Voltage, V
2-1	0.0374	0.0630
3-2	0.0572	0.0957
4-3	0.0778	0.1472
5-4	0.0956	0.1873

(b) Gap between peaks, $U_0 = 0.3\ eV$, $t = 1\ nm$.

Table 3.1: Analysis of position and gap between consecutive current-transmission peaks.

Figure 3.10 is a graphical representation of the data in table 3.1a. Data regarding two other systems have been included to further prove the above stated independence of the current-transmission peaks relation from other geometrical parameters; in particular, figure 3.10 shows two other systems which share every feature with the reference system of figure 3.8a, except for the U_0 value. The only difference between these systems is the number of confined energy levels, which is four instead of five in those with lower U_0.

The plot shows the data placing on a straight line with linear coefficient approximately equal to two; this means that, through the relation between potential energy and voltage $E = q \cdot V$, it is possible for electrons subject to a bias voltage V to access and tunnel across the system if there is an energy level placed at $E \approx q \cdot V/2$.

As the energy levels approach the barriers edge, they progressively drift from the linear relation; however, the lowest energy levels, which are more effectively confined, follow it closely.

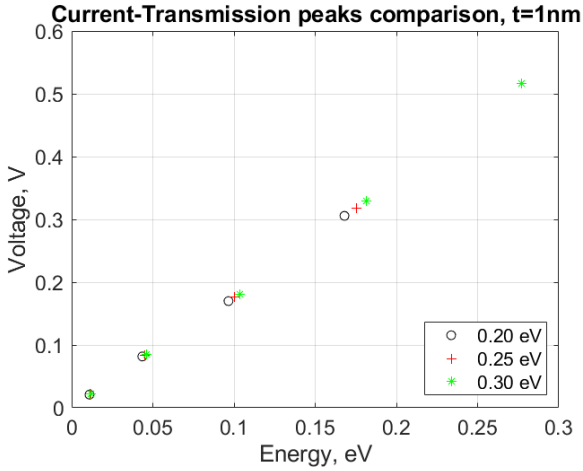

Figure 3.10: Relation of the current peaks position with respect to tunneling peaks position. Different U_0 values, constant thickness of barriers $t = 1\ nm$.

A similar relation emerges from the plot in figure 3.11, which represents the data in table 3.1b. The gap between two consecutive current peaks follows a linear relation with the gap between two consecutive energy levels, and the slope is again approximately equal to two.

In this plot, two systems with different barriers thickness have been compared to again show that this analysis is mostly independent of geometrical parameters: differences mainly start to emerge near the barriers edge, as the confinement of levels slightly loses effectiveness compared to deeper levels.

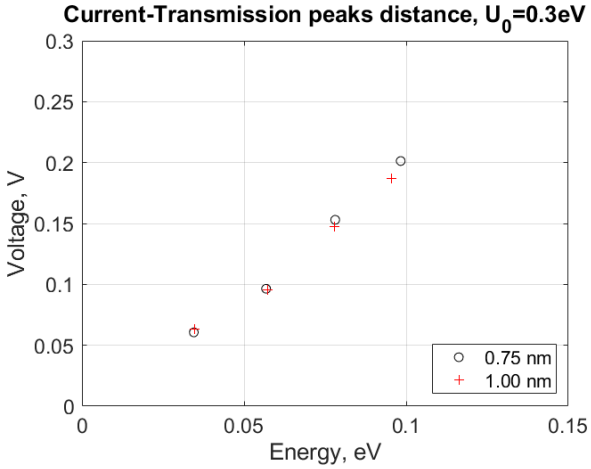

Figure 3.11: Relation of the gap between current peaks with respect to the gap between tunneling peaks. Different thicknesses of barriers, constant $U_0 = 0.3\ eV$.

Thus far, in this analysis, only the peak of each oscillation has been considered; however, current oscillations present a non negligible width which means that, by a certain degree, electrons are able to access the energy levels even though the chemical potential of the injection contact is not perfectly aligned with them. For the same reasons stated above, this phenomenon is more pronounced at room temperature than at low temperatures due to the Fermi-Dirac distribution behaviour.

Nonetheless, the relation $E \approx q \cdot V/2$ which holds between transmission and current peaks, can be better explained when considering that the bias voltage drops linearly across the system, such as shown in the introductory figure 3.1, and more in detail in figure 3.12b.

Since the voltage drop is linearly distributed across the system, the factor two in the relation

$$2E \approx q \cdot V \tag{3.2}$$

can be justified with the plot 3.12b, which shows that with an applied voltage equal to $0.2\ V$, the chemical potential of the left-hand contact is nearly aligned with the third confined energy level of the system, which is placed at around $0.1\ eV$ in both figures 3.12a and 3.12b.

In summary, since the voltage drop is not point-like, but rather distributed uniformly across the system, figure 3.12b illustrates that an alignment between the chemical potential of the injection contact and a confined energy level is indeed approximately obtained according to equation (3.2). Exact positions of transmission and current peaks for the reference system 3.12a are reported in table 3.1a.

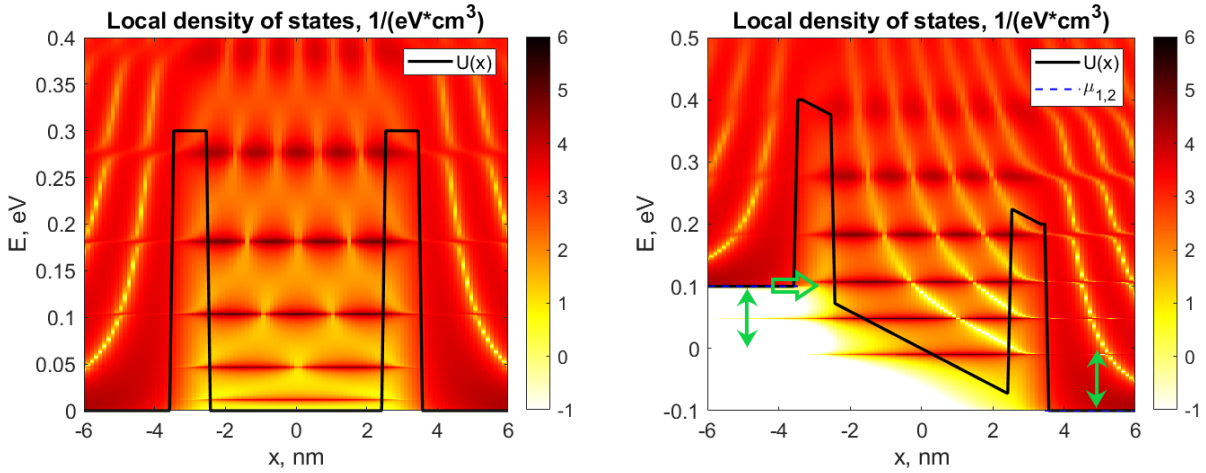

(a) Reference system in equilibrium conditions.

(b) Reference system under the effect of a 0.2 V-bias.

Figure 3.12: Graphical representation of the effect of the total voltage.

Chapter 4

Three-barrier systems: a molecule bound to the nanoparticle

Finally, after the analysis of the contribution of individual energy levels to the total current across a nanoparticle, the NEGF algorithm has been tested in reproducing results similar to a real case scenario, in which the nanoparticle is used to enhance the current signal in an electrochemical biosensor by acting as an intermediate between a metal electrode and the detected molecule.

In this very simplified model, the molecule has been implemented as a double-barrier system, similarly to the nanoparticle. Although this is far from a real case scenario, the attention has been focused on having electrons tunneling across the nanoparticle come from, or move to, another set of discrete energy levels rather than a continuum of available states such as a metal contact could be represented as.

To this purpose, another double-barrier system is a simple but effective solution which allows to observe the desired phenomena and produce meaningful results.

4.1 The metal contact

Since the experimental setup functions with the nanoparticles attached onto a metal contact, the previously implemented bias voltage profile is not reasonable any longer, since it results in a zero local density of states for energies below $U(x)$ at the left-hand injection contact, such as shown in figure 4.1, while in a metal all states below the chemical potential are occupied by electrons.

To address this issue, the new implementation forces the horizontal band edge on the injection side to be equal to

$$U_L = -q\,\frac{|V_{max}|}{2} \tag{4.1}$$

while, at the same time, maintaining the contact chemical potential unchanged. The result is represented in figure 4.2, in which states are allowed to exist below the contact chemical potential.

The value chosen in equation (4.1) is dynamically adjusted depending on the simulation parameters in order to define only the relevant energy range for conduction, according to the maximum bias voltage applied to the system.

With this solution, it is always possible to ensure there are electrons incoming from a contact with energy matching the confined energy levels below the contact chemical potential, even when the barriers are tilted due to the applied bias voltage. For this reason, energy levels of the simulation in figure 4.2 are allowed to act as conducting channels simultaneously if their energy is in the range $[\mu_1, \mu_2]$. This is the main difference with respect to the case in figure 4.1, which has been used through all chapter 3 to analyse individually the contribution of each energy level to the total current.

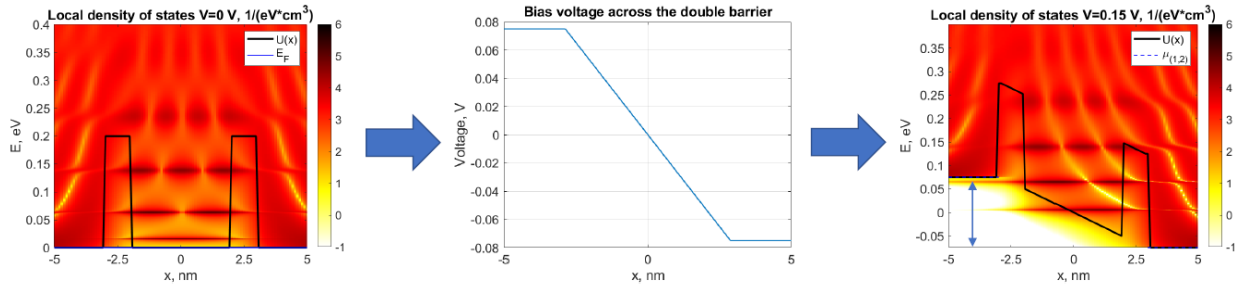

Figure 4.1: Bias voltage profile used in chapter 3 simulations, which includes one energy level at a time in the bias window.

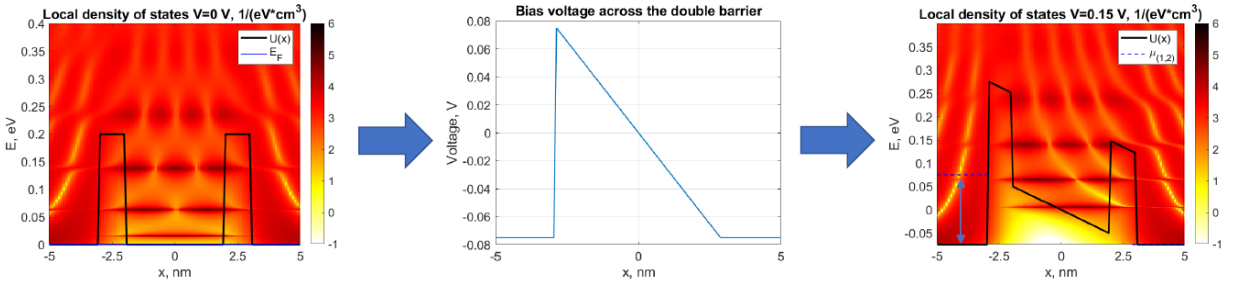

Figure 4.2: Modified bias voltage profile for a metal contact.

4.2 Simulations with a metal contact

A few preliminary tests on a simple double barrier system, such as the reference one in figure 4.2, confirmed again that when the energy levels are only a few multiples of k_BT far away from each other the Coulomb blockade phenomenon is not noticeable at room temperature.

This is clear when considering the system in figure 4.2 under a 0.15 V-bias at room temperature; the derived total current, obtained under the assumption of a metal contact, is shown in figure 4.3b. In this case, the total current does not present any feature of the Coulomb blockade, even more so than the system analysed in figures 3.8 and 3.9 of section 3.4.

In this system, the two lowest energy levels are separated by a 46 meV-wide gap, that has been measured from the corresponding tunneling peaks in the system's equilibrium transmission function, such as in section 3.4.

Although in this system the two lowest energy levels are separated by a larger gap than in the system in figure 3.8, the metal-like contact employed in the current simulation allows these two levels to conduct simultaneously with a 0.15 V bias voltage, rather than trying to highlight the contribution of each level individually such as in section 3.4.

This results into a monotonically increasing current in which the Coulomb blockade phenomenon is hidden behind the conduction by thermal energy of electrons.

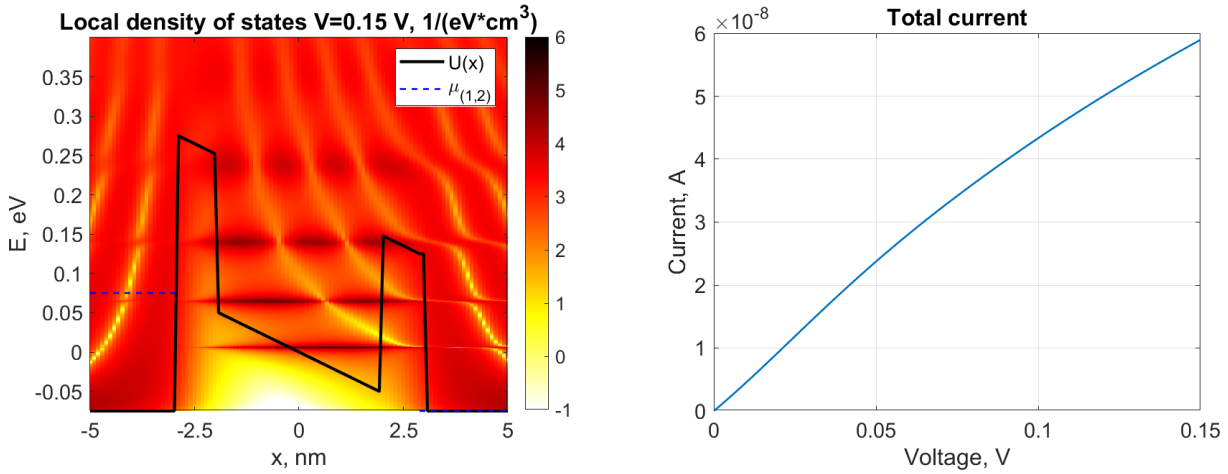

(a) LDOS at $V = 0.15\ V$.

(b) Total current.

Figure 4.3: Test system; conduction with a metal contact at $T = 300\ K$.

To prove this point, several simulations of the same system have been performed at different temperatures. By lowering the temperature, the typical features of the Coulomb blockade phenomenon are restored, as illustrated by figure 4.4.

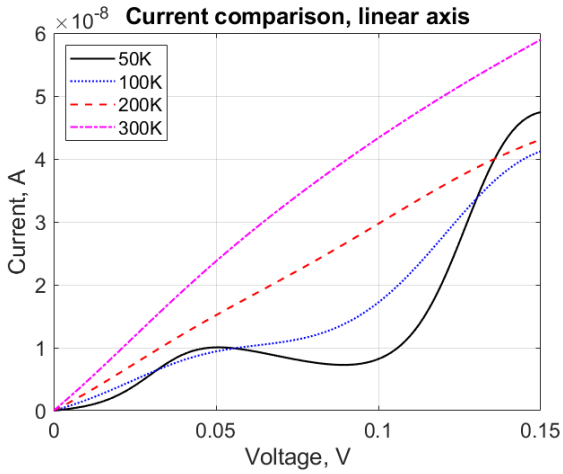

Figure 4.4: Current comparison at different temperatures. For $T < 200\ K$ the Coulomb staircase is restored.

By reducing the distance between barriers, or the nanoparticle size, it is possible to force the energy levels further apart from each other; thus increasing the gap between them.

By keeping the other geometrical parameters unchanged with respect to the system in figure 4.3a, the modified double-barrier system is presented in figure 4.5a: due to the energy levels being forced further apart, only two of them remain confined and the gap between them has been measured to be equal to:

$$E_2 - E_1 \approx 139\ meV \gg k_B T \approx 25.8\ meV \tag{4.2}$$

from the gap between transmission peaks.

The total current for the system is shown in figure 4.5b and, due to an increased gap between the two energy levels, the Coulomb blockade features have been restored even at room temperature.

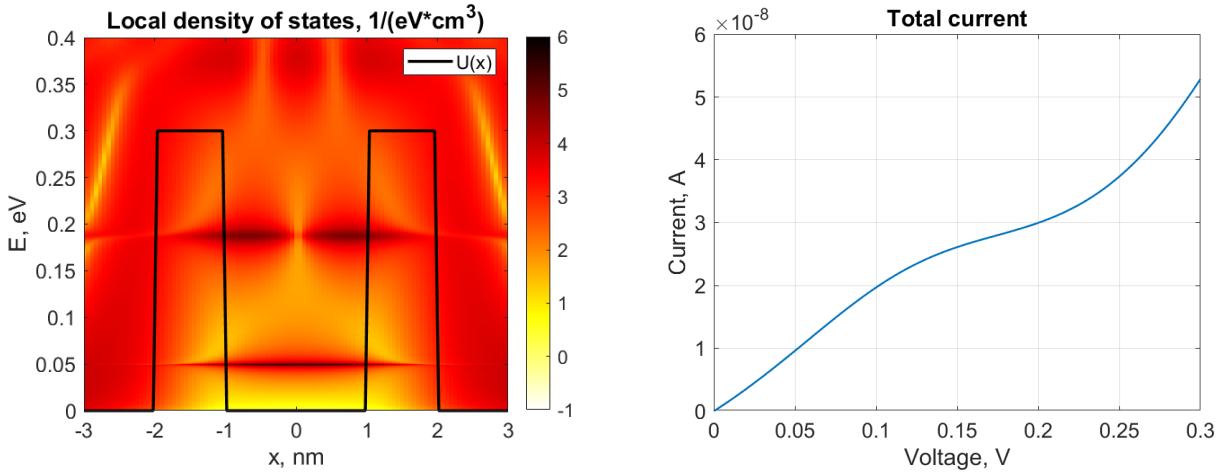

(a) Equilibrium LDOS.

(b) Total current at $T = 300\ K$.

Figure 4.5: Restoring the Coulomb blockade at room temperature by increasing the gap between energy levels.

4.3 Nanoparticle-molecule bound system

This analysis is based on the concept of sequential tunneling of electrons from a molecular energy level to the metal contact, through the nanoparticle, or vice versa according to the applied bias voltage.

It has already been observed in several occasions in the previous sections that when an electron incoming from a contact has an energy comparable with a confined energy level of the nanoparticle, it is able to tunnel through the system with probability equal to unity; thus reaching the other contact.

Then, by binding a molecule to the nanoparticle, electrons should be able to tunnel through the whole system if there is at least one pair composed of a molecular and a nanoparticle energy level with matching energy; thus ensuring the existence of a conducting channel that traverses both molecule and nanoparticle.

If such a conducing channel exists, incoming electrons that match its energy are able to tunnel through both systems with probability equal to unity.

4.3.1 Individual systems

As already quoted during the introduction to this chapter, the molecule has been modelled as a double-barrier system, similarly to the nanoparticle. This solution is simple, yet effective, in providing another set of discrete energy levels communicating with the nanoparticle ones.

Individual systems, each with its own set of energy levels are shown in figures 4.6 and 4.7, and their individual energy levels, measured from the transmission functions in figures 4.6b and 4.7b, are listed in table 4.1.

Level number	Nanoparticle, eV	Molecule, eV
1	0.016	0.043
2	0.063	0.163
3	0.139	//

Table 4.1: Individual nanoparticle and molecule energy levels.

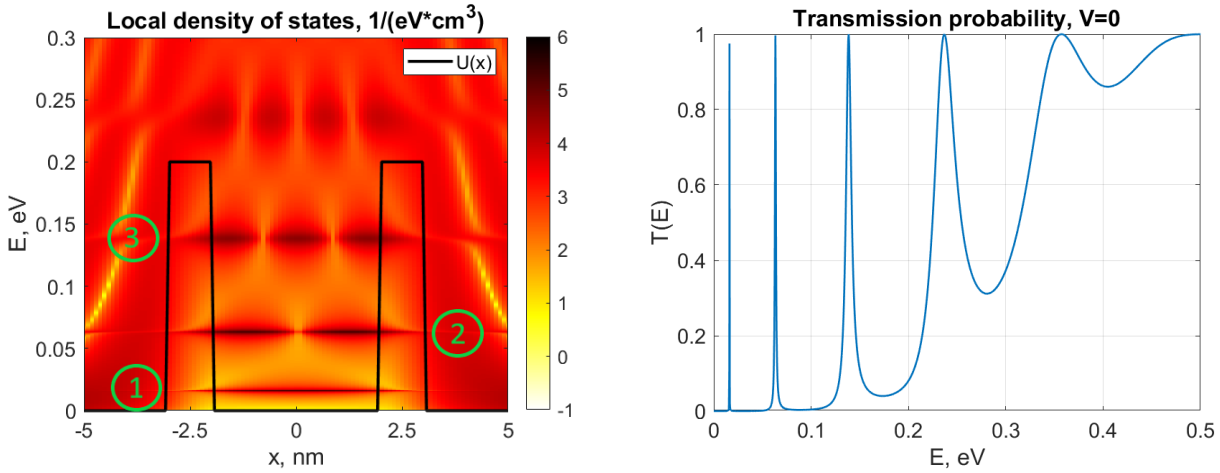

(a) LDOS. (b) Transmission function.

Figure 4.6: Nanoparticle, $U_0 = 0.2\ eV$, size 4 nm and thickness of barriers 1 nm.

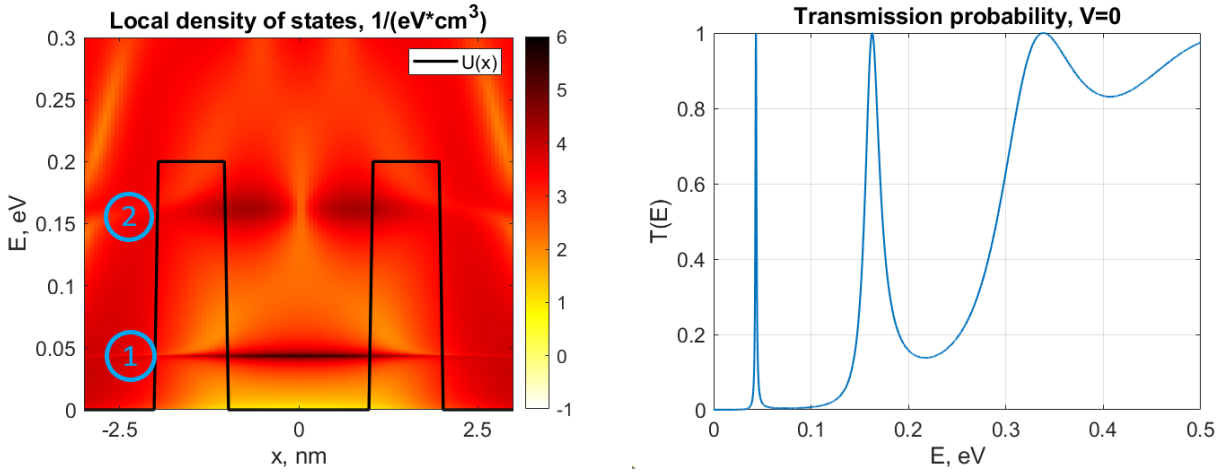

(a) LDOS. (b) Transmission function.

Figure 4.7: Molecule, $U_0 = 0.2\ eV$, length 2 nm and thickness of barriers 1 nm.

The nanoparticle's parameters of size and thickness of barriers have been chosen according to reasonable values found in literature for gold nanoparticles, such as [21], [22], [23] and [24].

Instead, the molecule length of 2 nm has been chosen to place its energy levels close enough to the nanoparticle ones, in order to easily align them by means of a rigid translation of either system to higher or lower energies, or through an applied bias voltage that tilts the energy barriers.

4.3.2 The bound system

When connecting together the two systems, one of the barriers enclosing the molecular energy levels can be removed: this is reasonable because these barriers are only necessary to generate a set of discrete molecular levels, and the barrier representing the nanoparticle shell can fulfil this purpose as well.

Moreover, since the molecule presumably binds directly onto the nanoparticle shell, this is also more reasonable than having a thicker barrier on the binding side of the nanoparticle.

The compound system is shown in figure 4.8 together with its transmission function. At equilibrium, the tunneling probability depends on individual energy levels of both structures as they all have different energies; for this reason, the transmission function presents one peak corresponding to each energy level and none of them reach unity since a unique conducting channel made of two aligned levels is not present.

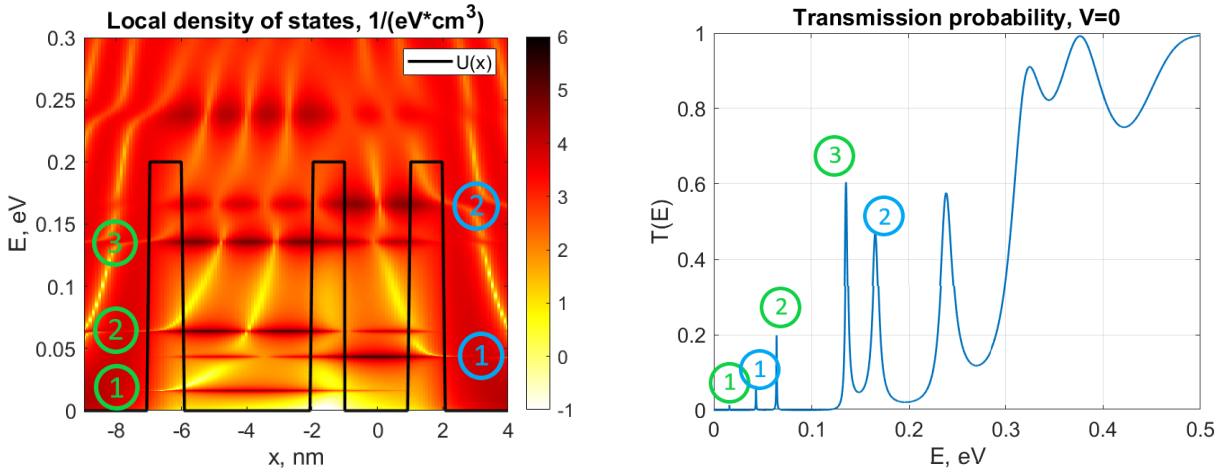

(a) LDOS highlighting the energy levels of the two systems.

(b) Transmission function.

Figure 4.8: Nanoparticle-molecule bound system; small tunneling peaks are distinguishable in the transmission function for each energy level.

Instead, by applying a bias voltage to the system, it is possible to tilt the barriers; thus achieving an alignment between nanoparticle and molecular energy levels. At first, the voltage drop has been applied only to the nanoparticle because the molecule was considered short enough not to be affected by it; however, this assumption has been relaxed at a later time.

In this particular system, two different alignment conditions can be achieved: the first one between level 1 of the nanoparticle and level 1 of the molecule, and the second one between level 2 of the nanoparticle and level 2 of the molecule, according to the enumeration in table 4.1. The first case is shown in figure 4.9, while the second one in figure 4.10.

The conducting channel formed by level 3 of the nanoparticle and level 2 of the molecule can be glimpsed at in figure 4.9a even if the levels are not perfectly aligned with a 0.05 V-bias voltage; however, it does not affect the total current since it is placed at an energy outside of the bias window determined by $[\mu_1, \mu_2]$.

As shown in figures 4.9b and 4.10b, when two energy levels are aligned by the effect of the bias voltage, the tunneling probability reaches values close to unity for electron energies that match the conducting channel. This proves the theoretical expectation about electrons being able to tunnel through both systems when two energy levels have equal or comparable energy.

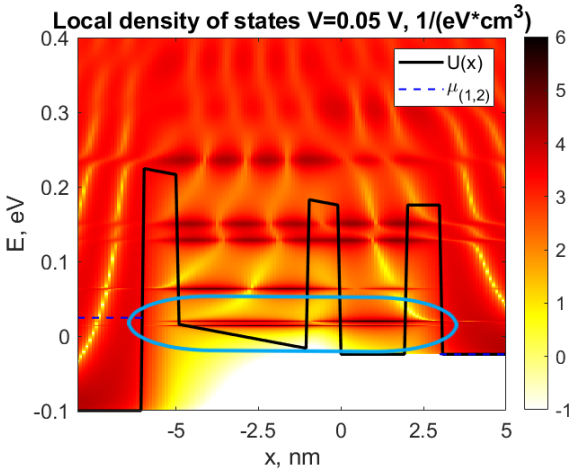

(a) LDOS showing the first pair of energy levels aligning.

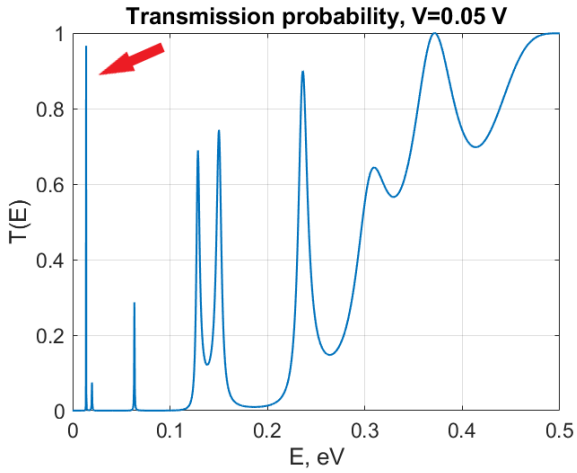

(b) Transmission function.

Figure 4.9: Bound system under a 0.05 V-bias.

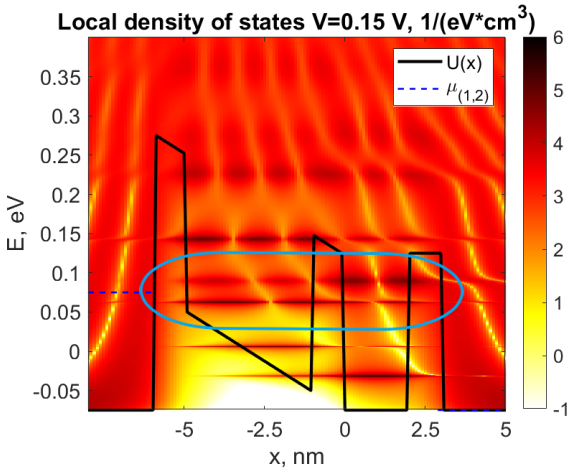

(a) LDOS showing the second pair of energy levels aligning.

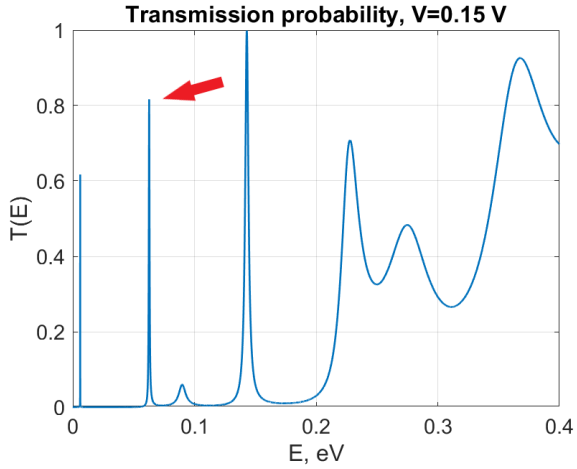

(b) Transmission function.

Figure 4.10: Bound system under a 0.15 V-bias.

The current resulting from the analysed system is reported in figure 4.11. It is possible to notice that, as the first pair of energy levels closes in to each other, the current increases exponentially; then, when the first conducting channel is formed around $V = 0.05\ V$, the current stops increasing until the second pair of energy levels enters the bias window determined by $[\mu_1, \mu_2]$. Finally, as the second conducting channel begins to form, the current slows again its rise.

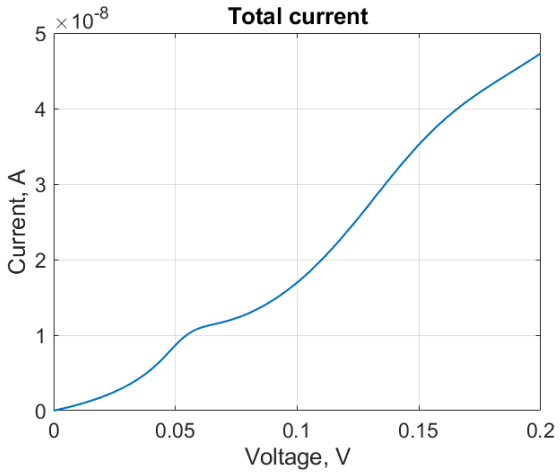

Figure 4.11: Bound system, total current.

4.3.3 Voltage drop across the molecule

In the previous section, the third barrier enclosing the molecular energy levels has been excluded from the voltage drop. This choice has been made because a molecule is in general short enough that the bias voltage can be considered constant at its ends.

Nonetheless, it is reasonable to assume that a voltage drop could be present even at the molecule ends. Therefore, in this analysis, the voltage drop has been extended to include the molecule and, for the sake of simplicity, the slope of the linear voltage drop has been assumed to be the same across the whole system.

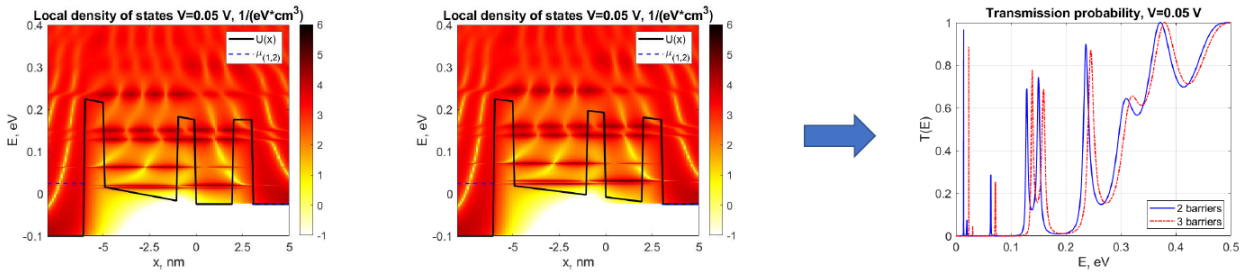

(a) 0.05 V bias voltage.

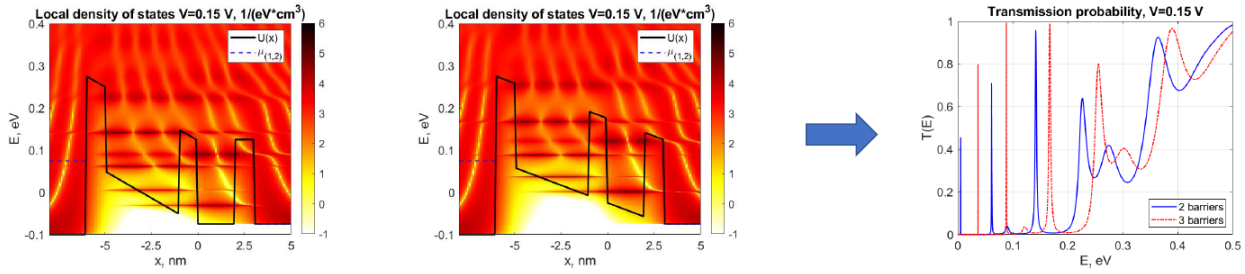

(b) 0.15 V bias voltage.

Figure 4.12: Bias voltage comparison with and without extending the voltage drop to the third barrier.

Figure 4.12 compares the same system analysed in the previous section with and without the extension of the voltage drop to the third barrier.

It is possible to observe that the transmission functions of the two cases start to differentiate as the bias voltage increases, even though they used to coincide perfectly in equilibrium conditions. This is due to the different gradient of the voltage between the two cases, as the figures illustrate.

This difference is reflected onto the total current: although the conducting channels originate from the same pair of energy levels, the alignment conditions is obtained for slightly different values of the bias voltage; moreover, the more realistic case, in which the voltage drop is extended across the three barriers, produces a more pronounced current step than the other case.

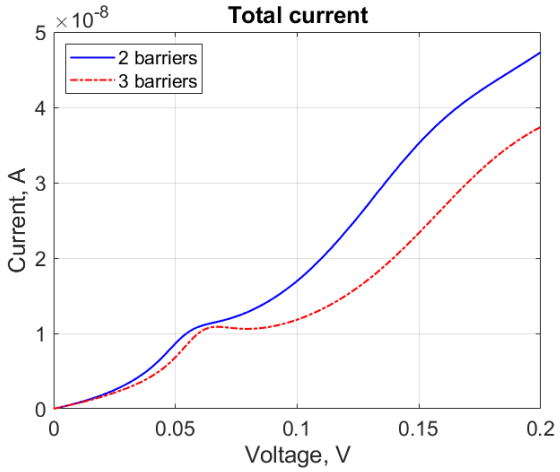

Figure 4.13: Current comparison with and without extending the voltage drop to the third barrier.

4.3.4 The importance of levels alignment

As a further proof of the crucial role played by the conducting channels originating from aligned energy levels, the system analysed in the previous sections has been compared with a similar one in which energy levels align outside of the bias window.

A similar condition can be achieved recalling that the total current is obtained from the Landauer-Büttiker formula, which is reported here for clarity:

$$I(E) = \int T(E)\left[f(E-\mu_1) - f(E-\mu_2)\right]\ dE \tag{4.3}$$

As observed in the previous sections, an alignment between a nanoparticle and a molecular energy level gives rise to a sharp peak that can reach unity in the transmission function $T(E)$. However, since $T(E)$ is multiplied by the difference between the Fermi-Dirac distributions of the contacts in equation (4.3), the contribution of a conducting channel can be excluded from the total current if it is placed at an energy E such that

$$f(E-\mu_1) - f(E-\mu_2) = 0 \tag{4.4}$$

The system used to achieve such a condition is reported in figure 4.14; in this system, the nanoparticle size has been reduced to 2 nm, and the molecule length to 1.5 nm to redistribute the energy levels of both systems to different energies.

At equilibrium there are no conducting channels; however, with a bias voltage approximately equal to 0.06 V the lowest energy levels of both systems align and a tunneling peak is obtained in figure 4.14d. Nonetheless, figure 4.14c shows that this conducting channel is not included in the bias window determined

by the chemical potentials of the contacts, and a further tilting of the barriers originating from a higher voltage drop would cause the energy levels to enter the bias window misaligned from each other.

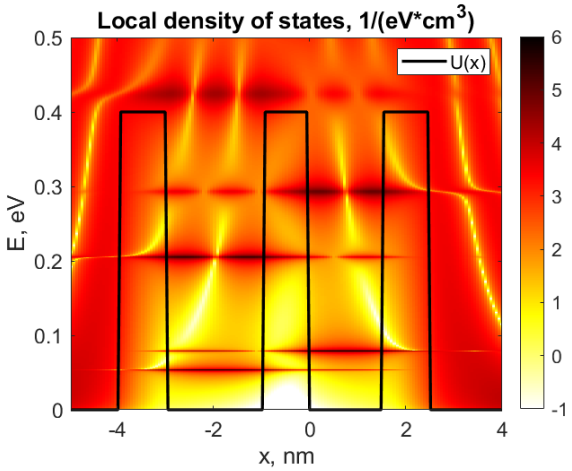

(a) LDOS, equilibrium conditions.

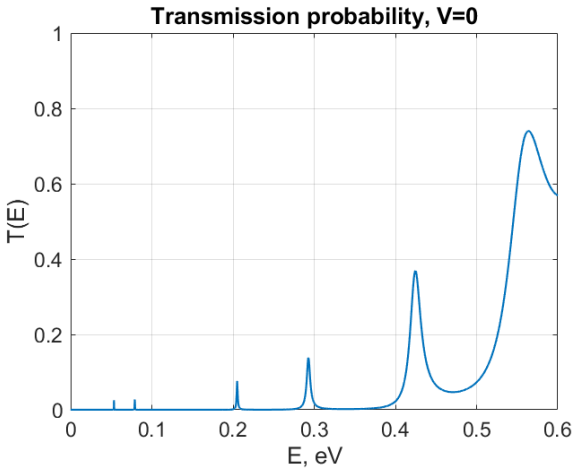

(b) Transmission function, equilibrium conditions.

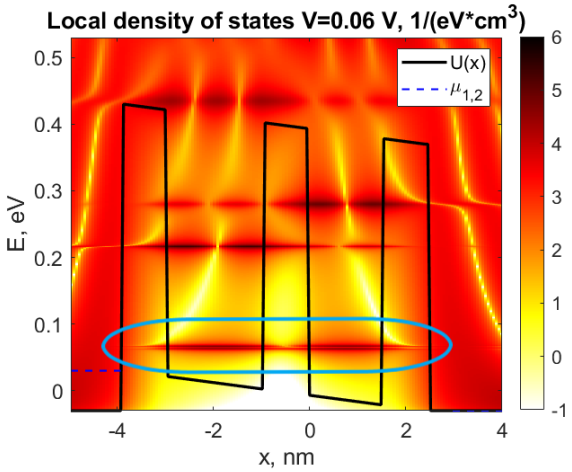

(c) LDOS, $V = 0.06\ V$.

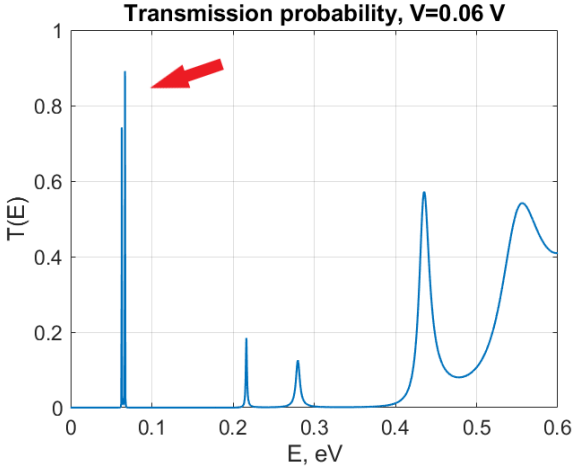

(d) Transmission function, $V = 0.06\ V$.

Figure 4.14: System with conducting channel outside the bias window.

The total current derived from the system in figures 4.14 has been compared with that of the system in figure 4.12a, in which the voltage drops across the three barriers, and the energy levels align, thus forming a conducting channel, inside the bias window.

The two curves are plotted in figure 4.15, and clearly the current produced by the misaligned energy levels of the system in figure 4.14 is significantly lower than the current originating from a pair of aligned energy levels.

Nonetheless, it is still possible to notice a small resonance even in the case with misaligned levels: this resonance occurs for a bias voltage approximately equal to $0.06\ V$, which is the value that causes the energy levels to align outside the bias window in figure 4.14c.

It has already been observed that at a temperature higher than the absolute zero the Fermi-Dirac distributions of electrons in the contacts are not actually equal to zero for $E > \mu$, but they gradually decrease to zero in the range of a few integer multiples of $k_B T$ above μ. In this case, the gap between the

conducting channel and the chemical potential of the left-hand contact is approximately equal to

$$37.9\ meV \approx k_B T = 25.8\ meV \tag{4.5}$$

measured by difference between the tunneling peak in figure 4.14d, and $\mu_1 = 0.03\ eV$. This justifies the presence of a few electrons with energy matching that of the conducting channel even if it is placed outside the bias window; those electrons are able to tunnel through the whole system with ease, thus causing a slight increase in current as long as the energy levels remain aligned.

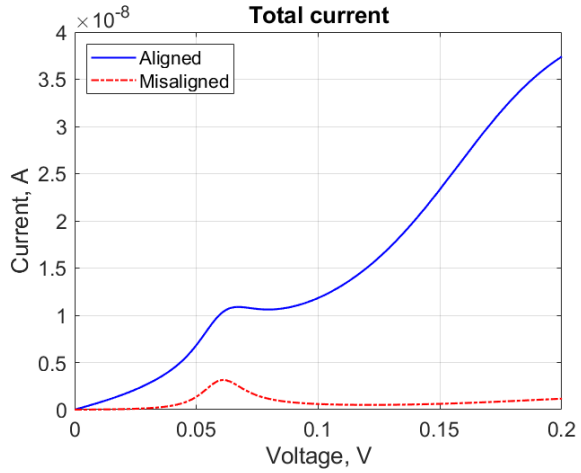

Figure 4.15: Current comparison of aligned and misaligned energy levels inside the bias window.

4.3.5 Crossing over of energy levels

Thus far, all the reported systems have shown energy levels crossing over from the nanoparticle to the molecule, and vice versa. This is particularly evident when comparing the nanoparticle and molecule taken individually as in figures 4.6a and 4.7a, respectively, with the bound system shown in figure 4.8a and reported in figure 4.16 to highlight two instances of this phenomenon.

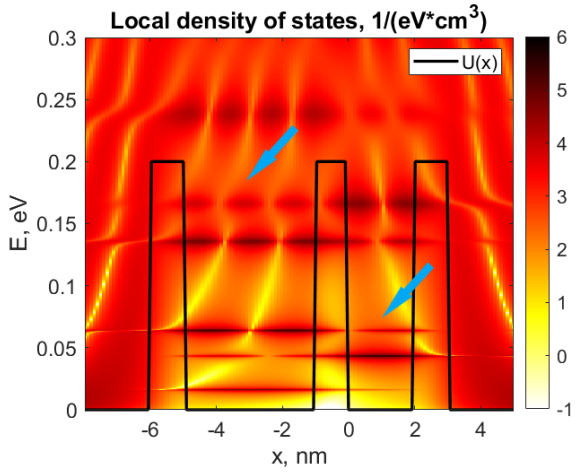

Figure 4.16: Energy levels crossing over in the bound system.

There are already studies accounting for this phenomenon concerning semiconductor heterostructures, such as [25], in which wavefunctions confined in a sequential quantum well structure often cross over to the neighbouring quantum wells. However, other similar studies have presented results in which this phenomenon is missing, such as [26].

The main difference between these two examples is the order of magnitude of the investigated quantum systems: layers in the *GaN/AlGaN* sequential quantum well studied in [25] are comparable in thickness with the lengths used along the x-axis in figure 4.16, while layers reach up to tenths of nanometers in thickness in the *AlGaAs/GaAs* triple-barrier diode analysed in [26].

To prove this assumption, all the lengths in the system in figure 4.16 have been doubled, while maintaining the same U_0. The resulting system is reported in figure 4.17.

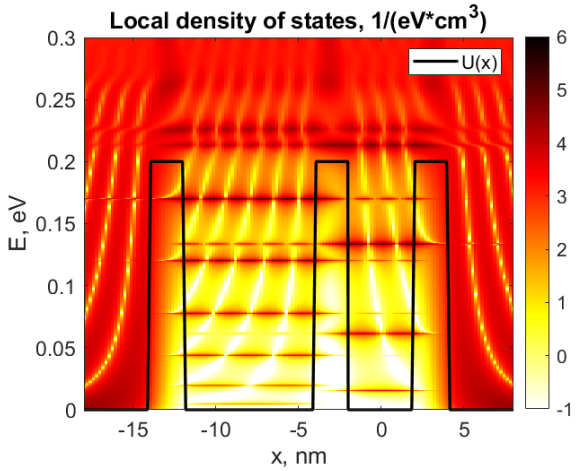

(a) Misaligned energy levels.

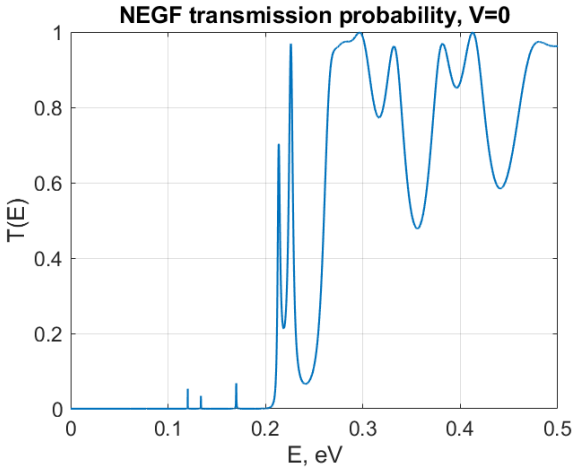

(b) Transmission function, no tunneling peaks.

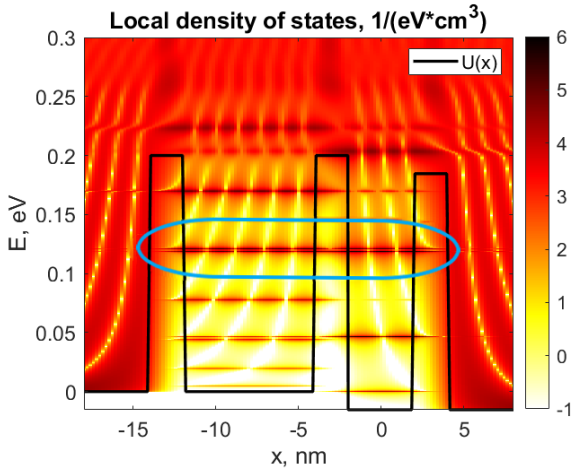

(c) Aligned energy levels.

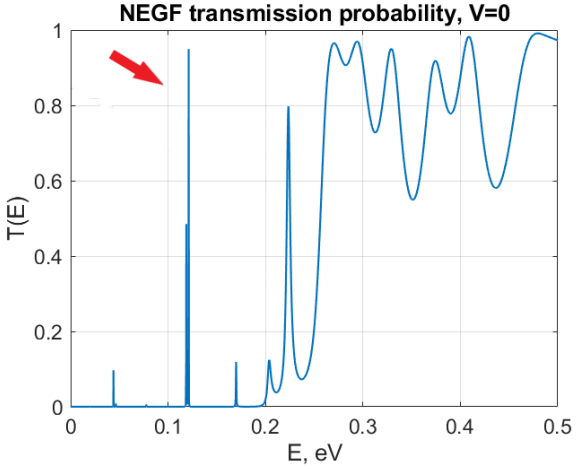

(d) Transmission function with a conducting channel.

Figure 4.17: Larger system with no crossing over of energy levels.

It is possible to notice that the deeper energy levels in figure 4.17a do not cross over between the two structures, while the crossing over starts again to appear near the barriers edges, where energy levels are more affected by the non-ideality and the finite barriers of the system.

Furthermore, an alignment between two energy levels has been obtained in figure 4.17c by rigid translation

of the third barrier to slightly lower energies. This allows the formation of a conducting channel even without applying a bias voltage, thus resulting in the sharp tunneling peak highlighted in figure 4.17d. Hence, the crossing over of energy levels does not affect the formation of a conducting channel.

4.3.6 Conduction of an individual molecule

To prove the utility of a nanoparticle in enhancing the current signal produced by a molecule, a comparison has been made between the systems in figure 4.18.

Figure 4.18a shows the system already used in the analysis of the previous sections, while the system in figure 4.18b has been obtained simply removing the double barrier representing the nanoparticle, and substituting it with a unique barrier of equal thickness so that the nanoparticle energy levels are removed from the simulation and the thick barrier represents the distance between the molecule and the contact.

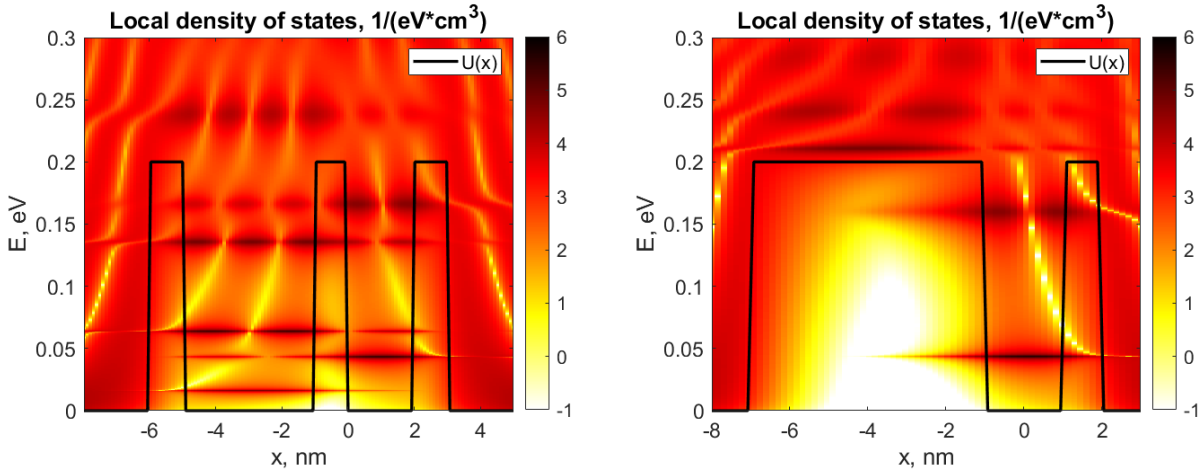

(a) Nanoparticle-molecule bound system.

(b) System obtained removing the nanoparticle.

Figure 4.18: Systems with and without the nanoparticle energy levels.

Such a large distance distance between the contact and the molecule causes the transmission function to be flat and equal to zero until the electron energy matches that of the barriers, such as shown in figure 4.19a.

However, figure 4.19b presents a detail of the transmission function for energies lower than 0.1 eV. Small tunneling peaks are still present, and the one represented arises in correspondence to the lowest energy level in figure 4.18b.

Although very small compared to unity, these tunneling peaks allow to calculate a total current according to the Landauer-Büttiker formula (4.3).

The current resulting from the system in figure 4.18b is plotted in figure 4.20. The current-voltage relationship of the system closely reminds that of an electrical resistance; therefore, this proves that the thick barrier prevails over the discrete molecular energy levels in determining the current shape.

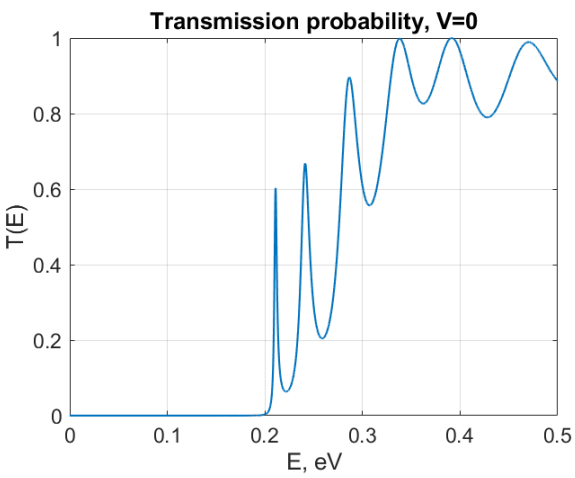

(a) Equilibrium conditions $T(E)$.

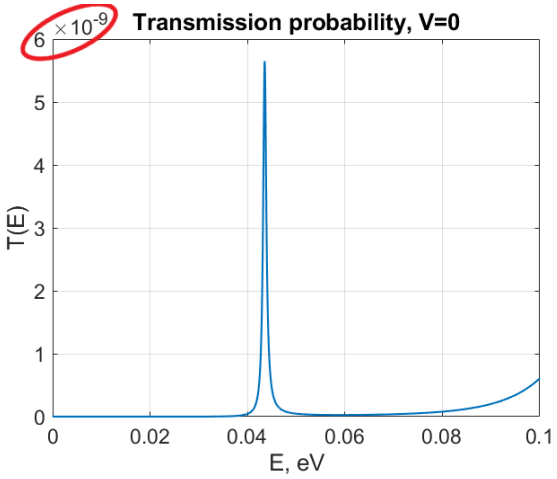

(b) Detail for $0\ eV < E < 0.1\ eV$.

Figure 4.19: Transmission function of the system in figure 4.18b without nanoparticle.

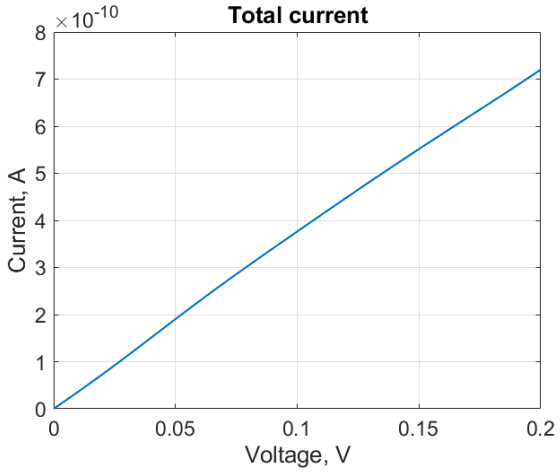

Figure 4.20: Resistance-like I-V characteristics without nanoparticle.

In a more realistic scenario, when the nanoparticle is not present the molecule can be allowed to bind directly to the metal contact and the thickness of the tunneling barrier separating them would be lower than the nanoparticle size.

Figure 4.21 shows the evolution of the current signal of an individual molecule as its distance from the contact progressively reduces. It is possible to notice that for distances larger than 3 nm the current trend is mostly linear, with slight deviations. Conversely, the Coulomb blockade trend emerges again for distances equal to 2 nm or lower.

Finally, although at a distance of 1.5 nm from the contact the current signal shows a trend that can be attributed to the Coulomb blockade inside the molecule, figure 4.22 illustrates the clear advantage in having a nanoparticle enhancing the current. Even if the presence of the nanoparticle puts the molecule further away from the contact, the current signal is drastically enhanced by the nanoparticle, and the current step is much more visible than without it.

Furthermore, comparing figures 4.15 and 4.21, it can be observed that the alignment of nanoparticle and molecular energy level is a crucial point in obtaining a detectable current signal: when the energy levels

are misaligned, instead of enhancing the signal, the nanoparticle yields a current even lower than that of an individual molecule.

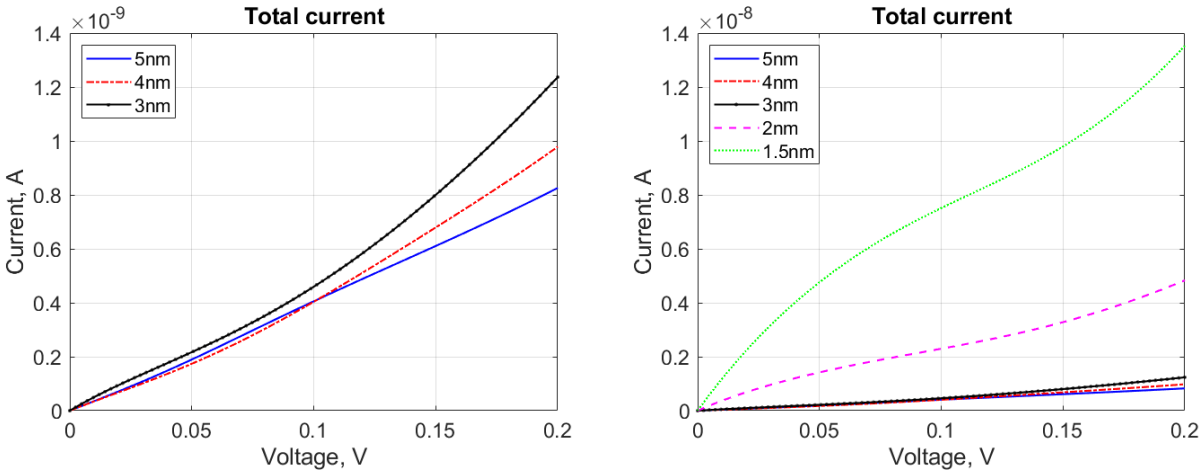

(a) Linear I-V characteristics.

(b) Restoring a glimpse of the Coulomb blockade.

Figure 4.21: Current of an individual molecule with decreasing distance from the contact.

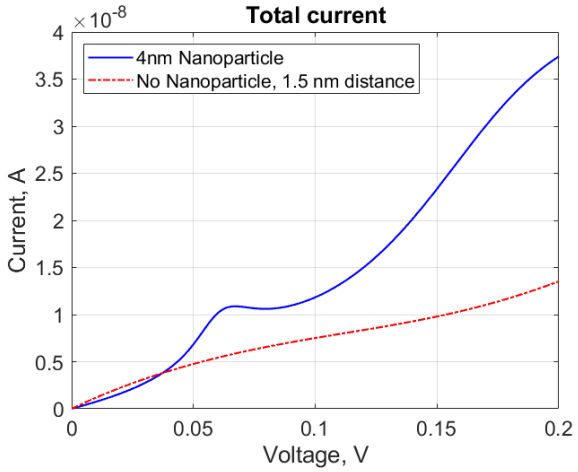

Figure 4.22: Current of an individual molecule and a molecule enhanced by a nanoparticle.

4.4 Simulation of a real system

Finally, the NEGF model has been put to the test in reproducing a current-voltage characteristics from an experimental measurement. The reference experimental setup is a cyclic voltammetry of *cytochrome P450scc* on gold nanoparticles, which is outlined in [27].

On average, in this experiment, gold nanoparticles have been measured to be 12 nm in diameter by Atomic Force Microscopy (AFM), while measurements also performed by AFM on single-molecule cytochrome P450 state that, on average, the molecule is 3.5 nm-long, with a quite relevant standard deviation equal to 0.9 nm [28].

For the purposes of this simulations only the average values have been used, namely a 12 nm-diameter gold nanoparticle and a 3.5 nm-long cytochrome P450 molecule.

Since it treats a real system, many parameters required for the simulation were not specified in [27], such as the thickness of the tunneling barriers, the U_0 value, or the availability of energy levels; therefore, they were found by trial and error in search of a current trend reminding of the curve in figure 4.23, which is taken from the paper.

The curve corresponding to the cytochrome plus nanoparticle is the one plotted with a solid line; the dashed and dotted ones represent the bare electrode and the electrode with nanoparticles only, respectively. Measurements are performed under aerobic conditions with a 100 nM phosphate buffer solution.

The crucial point in figure 4.23 is the presence of a peak in current due to the oxidation of the electrochemically reduced cytochrome molecule reacting with the oxygen in the environment, and the charge flow is mediated by the nanoparticle channelling the electron transport through its energy levels.

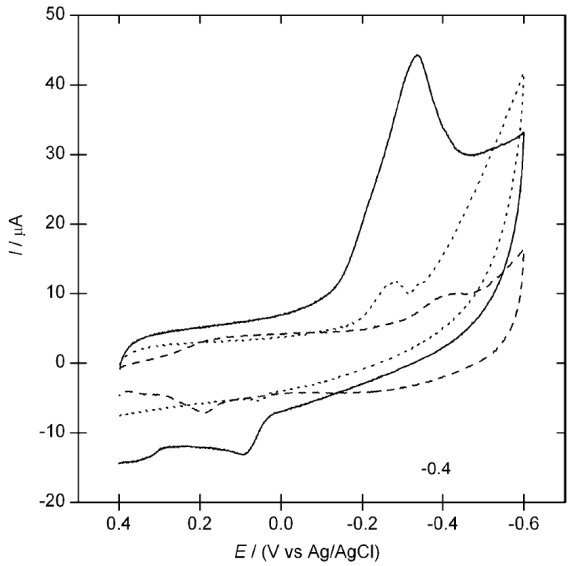

Figure 4.23: Experimental voltammogram, image taken from [27].

The different experimental conditions, such as the aerobic environment and the presence of a buffer solution are not conceived by the algorithm, since it only receives as input the potential energy profile. Moreover, due to the many missing parameters and the large dimensions of the system that entail a significantly higher number of confined energy levels compared to the cases shown in the previous sections, the time required for the simulation increases drastically and it becomes very challenging to analyse this system with the current implementation of the algorithm.

Nonetheless, the system that allows to obtain the most similar curve is shown in figure 4.24a, in which the molecule has been translated to lower energies with respect to the nanoparticle and, in particular below the equilibrium chemical potential of the contacts, which is chosen to be equal to 0.2 eV, in an attempt to emulate the electrochemically-reduced condition by ensuring its energy levels are all occupied. The nanoparticle also presents a few energy levels below the equilibrium chemical potential, to emulate a more realistic condition in which a few are occupied but there are still many available for conduction; the molecule is placed so that, at equilibrium, the two set of molecular and nanoparticle energy levels cannot communicate and exchange charge. In addition, the zero-current condition is achieved in the experiment for $V = 0.4\ V$, as well as the current is different than zero with a null bias voltage; for these reasons, the equilibrium condition of the simulation, in which the chemical potentials of contacts coincide, is achieved for a 0.4 V voltage drop across the system too.

The current derived from the simulation of the system is reported in figure 4.24b, with the exception of the second portion of the curve concerning the cyclic voltammogram. The voltage axis is also inverted to match figure 4.23.

There are still many differences between the experimental data and the reproduced one, the most noticeable being the difference of approximately one order of magnitude in the signal intensity. This result is not completely satisfactory yet: the current peak is wider than the experimental one, as well as the current presents a steady increasing trend that starts from positive bias voltage values, instead of remaining nearly constant until $V \approx -0.1\ V$, such as in figure 4.23.

The simulation does not exactly match the experiment; nonetheless, even with the few simple considerations stated above and despite the many limitations of the current model, a similar current trend is achievable in which the current reaches a maximum in correspondence of the oxidation peak of the cytochrome molecule.

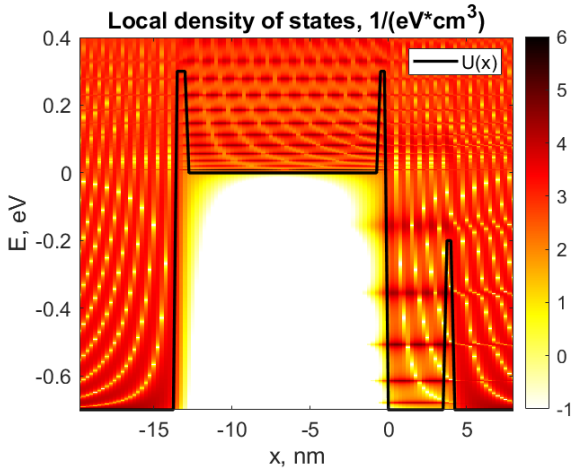

(a) LDOS with bias voltage equal to 0 V.

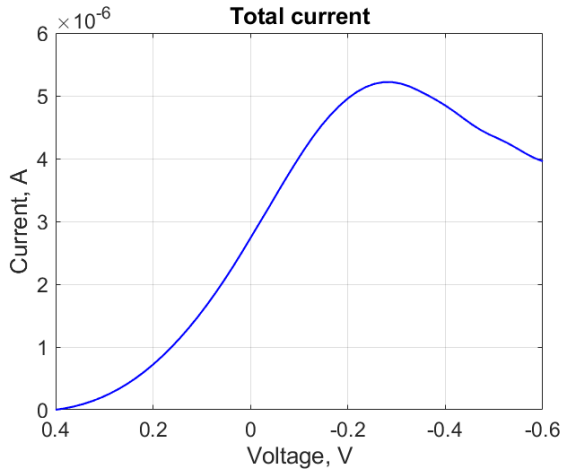

(b) Current-Voltage characteristic.

Figure 4.24: System used for the simulation of the experimental setup.

Conclusions and outlook

To summarize and conclude, this work aims to be a first step in the direction of a comprehensive tool in the design and modelling of nanoparticle-enhanced electrochemical biosensors.

The analysis is focused on the understanding of the mechanisms underlying the electron transport across a nanoparticle starting from first-principles quantum mechanics and knowledge regarding Schrödinger-like problems, instead of relying on a parametric approach to fit experimental data.

Since this is only the first step in achieving that objective, a viable model for the numerical solution of the problem is presented in the NEGF, and effectively applied to relatively simple systems consisting of either a single nanoparticle or a nanoparticle-molecule bound system.

Nonetheless, even simple systems like these allow to understand the relations between tunneling of electrons through discrete channels and the resulting current, as well as the importance of the nanoparticle in enhancing the measured signal.

However, given the overall complexity of the problem at hand, the results are quite satisfactory although the description is incomplete as far as the current is concerned, since only the coherent component is considered. A complete description would require the inclusion of other phenomena that complement the coherent tunneling of electrons; the *hopping* phenomenon is an example which presumably plays a role as important as tunneling when dealing with organic molecules, but relatively to incoherent transport of electrons. A natural continuation to this work could be the inclusions of such phenomena in the model.

Regardless, the first step should be the optimization of the algorithm, making it more efficient and less time-consuming on simple systems such as the ones analysed in this work. This limitation becomes particularly clear when trying to reproduce the experimental results in section 4.4, which entails the simulation of a more complex system.

Loops are particularly inefficient in the MATLAB environment and they should be, if possible, substituted by either array-wide operations or recursive functions. Moreover, the accuracy of the algorithm strongly depends on the refinement of the energy mesh and, in the current implementation, a uniform mesh is used. This is not ideal, since some parts in the energy mesh might require a higher accuracy, while others might not benefit from it. Such is the case for localized states which manifest themselves as sharp peaks in the transmission probability of electrons.

Bibliography

[1] Omar Manasreh. *Semiconductor Heterojunctions and Nanostructures*. 1st ed. US: McGraw-Hill Education, 2005. ISBN: 0071469680. DOI: 10.1036/9780071469685. eprint: https://mhebooklibrary.com/doi/pdf/10.1036/9780071469685. URL: https://mhebooklibrary.com/doi/book/10.1036/9780071469685.

[2] Claude Cohen-Tannoudji, B. Diu, and F. Laloë. *Quantum Mechanics, Volume 1*. Wiley, 1991. ISBN: 9780471164333. URL: https://books.google.it/books?id=iHcpAQAAMAAJ.

[3] Sandro Carrara et al. "On the role of nanoparticle sizes in monoelectron conductivity". In: *Nato Asi 3 High Tech* 18 (1996), pp. 497–503.

[4] Supriyo Datta. *Electronic Transport in Mesoscopic Systems*. Cambridge Studies in Semiconductor Physics and Microelectronic Engineering. Cambridge University Press, 1995. DOI: 10.1017/CBO9780511805776.

[5] Carlo Jacoboni. *Coherent Transport in Mesoscopic Structures*. July 2010. ISBN: 978-3-642-10585-2. DOI: 10.1007/978-3-642-10586-9_21.

[6] Rosemary Gardner. *Nanoelectronics Part II Single-Electron and Few-Electron Phenomena and Devices Chapter 6 Tunnel Junctions and Applications of Tunneling*. 2015. URL: https://slideplayer.com/slide/9903095/.

[7] Salvatore Esposito. "Multibarrier tunneling". In: *Phys. Rev. E* 67 (1 Jan. 2003), p. 016609. DOI: 10.1103/PhysRevE.67.016609. URL: https://link.aps.org/doi/10.1103/PhysRevE.67.016609.

[8] Aaron Szafer and A. Douglas Stone. "Theory of Quantum Conduction through a Constriction". In: *Phys. Rev. Lett.* 62 (3 Jan. 1989), pp. 300–303. DOI: 10.1103/PhysRevLett.62.300. URL: https://link.aps.org/doi/10.1103/PhysRevLett.62.300.

[9] Henrik Bruus and K. Flensberg. *Many-Body Quantum Theory in Condensed Matter Physics: An Introduction*. Oxford Graduate Texts. OUP Oxford, 2004. ISBN: 9780198566335. URL: https://books.google.it/books?id=v5vhg1tYLC8C.

[10] Robert Vichnevetsky. *Computer methods for partial differential equations*. Vol. 1. Prentice-Hall, 1981.

[11] Supriyo Datta. *Quantum Transport: Atom to Transistor*. Cambridge University Press, 2005. DOI: 10.1017/CBO9781139164313.

[12] Yongqiang Xue, S. Datta, and Mark A. Ratner. "First-principles based matrix Green's function approach to molecular electronic devices: general formalism". In: *Chemical Physics* 281.2-3 (Aug. 2002), pp. 151–170. ISSN: 0301-0104. DOI: 10.1016/s0301-0104(02)00446-9. URL: http://dx.doi.org/10.1016/S0301-0104(02)00446-9.

[13] Hocine Boumrar et al. *Equivalence of wave function matching and Green's functions methods for quantum transport: generalized Fisher-Lee relation*. 2019. arXiv: 1912.11506 [cond-mat.mes-hall].

[14] Madhi Pourfath. *The Non-Equilibrium Green's Function Method for Nanoscale Device Simulation*. July 2014. ISBN: 978-3-7091-1799-6. DOI: 10.1007/978-3-7091-1800-9.

[15] Claude Cohen-Tannoudji, B. Diu, and F. Laloë. *Quantum Mechanics, Volume 2*. A Wiley interscience publication v. 2. Wiley, 1977. ISBN: 9780471164357. URL: https://books.google.it/books?id=2KjvAAAAMAAJ.

[16] Mathieu Luisier. *Quantum Transport for Nanostructures*. Sept. 2006. URL: https://nanohub.org/resources/1792.

[17] Richard P. Feynman, R.B. Leighton, and M. Sands. *The Feynman Lectures on Physics, Vol. III: The New Millennium Edition: Quantum Mechanics*. The Feynman Lectures on Physics. Basic Books, 2011. ISBN: 9780465025015. URL: https://books.google.it/books?id=KsnbNL%5C_rh04C.

[18] C. Caroli et al. "Direct calculation of the tunneling current". In: *Journal of Physics C: Solid State Physics* 4.8 (June 1971), pp. 916–929. DOI: 10.1088/0022-3719/4/8/018. URL: https://doi.org/10.1088%2F0022-3719%2F4%2F8%2F018.

[19] G. Lake Roger snd Klimeck, R. Chris Bowen, and D. Jovanovic. "Single and multiband modeling of quantum electron transport through layered semiconductor devices". In: *Journal of Applied Physics* 81.12 (1997), pp. 7845–7869. DOI: 10.1063/1.365394. eprint: https://doi.org/10.1063/1.365394. URL: https://doi.org/10.1063/1.365394.

[20] R. de Picciotto et al. "Multi-terminal ballistic transport in one-dimensional wires". In: *Physica E: Low-dimensional Systems and Nanostructures* 6 (Feb. 2000), pp. 514–517. DOI: 10.1016/S1386-9477(99)00097-1.

[21] Dragomir Davidović and M. Tinkham. "Coulomb blockade and discrete energy levels in Au nanoparticles". In: *Applied Physics Letters* 73.26 (1998), pp. 3959–3961. DOI: 10.1063/1.122949. eprint: https://doi.org/10.1063/1.122949. URL: https://doi.org/10.1063/1.122949.

[22] N.K. Chaki et al. "Single-electron charging features of larger, dodecanethiol-protected gold nanoclusters: electrochemical and scanning tunneling microscopy studies." In: *Langmuir: the ACS journal of surfaces and colloids* 20 23 (2004), pp. 10208–17.

[23] Alexander Kyrychenko et al. "Preparation, structure, and a coarse-grained molecular dynamics model for dodecanethiol-stabilized gold nanoparticles". In: *Computational and Theoretical Chemistry* 977.1 (2011), pp. 34–39. ISSN: 2210-271X. DOI: https://doi.org/10.1016/j.comptc.2011.09.003. URL: http://www.sciencedirect.com/science/article/pii/S2210271X11004592.

[24] Shinya Kano et al. "Room-Temperature Coulomb Blockade from Chemically Synthesized Au Nanoparticles Stabilized by AcidBase Interaction". In: *Applied Physics Express - APPL PHYS EXPRESS* 3 (Oct. 2010). DOI: 10.1143/APEX.3.105003.

[25] Faisal F. Sudradjat et al. "Sequential tunneling transport in GaN/AlGaN quantum cascade structures". In: *physica status solidi c* 9.3-4 (2012), pp. 588–591. DOI: https://doi.org/10.1002/pssc.201100423. eprint: https://onlinelibrary.wiley.com/doi/pdf/10.1002/pssc.201100423. URL: https://onlinelibrary.wiley.com/doi/abs/10.1002/pssc.201100423.

[26] T. Nakagawa et al. "Observation of resonant tunneling in AlGaAs/GaAs triple barrier diodes". In: *Applied Physics Letters* 49.2 (1986), pp. 73–75. DOI: 10.1063/1.97356. eprint: https://doi.org/10.1063/1.97356. URL: https://doi.org/10.1063/1.97356.

[27] Victoria Shumyantseva et al. "Direct electron transfer between cytochrome P450scc and gold nanoparticles on screen-printed rhodium–graphite electrodes". In: *Biosensors & bioelectronics* 21 (Aug. 2005), pp. 217–22. DOI: 10.1016/j.bios.2004.10.008.

[28] Timothy H. Bayburt and Stephen G. Sligar. "Single-molecule height measurements on microsomal cytochrome P450 in nanometer-scale phospholipid bilayer disks". In: *Proceedings of the National Academy of Sciences of the United States of America* 99.10 (May 2002), pp. 6725–6730. ISSN: 0027-8424. DOI: 10.1073/pnas.062565599. URL: https://doi.org/10.1073/pnas.062565599.

Appendix A

Analytic derivation for single- and double-barrier transmission probabilities

In this appendix, explicit derivation for the single- and double-barrier transmission probabilities will be provided, expanding on section 1.1.

A.1 Single barrier

Following the derivation in [1] and with figure 1.1 as a reference, naming the potential energy U instead of V to avoid misunderstanding it for the bias voltage, the Hamiltonian of the system can be written as

$$H = -\frac{\hbar^2}{2m}\frac{d^2}{dx^2} + U(x) \ , \qquad U(x) = \begin{cases} 0 & x < 0 \\ U_0 & 0 \leq x < L \\ 0 & x \geq L \end{cases} \tag{A.1}$$

and the stationary eigenvalue Schrödinger equation reduces to a Helmholtz-like equation for the eigenfunctions:

$$H\psi(x) = E\psi(x) \quad \Rightarrow \quad \left[\frac{d^2}{dx^2} + \frac{2m}{\hbar^2}\left(E - U(x)\right)\right]\psi(x) = 0 \quad \Rightarrow \quad \psi''(x) + k^2\psi(x) = 0 \tag{A.2}$$

The general harmonic solution, under the hypotheses presented in section 1.1 is:

$$k_1 = k_3 = \sqrt{\frac{2mE}{\hbar^2}} \ , \quad k_2 = \sqrt{\frac{2m(E-U_0)}{\hbar^2}} \quad \Rightarrow \quad \psi(x) : \begin{cases} \psi_I(x) = Ae^{ik_1x} + Be^{-ik_1x} \\ \psi_{II}(x) = Ce^{ik_2x} + De^{-ik_2x} \\ \psi_{III}(x) = Fe^{ik_1x} \end{cases} \tag{A.3}$$

where A, B, C, D, F are complex coefficients to be determined through the continuity boundary conditions of $\psi(x)$ and its first derivative at the points where the potential changes definition:

$$\begin{cases} \psi_I(x=0) = \psi_{II}(x=0) \\ \left.\dfrac{d\psi_I(x)}{dx}\right|_{x=0^-} = \left.\dfrac{d\psi_{II}(x)}{dx}\right|_{x=0^+} \\ \psi_{II}(x=L) = \psi_{III}(x=L) \\ \left.\dfrac{d\psi_{II}(x)}{dx}\right|_{x=L^-} = \left.\dfrac{d\psi_{III}(x)}{dx}\right|_{x=L^+} \end{cases} \Rightarrow \begin{cases} A + B = C + D & \text{(A.4)} \\ k_1 A - k_1 B = k_2 C - k_2 D & \text{(A.5)} \\ Ce^{ik_2 L} + De^{-ik_2 L} = Fe^{ik_1 L} & \text{(A.6)} \\ k_2 Ce^{ik_2 L} - k_2 De^{-ik_2 L} = k_1 Fe^{ik_1 L} & \text{(A.7)} \end{cases}$$

Multiplying (A.6) by k_2, then summing (A.6) and (A.7), the ratio C/F can be expressed as:

$$\frac{C}{F} = \frac{k_1 + k_2}{2k_2} e^{i(k_1 - k_2)L} \tag{A.8}$$

Instead, by subtracting the same two equations D/F is obtained:

$$\frac{D}{F} = \frac{k_2 - k_1}{2k_2} e^{i(k_1 + k_2)L} \tag{A.9}$$

Multiplying (A.4) by k_1, then summing (A.4) and (A.5) and dividing both members of the resulting equation by F, the Fresnel coefficient t is obtained:

$$t^{-1} = \frac{A}{F} = \frac{k_1 + k_2}{2k_1}\frac{C}{F} + \frac{k_1 - k_2}{2k_1}\frac{D}{F} \tag{A.10}$$

Substituting (A.8) and (A.9) into (A.10):

$$\begin{aligned} t^{-1} = \frac{A}{F} &= \frac{(k_1 + k_2)^2}{4k_1 k_2} e^{ik_1 L} e^{-ik_2 L} - \frac{(k_1 - k_2)^2}{4k_1 k_2} e^{ik_1 L} e^{ik_2 L} = \\ &= e^{ik_1 L}\left[\frac{k_1^2 + k_2^2}{4k_1 k_2}\left(e^{-ik_2 L} - e^{ik_2 L}\right) + \frac{4k_1 k_2}{4k_1 k_2}\left(e^{-ik_2 L} + e^{ik_2 L}\right)\right] \quad \Rightarrow \\ \Rightarrow \quad t^{-1} &= e^{ik_1 L}\left[\cos(k_2 L) - i\frac{k_1^2 + k_2^2}{2k_1 k_2}\sin(k_2 L)\right] \end{aligned} \tag{A.11}$$

Finally, the transmission probability:

$$\begin{aligned}
T = |t|^2 = t \cdot t^* = \\
= & \frac{e^{-ik_1 L}}{\cos(k_2 L) - i\frac{k_1^2 + k_2^2}{2k_1 k_2}\sin(k_2 L)} \cdot \frac{e^{ik_1 L}}{\cos(k_2 L) + i\frac{k_1^2 + k_2^2}{2k_1 k_2}\sin(k_2 L)} = \\
= & \frac{1}{\cos^2(k_2 L) + \left(\frac{k_1^2 + k_2^2}{2k_1 k_2}\right)^2 \sin^2(k_2 L)} = \\
= & \frac{1}{1 - \sin^2(k_2 L) + \left(\frac{k_1^2 + k_2^2}{2k_1 k_2}\right)^2 \sin^2(k_2 L)} = \\
= & \frac{1}{1 + \left[\left(\frac{k_1^2 + k_2^2}{2k_1 k_2}\right)^2 - 1\right] \sin^2(k_2 L)} = \\
= & \frac{1}{1 + \left(\frac{k_1^2 - k_2^2}{2k_1 k_2}\right)^2 \sin^2(k_2 L)}
\end{aligned} \tag{A.12}$$

Substituting $k_1 = \sqrt{\frac{2mE}{\hbar^2}}$ and $k_2 = \sqrt{\frac{2m(E-U_0)}{\hbar^2}}$:

$$T(E) = \frac{4E(E-U_0)}{4E(E-U_0) + U_0^2 \sin^2\left(\sqrt{\frac{2m(E-U_0)}{\hbar^2}} L\right)}, \qquad E > V_0 \tag{A.13}$$

If $E < U_0$, the equality $\sin(ix) = i\sinh(x)$ can be used:

$$\sin^2\left(\sqrt{\frac{2m(E-U_0)}{\hbar^2}} L\right) = \sin^2\left(i\sqrt{\frac{2m(U_0-E)}{\hbar^2}} L\right) = -\sinh^2\left(\sqrt{\frac{2m(U_0-E)}{\hbar^2}} L\right) \tag{A.14}$$

Finally,

$$T(E) = \begin{cases} \dfrac{4E(U_0-E)}{4E(U_0-E) + U_0^2 \sinh^2\left(\sqrt{\frac{2m(U_0-E)}{\hbar^2}} L\right)}, & E < U_0 \\ \dfrac{4E(E-U_0)}{4E(E-U_0) + U_0^2 \sin^2\left(\sqrt{\frac{2m(E-U_0)}{\hbar^2}} L\right)}, & E \geq U_0 \end{cases} \tag{A.15}$$

In case $\sqrt{\frac{2m(U_0-E)}{\hbar^2}} L \gg 0$, the positive-argument exponential prevails and $\sinh(x) = \frac{e^x - e^{-x}}{2} \approx \frac{e^x}{2}$; therefore, if $E \ll U_0$, the first term in the sum at denominator in $T(E)$ is much smaller than the second one. In these conditions, the first term can be neglected and the transmission probability can be approximated as

a decaying exponential function of the barrier thickness L:

$$\begin{aligned} T(E) &\approx \frac{4E(U_0-E)}{\frac{U_0^2}{4}\exp\left\{2\sqrt{\frac{2m(U_0-E)}{\hbar^2}}L\right\}} = \frac{16E(U_0-E)}{U_0^2}\exp\left\{-2\sqrt{\frac{2m(U_0-E)}{\hbar^2}}L\right\} \\ \Rightarrow \quad T(E) &\propto \exp\left\{-2\sqrt{\frac{2m(U_0-E)}{\hbar^2}}L\right\}, \qquad E \ll U_0 \end{aligned} \tag{A.16}$$

A.2 Double barrier

With figure 1.2 as a reference and the coherent combined transmission amplitude

$$t = \frac{t_1 t_2}{1 - r_1 r_2} \tag{A.17}$$

recalling that $t_{(1,2)}$ and $r_{(1,2)}$ are complex numbers; therefore characterized by an absolute value and an argument, it is possible to express them in exponential form as:

$$t_{(1,2)} = \left|t_{(1,2)}\right| \exp\left\{i\phi_{(1,2)}\right\}, \qquad r_{(1,2)} = \left|r_{(1,2)}\right| \exp\left\{i\theta_{(1,2)}\right\} \tag{A.18}$$

Hence,

$$t = \frac{|t_1|\,|t_2| \exp\{i\phi\}}{1 - |r_1|\,|r_2| \exp\{i\theta\}}, \qquad \phi = \phi_1 + \phi_2, \quad \theta = \theta_1 + \theta_2 \tag{A.19}$$

Now, to obtain the tunneling probability t must be multiplied by its complex conjugate t^*:

$$t^* = \frac{|t_1|\,|t_2| \exp\{-i\phi\}}{1 - |r_1|\,|r_2| \exp\{-i\theta\}} \tag{A.20}$$

Thus,

$$\begin{aligned} T(E) = |t|^2 = t \cdot t^* = \\ = &\frac{|t_1|^2\,|t_2|^2}{1 - |r_1|\,|r_2| \exp\{i\theta\} - |r_1|\,|r_2| \exp\{-i\theta\} + |r_1|^2\,|r_2|^2} = \\ = &\frac{|t_1|^2\,|t_2|^2}{1 - 2\,|r_1|\,|r_2| \cos(\theta) + |r_1|^2\,|r_2|^2} \end{aligned} \tag{A.21}$$

It is possible to recognize $\left|t_{(1,2)}\right|^2 = T_{(1,2)}^2$ and $\left|r_{(1,2)}\right|^2 = R_{(1,2)}^2$ as the transmission and reflection probabilities of the individual barriers, respectively. Finally,

$$T(E) = |t|^2 = \frac{T_1 T_2}{1 - 2\sqrt{R_1 R_2}\cos(\theta) + R_1 R_2} \tag{A.22}$$

which is equation (1.12).

Appendix B

Explicit expression of the FEM matrix elements

In this appendix, explicit calculation of the matrix elements is performed; they can be derived analytically starting from equation (2.5), inserting the definition of Lagrange polynomials (2.1). The j-th basis function is different from zero only in the two elements adjacent to node j; for this reason, each integral is non-null for $i = j$ and $i = \pm j$.

B.1 Stiffness matrix elements

The first-order derivative of equation (2.1) is:

$$\frac{dN_j(x)}{dx} = \begin{cases} \dfrac{1}{x_j - x_{j-1}} \ , & x_{j-1} \leq x < x_j \\ \\ \dfrac{-1}{x_{j+1} - x_j} \ , & x_j \leq x < x_{j+1} \end{cases} \qquad j = 2, \ldots, N-1 \tag{B.1}$$

Diagonal elements are obtained for $j = i$:

$$K_{jj} = \int_0^L \frac{dN_j(x)}{dx} \frac{dN_i(x)}{dx} \, dx = \int_{x_{j-1}}^{x_j} \frac{1}{(x_j - x_{j-1})^2} \, dx + \int_{x_j}^{x_{j+1}} \frac{1}{(x_{j+1} - x_j)^2} \, dx =$$

$$= \frac{1}{x_{j+1} - x_j} + \frac{1}{x_j - x_{j-1}} \tag{B.2}$$

In off-diagonal elements, only half of each basis function overlaps with another one,as shown by figure 2.1:

$$K_{j,j+1} = \int_{x_j}^{x_{j+1}} \frac{-1}{(x_{j+1} - x_j)^2} \, dx = -\frac{1}{x_{j+1} - x_j} \tag{B.3}$$

$$K_{j,j-1} = \int_{x_{j-1}}^{x_j} \frac{-1}{(x_j - x_{j-1})^2} \, dx = -\frac{1}{x_j - x_{j-1}} \tag{B.4}$$

B.2 Mass matrix elements

Again, diagonal elements are obtained for $j = i$:

$$M_{jj} = \int_0^L N_j(x) N_j(x)\, dx = \int_{x_{j-1}}^{x_j} \left(\frac{x - x_{j-1}}{x_j - x_{j-1}}\right)^2 dx + \int_{x_j}^{x_{j+1}} \left(\frac{x_{j+1} - x}{x_{j+1} - x_j}\right)^2 dx =$$

$$= \frac{1}{(x_j - x_{j-1})^2} \int_{x_{j-1}}^{x_j} (x - x_{j-1})^2\, dx + \frac{1}{(x_{j+1} - x_j)^2} \int_{x_j}^{x_{j+1}} (x_{j+1} - x)^2\, dx =$$

$$= \frac{x_j - x_{j-1}}{3} + \frac{x_{j+1} - x_j}{3} \tag{B.5}$$

and in off-diagonal cases, only half of each basis function's support overlaps with a neighbouring one:

$$M_{j,j-1} = \int_0^L N_{j-1}(x) N_j(x)\, dx = \int_{x_{j-1}}^{x_j} \left(\frac{x - x_{j-1}}{x_j - x_{j-1}}\right)\left(\frac{x_j - x}{x_j - x_{j-1}}\right) dx =$$

$$= \frac{1}{(x_j - x_{j-1})^2} \int_{x_{j-1}}^{x_j} (x - x_{j-1})(x_j - x)\, dx =$$

$$= \frac{1}{(x_j - x_{j-1})^2} \int_{x_{j-1}}^{x_j} \left(x x_j - x^2 - x_{j-1} x_j + x x_{j-1}\right) dx =$$

$$= \frac{1}{(x_j - x_{j-1})^2} \left[\frac{x^2 x_j}{2} - \frac{x^3}{3} - x_{j-1} x_j x + \frac{x^2}{2} x_{j-1}\right]_{x_{j-1}}^{x_j} =$$

$$= \frac{1}{(x_j - x_{j-1})^2} \left(\frac{x_j^3}{6} - \frac{x_{j-1} x_j^2}{2} + \frac{x_{j-1}^2 x_j}{2} - \frac{x_{j-1}^3}{6}\right) =$$

$$= \frac{(x_j - x_{j-1})^3}{6 (x_j - x_{j-1})^2} = \frac{x_j - x_{j-1}}{6} \tag{B.6}$$

Similarly, the other off-diagonal element:

$$M_{j,j+1} = \frac{x_{j+1} - x_j}{6} \tag{B.7}$$

B.3 Matrix assembling

Finally, it is now possible to assemble the matrix form of Schrödinger's equation to be solved by the calculator.

For each node j of the domain mesh, the (2×2) matrices

$$[K]_j = \begin{bmatrix} K_{11} & K_{12} \\ K_{21} & K_{22} \end{bmatrix}, \qquad [M]_j = \begin{bmatrix} M_{11} & M_{12} \\ M_{21} & M_{22} \end{bmatrix} \tag{B.8}$$

can be defined with the stiffness and mass matrix elements obtained in sections B.1 and B.2, respectively. Then, summing over all mesh points, the matrix form of Schrödinger's equation is obtained as:

$$[H]\{\psi\} = E\,[M]\{\psi\} \tag{B.9}$$

which is equation (2.8); in particular:

$$[H] = \sum_j \left(\frac{\hbar^2}{2m} [K]_j + U_j [M]_j \right) \tag{B.10}$$

$$[M] = \sum_j [M]_j \tag{B.11}$$